UNIVERSITY OF MANCHESTER

SCHOOL OF PHYSICS AND ASTRONOMY

Coupling of Localised Plasmon Resonances

A THESIS SUBMITTED TO THE UNIVERSITY OF MANCHESTER FOR THE DEGREE OF DOCTOR OF PHILOSOPHY IN THE FACULTY OF ENGINEERING AND PHYSICAL SCIENCES

Benjamin David Thackray

2014

Contents

22420 words

List of Figures

Publications

- V. G. Kravets, F. Schedin, R. Jalil, L. Britnell, R. V. Gorbachev, D. Ansell, **B. D. Thackray**, K. S. Novoselov, A. K. Geim, A. V. Kabashin and A. N. Grigorenko, "Singular phase nano-optics in plasmonic metamaterials for label-free single-molecule detection", *Nature Materials*, 12, 304-309, 2013.

- **B. D. Thackray**, V. G. Kravets, F. Schedin, R. Jalil and A. N. Grigorenko, "Resistive coupling of localised plasmon resonances in metallic nanostripes through a graphene layer", *Journal of Optics*, 15, 114002, 2013.

- V. G. Kravets, R. Jalil, Y.-J. Kim, D. Ansell, D. E. Aznakayeva, **B. D. Thackray**, L. Britnell, B. D. Belle, F. Withers, I. P. Radko, Z. Han, S. I. Bozhevolnyi, K. S. Novoselov, A. K. Geim and A. N. Grigorenko, "Graphene-protected copper and silver plasmonics", *Scientific Reports*, 4, 5517, 2014.

- V. G. Kravets, F. Schedin, G. Pisano, **B. D. Thackray**, P. A. Thomas, A. N. Grigorenko, "Nanoparticle arrays: From magnetic response to coupled plasmon resonances", *Physical Review B*, 90, 125445, 2014.

- **B. D. Thackray**, V. G. Kravets, F. Schedin, G. H. Auton, P. A. Thomas, A. N. Grigorenko, "Narrow collective plasmon resonances in nanostructure arrays observed at normal light incidence for simplified sensing in air and water environments", ACS Photonics, 1, 1116-1126, 2014

- V. G. Kravets, O. P. Marshall, R. R. Nair, **B. D. Thackray**, A. Zhukov, J. Leng, A. N. Grigorenko, "Engineering optical properties of a graphene oxide metamaterial assembled in microfluidic channels" Submitted to Optics Express; in press.

- **B. D. Thackray**, G. H. Auton, P. A. Thomas, V. G. Kravets, A. N. Grigorenko, "Super-narrow, high Q plasmon resonances from gold nanostripe arrays on a gold sublayer" Manuscript prepared; on hold pending inclusion of latest results from the group (title and author list subject to change).

Conferences

- B. D. Thackray, V. G. Kravets, F. Schedin, R. Jalil and A. N. Grigorenko, "Resistive coupling of localised plasmon resonances in metallic nanostripes through a graphene layer", *Proceedings of the IEEE Conference on Nanotechnology*, 6322221, 2012, Conference proceeding and poster presentation, *IEEE Nanotechnology 2012*, Birmingham, UK.
- "Improving fabrication of structures for cascaded enhancement of plasmon resonances", Poster presentation, *Metamaterials 2012*, St. Petersburg, Russia.
- "Resistive coupling of localised plasmon resonances in metallic nanostripes through a graphene layer", Poster presentation, *Graphene Nanophotonics*, Benasque, Spain.
- "Narrow collective plasmon resonances in nanostructure arrays observed at normal light incidence for simplified sensing in asymmetric air and water environments*"*, Oral presentation, *META'14*, Singapore.
- NOWNano summer conferences - Yearly updates, Oral and poster presentations, Cheshire, UK.

LOA

AOI	Angle of incidence
CMOS	Complementary metal-oxide-semiconductor
CVD	Chemical vapour deposition
CVP	Cresyl violet perchlorate
FDTD	Finite difference time domain
FOM	Figure of merit
FWHM	Full width half maximum
IPA	Isopropyl alcohol
IR	Infra-red
LOA	List of abbreviations
LSPR	Localised surface plasmon resonance
MIBK	Methyl isobutyl ketone
NA	Numerical aperture
NIR	Near infra-red
PMMA	Poly(methyl methacrylate)
RIU	Refractive index unit
SEFS	Surface enhanced fluorescence spectroscopy
SEM	Scanning electron microscope
SERS	Surface enhanced Raman spectroscopy
SNOM	Scanning near-field optical microscope
SPP	Surface plasmon polariton
SPR	Surface plasmon resonance
UV	Ultra-violet

Abstract

Coupling of Localised Plasmon Resonances

Benjamin David Thackray

The University of Manchester

15th December 2014

Plasmon resonances have attracted a lot of recent research interest for their potential applications, including bio-sensing, sub-wavelength optics, negative refractive index metamaterials and their ability to produce massively enhanced electromagnetic fields. Localised surface plasmon resonances (LSPR) in metallic nanostructures can offer large electromagnetic field enhancements, and nanometre-scale localisation of electric fields. Their resonance wavelengths and properties can be tuned by variation of the nanostructure geometry and are sensitive to environmental refractive index. Coupling of localised plasmon resonances can: Create new hybrid modes that cannot be supported by individual nanostructures, overcome some of the limitations of individual LSPR, and open up possibilities for new applications and active control of plasmon resonances.

This thesis contains results from samples exploiting near-field, far-field and resistive coupling of localised plasmon resonances to create novel resonance modes that may make them suitable for important applications.

Firstly results are presented from samples exhibiting strong collective plasmon resonances at normal incidence, which could be used to improve the spatial resolution of, miniaturise and add new functionality to highly sensitive surface plasmon resonance based approaches to bio-sensing. A very high bio-sensing figure of merit is calculated for the nanostructure arrays fabricated.

Results are also presented from samples designed to produce the highest quality factor resonances possible when excited with light at grazing incidence. The highest resonance quality factors measured were conservatively estimated to be > 210, which to our knowledge are the highest values of quality factor measured in diffraction coupled arrays at the resonance wavelengths around 1.5 μm.

Evidence for the existence of a presently largely unrecognised resistive coupling mechanism is also presented from an array of gold nanostripes covered with a graphene layer. If further work is successful, this could allow extremely rapid modulation of the optical properties of a plasmonic array by application of gate voltage to the graphene layer.

Finally an improvement to the fabrication procedure for established near-field coupled composite plasmonic nanostructures that create a cascaded electromagnetic field enhancement effect is presented.

Declaration

I declare that no portion of the work referred to in the thesis has been submitted in support of an application for another degree or qualification of this or any other university or other institute of learning.

Benjamin David Thackray

15th December 2014

Copyright Statement

Acknowledgements

Many people have helped me throughout my PhD and I am inevitably going to omit some names here. Firstly, I owe a massive thank you to Vasyl Kravets, for hours spent selflessly helping and training me, from the beginning of and throughout my PhD. I owe much thanks to Fred Schedin and Gregory Auton for the assistance and advice they gave me with sample fabrication, not to mention their patience, as well as further thanks to Fred and Alexander Zhukov for additional training. I am indebted to Philip Thomas and Owen Marshall for the help they have given me with measurements, as well as Francisco Rodriguez and Rashid Jalil for their assistance in sample fabrication. Daniel Ansell has been a friend, travel partner, and general bosom buddy throughout my PhD. I would also like to thank Irina Grigorieva and the NOWNano DTC, from which I have received excellent training, friends, and funding, as well as the larger condensed matter/ graphene group as a whole, who are all lovely, helpful and friendly people.

Sasha Grigorenko has been the most patient, friendly, knowledgeable and helpful supervisor anyone could hope for, and I am immensely grateful towards him for his supervision and expertise. Plus he paid my conference expenses.

Beyond my academic life, Damien Jeanmaire, Jennifer Wedgwood, David Green and Michael Bramhall are four of the best friends I have ever had, out of a list of too many great friends to name that have shaped my life and experiences in Manchester.

Finally I am of course eternally indebted to my awesome parents and siblings; Graham, Janet, Laura and Robert Thackray. I love you all.

Fred and Edward are also awesome.

My background

I studied for a BSc in Physics at Bristol university, graduating in 2009. I then studied for an MSc in Nanoscale Science and Technology at the universities of Leeds and Sheffield, graduating from Leeds in 2010. I then immediately joined the NOWNano doctoral training centre at The University of Manchester, where I had six months of lectures and training, before starting the 3.5 year PhD project which produced this thesis.

To Albert; Cat (deceased).

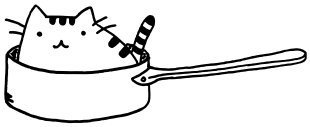

Chapter 1

Introduction

Plasmons are resonances of the free electron plasma in metals. Surface plasmons are resonances at interfaces between metals and dielectrics, and have generated significant interest for their potential applications, including bio-sensing, sub-wavelength optics, negative refractive index metamaterials and their ability to produce massively enhanced electromagnetic fields.

Surface plasmon resonances have been exploited since ancient Roman times, when metal nanoparticles were used to colour glass. A famous example can be seen in the Lycurgus Cup from around 300 AD (currently at the British museum) which is green in reflection, but red in transmission. Localised plasmon resonance - the physical reason for the vivid colours observed in metal colloids - was not understood until many centuries later. The physics of the localised plasmon resonances responsible for the optical properties of subwavelength nanoparticles are discussed in section 1.4.

A second type of surface plasmon resonance is delocalised, propagating resonance at the interface of dielectrics and semi-infinite surfaces or gratings. The first clue to the existence of these surface plasmon modes was spotted by R. W. Wood in 1902, who observed anomalous dispersion in the spectra of metal diffraction gratings, in the form of nearby bright and dark bands[1]. These were termed 'Wood's anomalies'. While Wood documented some important properties of the resonances, such as the fact that they are only excited by $p-$polarised light, their physical origin was not understood. Wood observed two types of anomaly, one sharp and one diffuse. Lord Rayleigh provided an explanation of the sharp anomalies in 1907[2], which are now often known as 'Rayleigh anomalies'. However the diffuse anomalies which consisted of nearby bright and dark bands proved more elusive. Eventually in 1941, Fano[3] spotted the connection between this problem and that in a 1909 paper concerning radio wave propagation. Sommerfeld[4] had studied the solutions of Maxwell's equations for radio waves at the interface between the air and the earth (as had Zenneck in 1907[5]), and demonstrated the existence of surface waves that could guide the wave around the curvature of the earth. Fano realised the equivalence of the problem and generalised the solution to optical frequencies. Pines and Bohm were among the

first to model the electron plasma hydrodynamically and study its modes[6], and R. H. Ritchie[7] was the first to predict the existence of quantised surface plasmons in 1957 in an attempt to explain the electron energy loss spectra of metallic thin films. It was in this quantum mechanical framework which the 'plasmon' was christened[8]. As the electromagnetic modes of the vacuum are quantised as the photon and the vibrations of a crystal lattice by the phonon, so the modes of an electron plasma can be quantised as the plasmon. No metal exists where the free electrons do not experience some form of damping, so plasmons are always quasiparticles, and the best 'plasmonic' metals are thus those with the least damping and highest conductivity, such as gold and silver (see section 1.8). Since these waves require an oscillating electromagnetic field in the air as well as electron oscillation in the metal, they are often referred to as surface plasmon polaritons (SPPs).

1.1 Surface plasmon polaritons

The existence of surface plasmon polaritons and some of their properties can be deduced from the study of Maxwell's equations. This derivation is based on the more detailed descriptions given in references [8] and [9]. Beginning with Maxwell's equations in their macroscopic form, we assume that the medium is:

- Linear in its response to the excitation. This will fail for large amplitude excitations but should be valid for small amplitude excitations.
- Infinite and isotropic, i.e. ϵ depends only on ω, not spatial coordinates or momentum.
- Non-magnetic, i.e. $\mu = 1$.
- Local, meaning that the response at any given point is dependent only on the history of the excitation at that point. In other words, we have no spatial dispersion, just temporal dispersion.

Since most situations relevant to my work involve coherent, continuous excitation, it is convenient to use complex notation. For a field oscillating at frequency ω, time dependence can be modelled with an $e^{-i\omega t}$ factor, which simplifies differentiation in time to multiplication by $-i\omega$.

Hence, we work with Maxwell's equations in the form

$$\begin{aligned} \nabla \cdot \underline{\mathbf{H}}(r,\omega) = 0 \qquad & \nabla \cdot \underline{\mathbf{D}}(r,\omega) = 0 \\ \nabla \times \underline{\mathbf{E}}(r,\omega) = i\omega\mu_0 \underline{\mathbf{H}}(r,\omega) \qquad & \nabla \times \underline{\mathbf{H}}(r,\omega) = -i\omega \underline{\mathbf{D}}(r,\omega) \end{aligned} \tag{1.1}$$

and the constitutive equation describing the response of the medium

$$\underline{\mathbf{D}}(r,\omega) = \epsilon_0 \epsilon(\omega) \underline{\mathbf{E}}(r,\omega) \tag{1.2}$$

where $\epsilon(\omega)$, the dielectric function of the medium, is complex. The real part of ϵ, ϵ', relates to the energy stored in the medium, and the imaginary part, ϵ'', to the energy dissipated[1].

In this simplified situation where the medium is approximated as linear, isotropic, non-magnetic and local in its response to excitation, the dielectric function $\epsilon(\omega)$ and Maxwell's equations contain all the information needed to describe the electromagnetic modes of the system.

1.1.1 Boundaries and dispersion

Surface plasmons occur at the boundary between a metal and a dielectric. We consider a boundary between a semi-infinite dielectric for $z > 0$ and a metal for $z < 0$.

For light with polarisation direction in the (x, z) plane, which is also the plane of incidence[2], we define the **H** and **D** fields in each medium as[3]

$$\underline{\mathbf{H}}_D = \begin{pmatrix} 0 \\ \mathrm{H}_{Dy} \\ 0 \end{pmatrix} e^{ik_{Dx}} e^{ik_{Dz}} e^{-i\omega t} \qquad \underline{\mathbf{H}}_M = \begin{pmatrix} 0 \\ \mathrm{H}_{My} \\ 0 \end{pmatrix} e^{ik_{Mx}} e^{-ik_{Mz}} e^{-i\omega t}$$

$$\underline{\mathbf{D}}_D = \begin{pmatrix} \mathrm{D}_{Dx} \\ 0 \\ \mathrm{D}_{Dz} \end{pmatrix} e^{ik_{Dx}} e^{ik_{Dz}} e^{-i\omega t} \qquad \underline{\mathbf{D}}_M = \begin{pmatrix} \mathrm{D}_{Mx} \\ 0 \\ \mathrm{D}_{Mz} \end{pmatrix} e^{ik_{Mx}} e^{-ik_{Mz}} e^{-i\omega t} \tag{1.3}$$

Using $\nabla \times \underline{\mathbf{H}}(r,\omega) = -i\omega \underline{\mathbf{D}}(r,\omega)$, we find that in the dielectric

$$\nabla \times \underline{\mathbf{H}}_D = \begin{pmatrix} -\frac{\partial \mathrm{H}_{Dy}}{\partial z} \\ 0 \\ \frac{\partial \mathrm{H}_{Dy}}{\partial x} \end{pmatrix} = -i\omega \begin{pmatrix} \mathrm{D}_{Dx} \\ 0 \\ \mathrm{D}_{Dz} \end{pmatrix} \tag{1.4}$$

so

$$k_{Dz}\mathrm{H}_{Dy} = \omega \mathrm{D}_{Dx} \tag{1.5}$$

and similarly, in the metal

$$k_{Mz}\mathrm{H}_{My} = -\omega \mathrm{D}_{Mx}. \tag{1.6}$$

Knowing that $\underline{\mathbf{D}}(r,\omega) = \epsilon_0 \epsilon(\omega) \underline{\mathbf{E}}(r,\omega)$, and the boundary conditions $\mathrm{H}_{Dy} = \mathrm{H}_{My}$ and

[1] The constitutive equation is closely related to the Fourier transform of the polarisation response function - a convolution of previous excitation and current excitation. The components of the excitation and response which are in phase will Fourier transform to real quantities, and those which are out of phase transform to imaginary.

[2] This is known as TM (transverse magnetic) or $p-$polarised light. Light with polarisation at 90°to this, perpendicular to the plane of incidence and in the (x, y) plane is known as TE (transverse electric) or $s-$polarised.

[3] The waves in both metal and dielectric in the $z-$direction are evanescent, with the field amplitude decaying exponentially away from the surface, hence the differing sign on their k_z vectors

$E_{Dx} = E_{Mx}$, we deduce from 1.5 and 1.6 that

$$\frac{k_{Dz}}{k_{Mz}} = -\frac{\epsilon_D}{\epsilon_M}. \tag{1.7}$$

Using the electromagnetic wave equation $\left(\nabla^2 - \frac{\mu_D \epsilon_D}{c^2}\frac{\partial^2}{\partial t^2}\right)\underline{\mathbf{D}}_D = 0$ (for non-magnetic media) we find

$$k_x^2 + k_{Dz}^2 = \epsilon_D \left(\frac{\omega}{c}\right)^2 \tag{1.8}$$

and similarly for the metal

$$k_x^2 + k_{Mz}^2 = \epsilon_M \left(\frac{\omega}{c}\right)^2. \tag{1.9}$$

Substituting for k_{Dz} from equation 1.7

$$k_x^2 = \epsilon_D \left(\frac{\omega}{c}\right)^2 - \left(\frac{\epsilon_D}{\epsilon_M}\right)^2 k_{Mz}^2$$

and then substituting for k_{Mz}^2 from 1.9 to get an equation solely in terms of k_x and ω and rearranging, we find the surface plasmon dispersion equation at the boundary of two semi-infinite media.

$$k_x = \frac{\omega}{c}\sqrt{\frac{\epsilon_D \epsilon_M}{\epsilon_D + \epsilon_M}}. \tag{1.10}$$

This equation has a maximum of k_x when $\epsilon_D = -\epsilon_M$, which represents the surface plasmon resonance frequency at $\omega = \omega_{SP}$. For an idealised metal with no damping, and thus no imaginary component of ϵ_M, k_x would tend to infinity as $\omega \to \omega_{SP}$, however in real metals the damping constrains and broadens the resonance peak.

1.2 The microscopic response of the medium

Metals such as gold and silver that are well suited for plasmonic applications are well described by the Drude model. In this picture, the metals consist of fixed ion cores, surrounded by freely moving conduction electrons. The electrons do not interact with one-another, but occasionally collide instantaneously and elastically with the ion cores. The Drude model can be derived as a special case of the Lorentz model of the optical polarisability.

1.2.1 The Lorentz model

The Lorentz model of the optical polarisability[8] treats a medium as a collection of classical driven damped harmonic oscillators. For an oscillator of mass m, natural frequency ω_0 and damping coefficient γ, displaced from equilibrium a distance $\mathbf{r}$ (assumed small) by force F,

$$F = m\left(\frac{d^2\mathbf{r}}{dt^2} + \gamma\frac{d\mathbf{r}}{dt} + \omega_0^2\mathbf{r}\right) = -e\mathbf{E} \tag{1.11}$$

For our case the displacing force is created by an electric field **E**, and acts on electron charge e. Using complex notation for **E** and **r** oscillating at a single frequency ω with time dependence contained in a $e^{-i\omega t}$ factor, and substituting m by the electron effective mass m^* we find

$$\mathbf{r} = \frac{-e\mathbf{E}}{m^*\left(-\omega^2 - i\gamma\omega + \omega_0^2\right)}. \tag{1.12}$$

The complex dipole moment **p** induced by the charge separation **r** is $\mathbf{p} = -e\mathbf{r}$. The linear polarisability α is defined as $\mathbf{p} = \alpha\mathbf{E}$, i.e.

$$\alpha = \frac{e^2}{m^*\left(-\omega^2 - i\gamma\omega + \omega_0^2\right)} \tag{1.13}$$

The macroscopic polarisation of a medium **P** is linked to its dielectric function by $\epsilon(\omega) = 1 + \frac{\mathbf{P}}{\epsilon_0\mathbf{E}}$. Assuming that oscillators are non-interacting, we can simply sum all the individual microscopic polarisabilities to find **P**. So for n electrons, $\mathbf{P} = n\alpha\mathbf{E}$ and

$$\epsilon(\omega) = 1 + \frac{ne^2}{m^*\epsilon_0\left(-\omega^2 - i\gamma\omega + \omega_0^2\right)} \tag{1.14}$$

1.2.2 The Drude model

The Drude model is simply a special case of the above. In the Drude model, the delocalised conduction electrons move without any restoring force, in other words, $\omega_0 = 0$. We then have

$$\epsilon(\omega) = 1 - \frac{ne^2}{m^*\epsilon_0\left(\omega^2 + i\gamma\omega\right)} \tag{1.15}$$

The factor $\frac{ne^2}{m^*\epsilon_0}$ multiplying the second term on the right hand side has units of s^{-2}, and its square root represents $\omega_p = \sqrt{\frac{ne^2}{m^*\epsilon_0}}$, the bulk plasma frequency of the metal. We therefore have a frequency dependent dielectric function

$$\epsilon(\omega) = 1 - \frac{\omega_p^2}{\omega^2 + i\gamma\omega} \tag{1.16}$$

The effect of inter-band transitions can be roughly accounted for by introducing a factor ϵ_{int}.

$$\epsilon(\omega) = \epsilon_{int} - \frac{\omega_p^2}{\omega^2 + i\gamma\omega} \tag{1.17}$$

However close to inter-band transitions the Drude model will fail[10].

The resonances of the bulk plasma at ω_P (i.e. ω when $\epsilon(\omega) = 0$ for no damping) are of little relevance to my work, as they do not couple to light. Substituting equation 1.16 into 1.10 and rearranging yields that for a perfect Drude metal (with no damping, i.e. $\epsilon" = 0$) in air ($\epsilon_D = 1$), resonance (where $k_x \to \infty$) occurs at $\omega_{SP} = \omega_P/\sqrt{2}$.

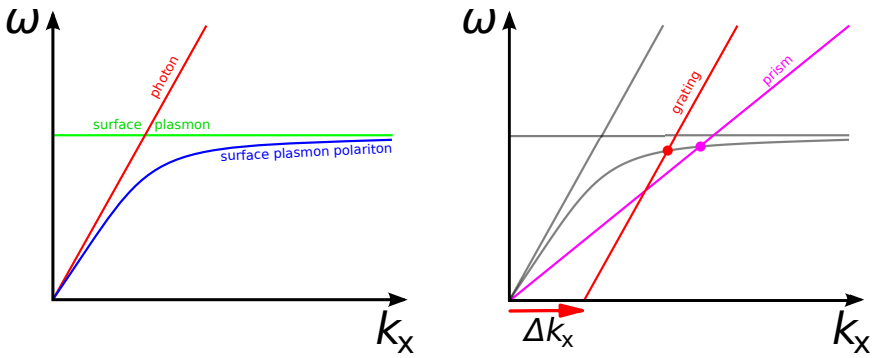

Figure 1.1 – Left: Comparison of the dispersion relations of free-space photons, non-radiative surface plasmons and surface plasmon polaritons. Note that the photon and SPP lines do not intersect anywhere other than at zero. Right: Two methods of coupling to SPPs. Gratings introduce an additive factor to the wave-vector of the free-space photons, while a prism multiplies the wavevector by the refractive index.

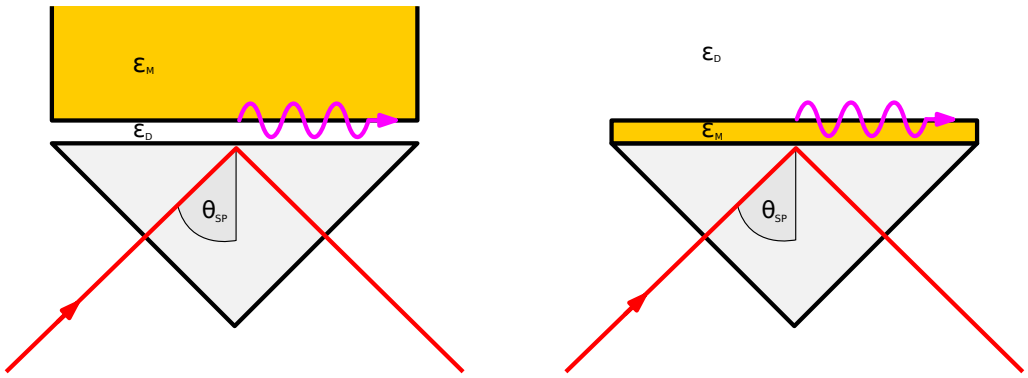

Figure 1.2 – The Otto[11] (left) and Krestchmann[12] (right) configurations for coupling light to surface plasmons using a prism.

1.3 Exciting surface plasmons

SPPs can be excited directly by electrons, but for most applications optical excitation is more practical. Coupling freespace photons to surface plasmon resonances is more tricky because their momentum is always smaller than that of a plasmon at the same frequency. Figure 1.1 plots the dispersion relations for photons in a vacuum ($\omega = ck$) and surface plasmon polaritons at the interface between two semi-infinite media (1.10), which do not cross. Despite this, methods exist to overcome the momentum mismatch and couple light to these SPP modes.

1.3.1 Prism coupling

Light travelling in a medium of refractive index n has its wavevector multiplied by a factor of n relative to its wavevector in free-space. By placing a prism close to a suitable metal film, the evanescent waves generated by total internal reflection can excite plasmon resonances at the interface between the film and dielectric. The two most common geometries for this are the Otto[11] and Krestchmann[12] configurations (figure 1.2). The two differ only in the relative positions of the interfaces. The

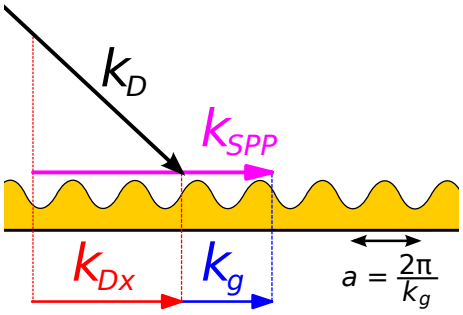

Figure 1.3 – Grating coupled surface plasmon polaritons.

angle at which the surface plasmon is excited is strongly dependent on ϵ_D of the environment close to the interface. If something is adsorbed on the surface of the metal, the change in ϵ_D is detectable as a shift of the resonance angle θ_{SP}, making the Krestchmann configuration popular for sensing applications. The Krestchmann configuration is favoured over the Otto, as it is more simply realised practically, and the exposed gold surface can easily be functionalised and exposed to a solution and analyte.

1.3.2 Grating coupling and surface roughness

Surface structure can introduce an additive factor to the photon momentum. Denoting the photon wavevector in the dielectric (at a frequency ω) k_{Dx} and the surface plasmon wavevector at the same frequency k_{sp}, we need additional wavevector Δk_x such that

$$k_{Dx} + \Delta k_x = k_{sp} \tag{1.18}$$

For an photon in air incident at angle θ to the surface normal

$$\frac{\omega}{c}\sin\theta + \Delta k_x = k_{sp} \tag{1.19}$$

One way to provide this extra Δk is to fabricate a grating on the metal surface, with period $a = \frac{2\pi}{k_g}$ such that $nk_g = \Delta k$, i.e.

$$\frac{\omega}{c}\sin\theta + nk_g = k_{sp} \tag{1.20}$$

is satisfied for integer n.

Similarly, surface roughness can also allow coupling of light to plasmons. Surface roughness can be viewed as a superposition of many gratings of various periods, which may provide appropriate Δk_x. Both gratings and roughness can also work in reverse, and convert surface plasmons into radiated photons. Point defects and point sources such as a SNOM tip can also be used to excite propagating plasmons, as

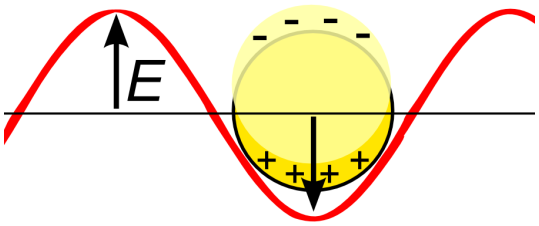

Figure 1.4 – Schematic diagram of localised plasmon resonance of a spherical metallic nanoparticle. An incident electromagnetic field E will cause the free negatively charged electrons to move in the opposite direction to the applied field, creating a build up of negative charge at one surface. The fixed positive ion cores on the opposite side will then lack electrons to neutralise their positive charges, and this build up of net positive charge will then create a restoring force. This results in an induced oscillating dipole with a resonant frequency. If the nanopaticle electron cloud is excited with light at this resonant frequency, then localised surface plasmon resonance is induced, and strong electric fields are created by the moving charges.

they break the translational invariance of the system and thus remove the momentum conservation requirement.

1.4 Localised surface plasmon resonance (LSPR)

A second flavour of plasmon resonance is localised resonances in metallic nanoparticles and nanostructures. Despite colloids of gold, and later other metals, being exploited since Ancient Roman times, it was not until Faraday's studies in the 19th Century[13] that the origin of their colour was studied scientifically. Faraday realised that the colours were linked to the nanoparticle morphologies[14], but was not able to give a full explanation of the phenomenon. Finally in 1908, Mie published a solution of Maxwell's equations for light interacting with spherical particles of size comparable to the light wavelength[15]. Before discussing Mie's solution, it is possible to gain insight from a qualitative picture of LSPR resonances.

1.4.1 Qualitative picture

In non-metallic materials, electrons are typically bound to a nucleus of an atom. If the electrons are displaced slightly by an external electromagnetic field, the positive charge of the nucleus acts as a restoring force to pull them back to equilibrium. This picture of materials as collections of harmonic oscillators is the basis of the Lorentz model (section 1.2.1). In metals the situation is different, as no net restoring force acts on the delocalised electron gas in the bulk of the metal. However surfaces can introduce a restoring force, and for small nanoparticles, surface effects become increasingly significant, and even dominant. If the entire electron gas of the particle is displaced (see figure 1.4), then at the surface on one side of the particle an excess negative charge will accumulate, and at the opposing surface a net positive charge will remain. The attraction between these two opposing charges then acts as a restor-

ing force, pulling the electron cloud back towards equilibrium. This is effectively just a harmonic oscillator, and the optical properties of metal nanoparticles can be qualitatively understood with this picture. Modelling the entire electron cloud of a particle as a single harmonic oscillator; its resonance frequency will be lower if it has higher total mass, and so larger nanoparticles have resonances at longer wavelengths than smaller ones. For large gold particles these resonances lie in the infrared and do little to change the appearance in the visible when excited with white light. For particle diameters of a few hundred nanometres (depending on surrounding medium), the resonance frequency approaches the optical part of the spectrum, absorbing red light and giving colloidal suspensions a blueish colour that becomes more intense with decreasing size. As the resonance crosses the green wavelengths at the centre of the visual spectrum, suspensions turn magenta, and then become increasingly deep red until the particles are only a few nm in size and absorb in the blue to ultra-violet.

1.4.2 Mie's analytical solution for nanospheres

Mie's solution (also known as 'Mie theory') enables precise evaluation of extinction, scattered fields and enhancement factors, but can be very cumbersome[8, 15]. The theory assumes a spherical morphology, that the particle and surrounding medium can each be described by one dielectric function, and that there is a sharp discontinuity in electron density at the particle surface[14]. For a metal sphere of dielectric function $\epsilon_M(\omega)$ in a dielectric medium of dielectric constant ϵ_D in a constant quasi-static external field (assuming a particle diameter smaller than the excitation wavelength, so that retardation effects are negligible) of magnitude $E_{incident}$, the internal field of the sphere is given by[8, 16]

$$E_{internal} = \frac{3\epsilon_D}{\epsilon_M(\omega) + 2\epsilon_D} E_{incident} \tag{1.21}$$

Assuming that the electric potential, φ, (where $E_{incident} = -\nabla\varphi$) and the normal component of the electric displacement are both continuous at the sphere surface as our boundary conditions, the overall polarisability of the nanosphere can be calculated by solving Laplace's equation[14], $\nabla^2\varphi = 0$, giving

$$\alpha = 4\pi\epsilon_0 r^3 \frac{\epsilon_M - \epsilon_D}{\epsilon_M + 2\epsilon_D} \tag{1.22}$$

for a sphere of radius r.

From 1.21 and 1.22 we see that, for a metal with little damping (and therefore a mostly real dielectric function), when $\epsilon_M \approx -2\epsilon_D$ the polarisability will be huge and the field inside the nanoparticle will be greatly enhanced. For a hypothetical perfect Drude metal, the enhancement factor would tend to infinity. It is the damping ($\mathrm{Im}(\epsilon_M(\omega))$) which constrains the amplitude and broadens the resonances. The resonance wavelength depends on the frequency dependent dielectric function $\epsilon_M(\omega)$ of

the metal as well as ϵ_D of the environment. Similar to SPP resonances, this sensitivity to the dielectric constant/ refractive index of the environment is the basis of LSPR biosensing techniques. For excitation frequencies significantly larger than the dipolar surface plasmon resonance of the particle the deviation between nanoparticle and thin film behaviour decreases, as other effects such as inter-band transitions begin to dominate the optical properties[17]. The resonances of sub-wavelength nanostructures depend strongly on the morphology of the structures, and analytic solutions of Maxwell's equations only exist for simple geometric shapes. More complicated structures typically lack analytical solutions. In these cases, finite element computer simulation can be used to help predict the resonances.

1.4.3 Exciting localised plasmons

For sub-wavelength metallic structures, the problem is no longer translationally invariant, removing the requirement of k_x conservation. Consequently light of the right frequency is easily coupled to the resonance modes of subwavelength structures and nanoparticles, for example light at frequency ω close to that where $\epsilon_M(\omega) \approx -2\epsilon_D$ can be used to excite dipolar resonance.

1.5 Near and far field coupling of localised plasmon resonances

Localised plasmon resonances involve moving charges, which create their own electromagnetic fields as they oscillate. Plasmonic resonators placed in close proximity will interact via the fields they create, either in the near or far field, or some combination of both. Various geometrical and environmental parameters can control the nature of the interaction, and can significantly modify the resonance modes, in some cases broadening them or suppressing resonances, in some cases strengthening them or creating new resonance modes.

1.5.1 Near field coupling

Near field coupling occurs when plasmonic resonators are placed within a few hundred nanometres of one-another. This can be most basically understood in the same qualitative picture discussed in section 1.4.1. If two metal nanostructures are placed in close proximity and subjected to an external electromagnetic field, the induced electron motion in the structures will create areas of electron accumulation, with net negative charge, and areas of electron outflow, with net positive charge, in each structure. The conduction electron clouds will not only interact with the charge distribution of their host nanostructure, but also of that in the other nanostructure in close proximity (figure 1.5). Another simple approach is to consider the two resonators as dipoles, with dipole moments p_1 and p_2, and interaction energy $V \propto p_1 p_2 / d^3$, where d is separation[18]. This energy becomes significant when the separation is comparable

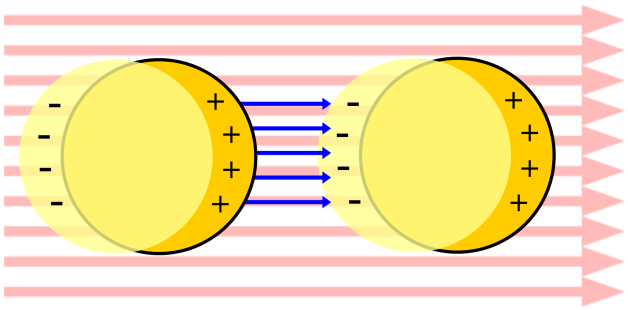

Figure 1.5 – A simple schematic of near-field interactions between plasmon resonances in nanostructures. The applied electric field is shown in red, and enhanced field in blue.

to the nanoparticle size, and will shift the resonant frequencies of each structure, creating low energy and high energy hybrid modes, where the dipoles are aligned parallel or anti-parallel respectively (often termed referred to as 'bonding' and 'antibonding' modes in analogy with molecular orbitals)[18]. The bonding mode has a large net dipole moment, and typically couples well to incident light. Since the antibonding dipole moments cancel each other, these modes have no, or a weak, net dipole, and so are 'dark' modes that do not generally couple well to light[18]. An exception to the previous remark and interesting application of nanoplasmonic dimers was achieved by using tapered, asymmetrical nanostructures to form dimers with an antibonding mode with a net dipole that can couple to incident light[19]. Since the antibonding mode involves adjacent charges moving in opposite directions, it is effectively a circulating charge, and thus produces a magnetic field at optical frequencies. Near field coupling is also exploited in more complex composite nanostructures, such as clusters, coupled nanorods, and structures for cascaded enhancement (section 5.1).

1.5.2 Surface enhanced spectroscopy

Early investigations of near-field coupling of plasmonic nanostructures were closely linked with the discovery and development of two of its major applications - surface enhanced fluorescence spectroscopy (SEFS), and surface enhanced Raman spectroscopy (SERS). The physics of the fluorescence and Raman processes themselves are discussed in section 1.10.1, here I will discuss the history and physics of the enhancement from strong fields near near-field coupled nanostructures.

1.5.2.1 A history

M. Fleischmann *et al.* were the first to observe SERS in 1974 while studying the adsorption of pyridine on roughened silver electrodes[20]. They did not recognise the significance of the enhancement, and merely commented on the importance of preparing high-surface area electrodes to acquire good spectra[20]. By 1977, both Albrecht and Creighton[21] and Jeanmaire and Van Duyne[22] had independently recognised that more was at work than just increased surface area[23]. Albrecht and

Creighton noticed a 5-fold increase in signal intensity for an increase in surface roughness of only 10-20%. Using the relative intensities of the Raman spectra and estimates of the number of molecules in solution and adsorbed at the surface, they estimated an enhancement of about 10^5 times at the metal surface compared to in solution above it[21]. They suggested a charge-transfer mechanism may be responsible for the enhancement. Jeanmaire and Van Duyne measured enhancement of 10^{5-6} times, much more than could be accounted for by the increase in surface area, and suggested an electromagnetic explanation for the enhancement. Controversy regarding the origin of the effect persisted for some time[24], until eventually consensus formed that while both mechanisms contribute to the enhancement, the electromagnetic effect is most significant[25]. Methods for calculation of enhancement factors can sometimes be a contentious issue, but enhancement factors of the order of 10^{10-11} are routinely reported, and may even in many cases be under-estimated due to assumptions about the number of participating molecules[26]. Single molecule SERS on colloidal silver nanoparticles was first observed in 1997, again by two groups independently[27, 28]. This contributed to a renewed interest in SERS for its applications in sensing, analytical chemistry, and biomedical applications[29]. Single molecule Raman would be practically impossible to observe without the huge enhancement factors that SERS can provide. Single molecule Raman cross sections are typically $\sim 10^{-29}$ cm^2, meaning that for excitation with a (relatively high power) 100 mW laser focused to 1 μm^2, one would expect to have to wait over an hour just to produce a single Raman scattered photon[26].

The discovery of SERS was the first practical application of surface plasmon resonances, and along with the discovery of anomalously high transmission through hole arrays, helped initiate a renaissance of interest and scientific investigation of surface plasmon resonance. Along with this, the advances in nano-fabrication techniques, particularly in scanning electron beam lithography and microscopy, allowed fabrication of nanostructures with well defined geometry and morphology that would not have been possible before the advent of these techniques.

1.5.2.2 Field enhancement

The mechanism of field enhancement in the vicinity of sub-wavelength metallic nanoparticles is quite easily understood qualitatively in the electrostatic approximation. An applied electric field will exert a force on the electron cloud of the nanoparticle, in the direction antiparallel to the field direction. Since the electric field at a given location is defined as the force exerted on a positively charged test particle at that location, we imagine such a particle near the nanoparticle surface. A test particle near the displaced electron cloud will see a net negative charge and be attracted towards it. Similarly the test particle near the positively charged ion cores which have been temporarily stripped of their electrons will be repelled. These extra attractive or re-

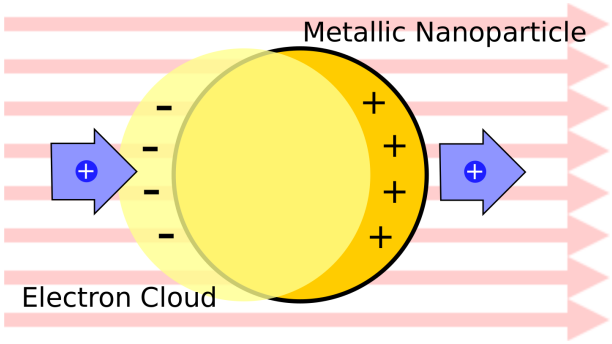

Figure 1.6 – Localised surface plasmon resonances in a metal nanosphere in a quasi-static external electric field (red). The blue arrows show the additional local forces on a small positively charged test particle near the surface of the nanoparticle. The forces are in the same direction as the incident field, i.e. the field is enhanced.

pulsive forces act in unison with the external field and account for the field enhancement (figure 1.6). Field enhancement also exists for propagating SPP resonances, but is comparatively modest, reaching a maximum enhancement factor of about 3 at a planar interface[8]. One slight advantage over the localised case is that enhancement is uniform all over the surface.

It was not long after the discovery of SERS that it was noticed that the largest enhancements on irregular colloidal or roughened surfaces occur randomly at 'hot-spots'. Further study of colloidal silver nanoparticles, revealed that these hot-spots occurred on particles with complex, red-shifted spectra with multiple peaks[18] - a hallmark of near-field coupled plasmon resonances. Further studies corroborated this evidence, proving the importance of near-field coupling for SERS enhancement[18].

A key challenge of SERS, especially for single molecules, is reproducibility. Additionally, SERS spectra tend to be unstable in time, and will flicker and sometimes disappear entirely[29]. Some attempts to overcome this irreproducibility include efforts to improve control over colloidal synthesis[30], sometimes employing self-assembly to regulate the surface structure[31, 32]. This has seen some success, but as a fundamentally statistical technique, its predictability tends to be limited. Significant improvements in nanofabrication techniques such as electron beam lithography and reactive ion etching in the last two decades have enabled the patterning of regular surface nanostructures. This has allowed significant improvements in SERS reproducibility, and resulted in a move towards rational design of regular structures for maximum control over enhancement[33, 34, 35]. One such example is the structures for cascaded enhancement in chapter 5 of this thesis.

1.5.2.3 The mechanism of SEFS and SERS

The electromagnetic, plasmonic, contribution to fluorescence and Raman enhancement (section 1.10.1) is nowadays well understood[36]. The underlying theoretical treatment is complicated, but a useful 'rule of thumb' can be developed by model-

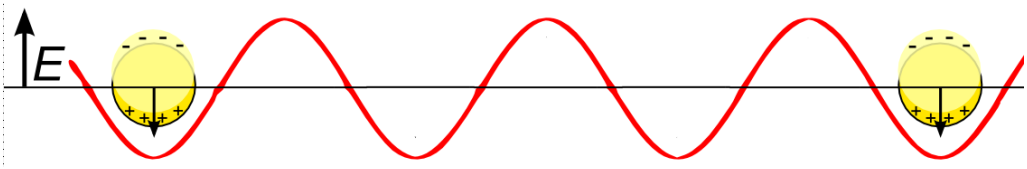

Figure 1.7 – Radiative coupling of LSPR.

ling the process as a form of dipole radiation[37]. The enhancement of fluorescence and Raman scattering is considered in two stages - enhancement of absorption and enhancement of radiation[4]. We imagine that the local electric field, $\mathbf{E}_{loc}$, excites a dipole in the molecule, that has a given (small) probability of radiating Stoke's shifted light. Both excitation and emission are then proportional to the square of this dipole moment, which is in turn linearly proportional to the local field, $\mathbf{E}_{loc}$,which creates it. Hence both processes are enhanced by a factor $\mathbf{E}_{loc}^2/\mathbf{E}_{inc}^2$ or $\tilde{E}^2$, where $\tilde{E} = \mathbf{E}_{loc}/\mathbf{E}_{inc}$ is defined as the local field enhancement factor. For Raman enhancement, this results in an overall enhancement $\sim \tilde{E}^4$. For fluorescence we may expect the same, but this is not the case. Every electron excited to a Raman virtual-state will decay via a Raman process. This is not the case for fluorescence. Since fluorescence is a true two step process, it competes with other modes of decay, which are also enhanced by a factor which is of very similar magnitude. This effectively cancels out one of the enhancement steps, resulting in overall enhancement that is closer to $\sim \tilde{E}^2$. For fluorophores on top of planar metal films, coupling to the SPP modes can occur and in fact significantly quench the fluorescence[38].

This simple dipole picture neglects that absorption and emission occur at different frequencies. This distinction may not be significant for small Stoke's shifts, but as the size of the shift increases will become increasingly problematic. As might be expected, optimal conditions for surface enhanced Raman scattering tend to occur when the surface plasmon resonance frequency of a structure lies half-way between the excitation wavelength and that of the Raman scattered light[39]. The approximation can also fail when calculating depolarisation ratios[40]. Many other factors can affect the real enhancement factor observed, however it has been shown experimentally that the $|E|^4$ approximation is often adequate[37, 40]. Also, while it may not seem appropriate to use dipolar emission to model stochastic spontaneous emission which governs fluorescence, the approach is experimentally well justified. It can be shown that the quantum mechanical treatment predicts an average radiated power that differs only by a constant factor of 4[8].

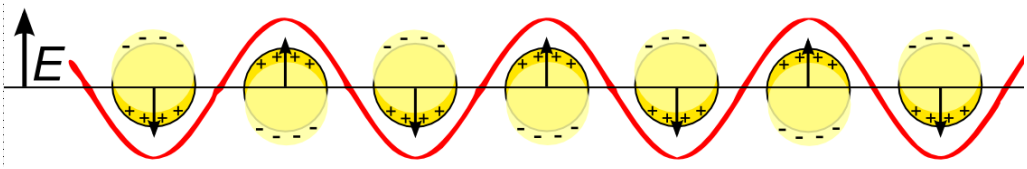

Figure 1.8 – Collective, Diffraction coupled plasmon resonances. Diffraction coupling occurs when nanostructures are spaced so that the scattered field from each structure arrives in phase with the electron oscillations in its neighbours. The scattered light is then recaptured as electron oscillation, reducing energy loss to the far field and retaining it as plasmon resonance, thereby increasing the resonance quality factor.

1.6 Radiative coupling

Plasmon resonances can also couple via their scattered radiation fields. Figure 1.7 depicts a plasmonic nanoparticle dipole scattering radiation, inducing resonance in another several wavelengths away. The underlying principles here are not significantly different to those governing the initial excitation of a plasmonic resonator with an applied external magnetic field, except that the induced oscillating dipole in the second resonator will in turn also scatter light, which will interact with the initial resonator. This effect will of course diminish with distance. In arrays of plasmonic nanoparticles, these interactions can become very significant and lead to the formation of new, collective resonance modes.

1.6.1 Diffraction coupling

The fundamental ideas behind diffraction coupling and the coupled dipole model can be seen in many papers, such as those by Carron *et al.* [41], and Markel *et al.*[42] in the 80s and 90s, but the idea was not fully developed or experimentally realised. A 2004 paper by Schatz *et al.*[43] focussed on the extremely narrow resonances predicted by the theory, and stimulated a number of further theoretical[44, 45, 46] and experimental[47, 48, 49, 50] studies. These early experimental studies observed some narrowing of the resonances, but it was not until papers by Kravets *et al.*[51] and Auguié *et al.*[52] that the extremely narrow resonances predicted were successfully realised experimentally.

The physical basis of diffraction coupling can be understood quite simply (figure 1.8). If arrays are fabricated so that the Rayleigh diffraction anomalies of the array[2] (where light is scattered into the plane of the array as a diffraction mode crosses from the air into the substrate) and the localised surface plasmon resonance modes of the structures occur at similar wavelengths, then light that would otherwise be scattered to the far-field can be recaptured as electron oscillation in the nanostructures. By using the right combination of nanostructure size and shape and array period, it can be configured so that light that is scattered by each nanostructure into the plane of

[4] Here we are using the quantum picture where Raman scattering involves instantaneous absorption, excitation to a virtual state and decay, see 1.10.1.2.

the array is in phase with the electron oscillation of its neighbour at its point of arrival, so that the scattered light reinforces the electron resonance in the neighbouring structure. Light energy which would otherwise be scattered to the far field and lost is thus recapturing as electron oscillation. Extending this argument to the whole array of interacting nanostructures results in very narrow collective resonance modes that improve with the size of the array (in the limits of spatial coherence of the incident light). Since quality factor Q is intrinsically linked to the ratio of energy retention and loss of an oscillator by

$$Q = \frac{f}{\Delta f} = \frac{\lambda}{\Delta \lambda} = 2\pi \frac{\text{Energy stored}}{\text{Energy dissipated}} \tag{1.23}$$

where f is resonance frequency, λ is resonance wavelength, and Δf and $\Delta \lambda$ are the frequency and wavelength bandwidths (resonance full-width, half-maximum) the quality factor of these resonances is greatly improved[8].

The most important Rayleigh cut-off wavelengths where light is diffracted into the plane of the array occur at

$$\lambda_R = \frac{a}{m}[n \pm \sin(\theta)] \tag{1.24}$$

where a is the array period, m is an integer, n is the refractive index of the surrounding environment (which can be the environment above or within the substrate) and θ is the angle of incidence. Additional resonances may exist, depending on the geometry of the array. For a two dimensional square array for example, the resonances may occur at any

$$\lambda_R = \frac{a}{m}[n\sqrt{p^2+q^2} \pm \sin(\theta)\left\{p\cos(\phi)+q\sin(\phi)\right\}] \tag{1.25}$$

for integer p and q and azimuthal angle ϕ, i.e. the polar angle defining the samples' orientation with respect to the plane of incidence[51].

1.6.1.1 The coupled dipole model

The coupled dipole model[41, 42, 43, 44, 45, 46] was instrumental in the prediction of diffraction coupled resonances, and can also shed light on some of their properties. In an array of N particles, each at position $\mathbf{r}_i$ with polarisability α_i subjected to an external field $\mathbf{E}_{inc}$, a dipole $\mathbf{p}_i$ will be induced in each particle, given by $\mathbf{p}_i = \alpha_i \mathbf{E}_{loc,i}$, where $\mathbf{E}_{loc}$ is the local field at the nanoparticle position $\mathbf{r}_i$. Because each dipole in the array will create its own scattered field, $\mathbf{E}_{loc}$ consists of contributions from both $\mathbf{E}_{inc}$ and $\mathbf{E}_{dipole,i}$, the retarded fields created by the other dipoles. Assuming excitation with a plane wave field $\mathbf{E}_{inc} = \mathbf{E}_0 e^{i\mathbf{k}\cdot\mathbf{r}}$, where $|\mathbf{k}| = \frac{2\pi}{\lambda}$,

$$\mathbf{E}_{loc,i} = \mathbf{E}_{inc,i} + \mathbf{E}_{dipole,i} = \mathbf{E}_0 e^{i\mathbf{k}\cdot\mathbf{r_i}} - \sum_{j=1, j\neq i}^{N} A_{i,j}\cdot\mathbf{p}_j \tag{1.26}$$

for $i = 1,2,...,N$, where A is the dipole interaction matrix[43]. Solving this is long-winded, but by assuming an infinite array of particles with the same induced polarisation, for excitation at normal incidence we arrive at the analytic solution

$$\alpha_{eff} = \frac{1}{1/\alpha - S} \tag{1.27}$$

where S is the retarded dipole sum

$$S = \sum_{j \neq i} e^{ikr_{ij}} \left[\frac{(1 - ikr_{ij})(3\cos^2\theta_{ij} - 1)}{r_{ij}^3} + \frac{k^2 \sin^2\theta_{ij}}{r_{ij}} \right] \tag{1.28}$$

with angle θ_{ij} between r_{ij} and the polarisation direction.

The qualitative description of diffraction coupling above described a situation where light scattered into the plane of the array could reinforce the resonances in neighbouring nanostructures. This corresponds to a situation where the imaginary part of S is negative, partially cancelling the overall positive imaginary component of the complex polarisability which represents radiative damping.

The maximum value of α_{eff} , and therefore extinction ($\sigma_{ext} \propto k\mathrm{Im}(\alpha)$), occurs when α^{-1} and S cancel as much as possible. This condition relies on both the real and imaginary components of α^{-1} and S cancelling, and these values are dependent on the nanoparticle size, array period, and the dielectric functions of the material and environment. The spectral width and quality factor of the diffraction coupled resonances depend not only on α^{-1} and S at the resonance maximum wavelength, but also the profile of the curve either side of the resonance. This is illustrated by example in figure 1.9. The black lines represent components of the inverse polarisability α^{-1} of an isolated nanoparticle of the specified radius, and the red lines represent the components of the dipole sum, S, when the nanoparticles are arranged in a large array. A and B label the Rayleigh anomalies in the substrate and in air respectively. With the aim of creating the highest quality resonances possible in mind, the left hand column, graphs (a-c), depict a non ideal situation, whereas (d-f) predict a near-ideal scenario at the given resonance wavelength. Looking first at the left-hand column, there are two points, P and Q where the real components of α^{-1} and S cancel. These points are close to, but do not perfectly coincide with the Rayleigh anomaly at B. Looking at $\mathrm{Im}(\alpha^{-1})$ and $\mathrm{Im}(S)$, P lies before the step in $\mathrm{Im}(S)$ at B, where the difference between $\mathrm{Im}(\alpha^{-1})$ and $\mathrm{Im}(S)$ is relatively large, and so the cancellation of α^{-1} and S is imperfect and manifests as a small peak in extinction. However, Q lies to the right of the step, where the difference is much closer to zero and therefore the cancellation of α^{-1} and S much closer to perfect. The peak at Q is correspondingly much larger. Because $\mathrm{Re}(\alpha^{-1})$ and $\mathrm{Re}(S)$ cross at a point where the first derivative of $\mathrm{Re}(S)$ is small (in comparison to the case depicted in (d), which we are about to consider), there is also significant cancellation of $\mathrm{Re}(\alpha^{-1})$ and $\mathrm{Re}(S)$ at nearby wavelengths, and thus the extinction peak profile is relatively broad.

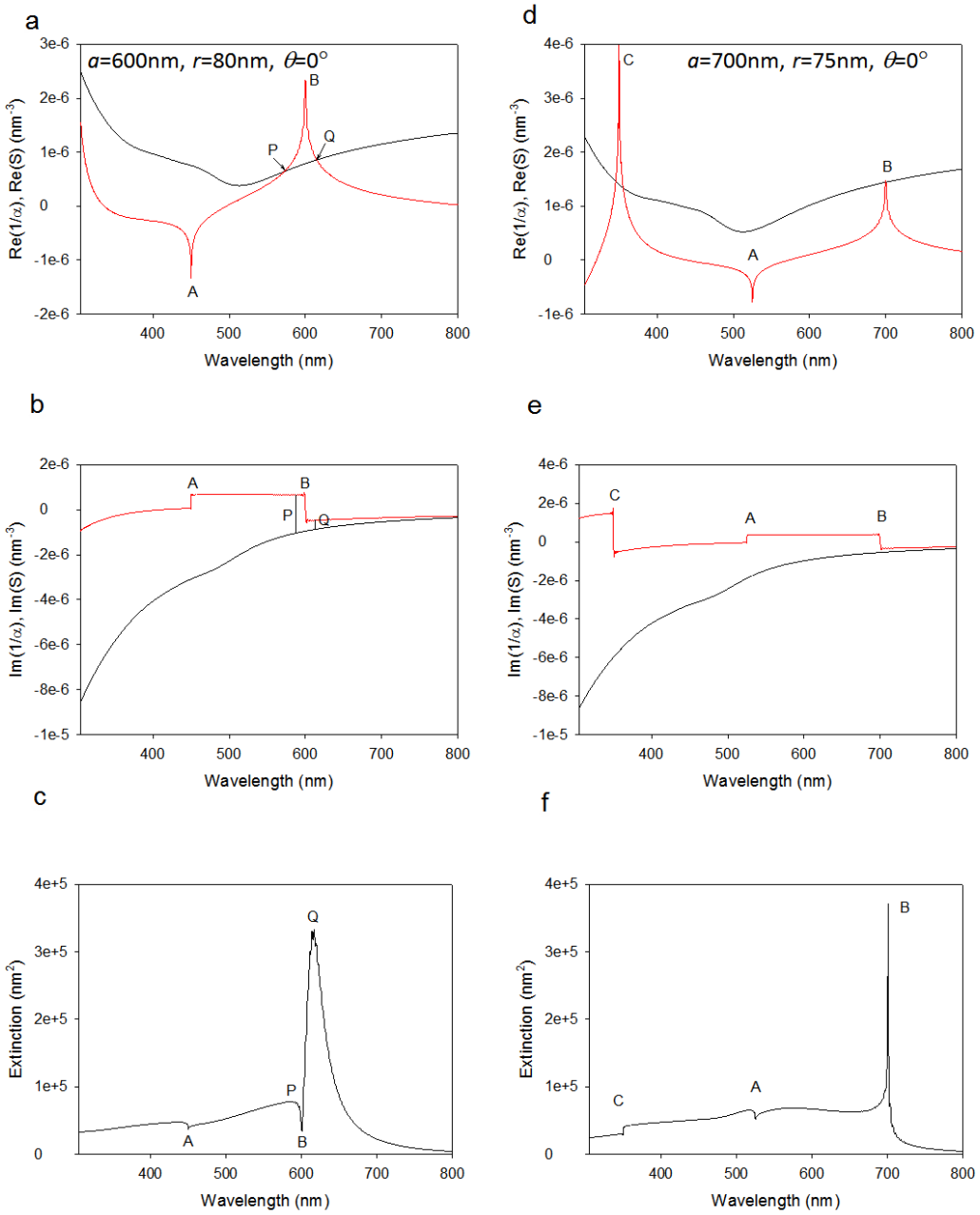

Figure 1.9 – Spectral behaviour of the real and imaginary components of the inverse polarisability α^{-1} (black) and dipole sum S (red) for a square array of gold nanospheres on a glass substrate, and the resulting extinction spectra at normal incidence in air. (a) to (c) (left column) are for period $a = 600$ nm, and radius $r = 80$ nm, and (d) to (f) are for $a = 700$ nm and $r = 75$ nm at normal incidence. Calculated for 100 interacting structures. S is divergent at A and B for infinite arrays, but finite arrays produce broadened peaks that do not diverge.

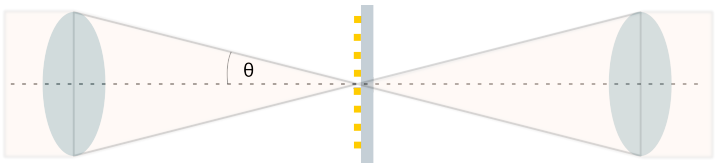

Figure 1.10 – Schematic diagram of a typical transmission measurement setup with focussing optics. All my measurements of transmission and ellipsometry used focussing optics with NA = 0.1.

This is in contrast to the situation depicted in figure 1.9(d-f). Here, Re(α^{-1}) and Re(S) cancel exactly at the Rayleigh wavelength, at point B. Because the intersection occurs at the apex of the sharp peak of Re(S), the completeness of the cancellation of Re(α^{-1}) and Re(S) at neighbouring wavelengths quickly diminishes away from point B. Additionally, Im(α^{-1}) and Im(S) become closer to each other, and to zero, with increased lattice periodicity. This results in strong overall cancellation of α^{-1} and S at the specific wavelength B, and a correspondingly high effective polarisability and sharp peak in extinction, as seen in graph (f).

A further study and application of the coupled dipole approximation at normal incidence can be found in section 2.2, where it was employed to predict optimal parameters for strong resonances at normal incidence.

1.6.1.2 Spatial coherence

In the couple dipole model above, it is assumed that all the dipolar resonators are excited by a collimated beam of light. However, a practical measuring setup often necessitates the use of focussing optics (figure 1.10). In this configuration the excitation field at the sample surface can only be considered coherent over a spatial coherence distance of order λ/θ at excitation wavelength λ, for small θ (θ is depicted in figure 1.10). This effectively reduces the number of nanostructures that participate in the collective resonance, N, to $N \approx \frac{\lambda_R}{\theta a}$, where λ_R is the Rayleigh wavelength at which the collective resonance is excited and a is the sample period. All optical measurements in this thesis used focussing optics of NA = 0.1, which gives $\theta \approx 0.1$ rad in air, and therefore $N \sim 10$ for the main Rayleigh resonance in air.

1.7 Resistive coupling

Another coupling mechanism which has been much less thoroughly studied is resistive coupling of plasmon resonances[53, 54]. This mechanism was first suggested by Kravets *et al.* to explain the quantised transmission of an array of plasmonic nanopillars on a conductive sublayer[53]. It was observed that the transmission through the arrays of gold nanopillars was quantised in the infrared limit into levels separated by $\pi\alpha \approx 2.3\%$. An explanation for the phenomenon was presented, suggesting that the quantised transmission plateaux arise as a consequence of quantised shunt resist-

ance between the nanopillars via the conductive chromium/ titanium sublayer, with a thin non-conductive chromium/ titanium oxide layer providing a tunnel barrier[53]. The tunnel barrier is overcome by dielectric breakdown, induced by the strong plasmonically enhanced electric fields at the surface of the nanopillars, allowing the nanopillars to couple resistively through the conductive sublayer. The contact resistance of a narrow breakdown channel is known to be quantised, thus leading to the quantised transmission observed.

Work presented in chapter 4 of this thesis and published in 2013[54] includes evidence for the resistive coupling of LSPR through a graphene layer transferred atop an array of diffraction coupled gold lines.

1.8 Plasmonic Metals

1.8.1 Silver

Silver is the simplest plasmonic metal to understand, as it is very well modelled by the Drude model (equation 1.17). Its SPP dispersion relation closely resembles the idealised case plotted in figure 1.1. Silver has the highest conductivity of any metal, and no strong inter-band transitions in the visible spectrum. Correspondingly, it also has the least damping for plasmonic applications. However, silver's downside is in its tendency to oxidise, which causes a gradual decay in resonance quality and limits its use for applications in ambient conditions. Recent work in our group however, demonstrated that graphene (see section 1.9) transferred on top of a silver layer can protect the surface from oxidation and preserve its properties for plasmonic applications[55].

1.8.2 Gold

Gold's high conductivity and exceptional inertness are its most advantageous properties. For some applications it is also favoured for its surface chemistry and biocompatibility[8]. However as might be deduced from its colour, gold has an inter-band transition in the visible part of the spectrum, at around 470 nm, and several more in the ultraviolet, such as at 325 nm[8]. These result in increased damping near these wavelengths when compared to silver, increasing the imaginary component of the dielectric function. Accurately modelling the dielectric function of gold near these transitions requires modification of equation 1.17. The presence of these inter-band transitions is the reason that gold is usually used for plasmonic resonances of wavelength > 600 nm. In this region damping is smaller and gold much more closely resembles an ideal Drude metal[8].

1.8.3 Copper

Copper has similar plasmonic properties to gold, and similarly its colour is an indication that it also has inter-band transitions towards the blue end of the visible spectrum. Copper is more conductive than gold, cheaper than gold and silver, and (unlike gold) is CMOS compatible. However, oxidation is again a major issue, with copper surfaces losing their plasmonic characteristics rapidly upon contact with air. As with silver, copper too can be protected from oxidation with a graphene layer to preserve its plasmonic properties. Graphene protected copper even showed a slight improvement in SPP resonance quality factor[55].

1.8.4 Other plasmonic metals

Many other metals support surface plasmon resonances. Aluminium has an inter-band transition at ~800 nm, which severely limits its application in the visible. However its damping is much lower in the blue and UV part of the spectrum[10]. Like copper, it suffers from rapid oxidation, which limits usefulness for plasmonic applications. Other metals with plasmon resonances include alkali metals such as lithium, sodium and potassium (which are obviously severely limited by their reactivity), as well as nickel, indium, platinum, palladium and rhodium[10, 23]. These metals generally suffer from high losses (except potentially the highly reactive alkali metals), and so are only used in situations where they exhibit some other useful property such as catalysis[10]. Alloys present another interesting possibility which has only recently begun to be investigated for plasmonic applications[10, 56, 57].

1.9 Graphene

Graphene is a two-dimensional material made of either one or a few stacked layers of carbon atoms, each layer arranged in a hexagonal lattice. It was first isolated and studied in 2004[58], by repeated cleaving of small pieces of graphite (which can be considered to consist of many thousands of stacked graphene layers) with adhesive tape, until the graphite had been subdivided into single graphene sheets. Monolayer graphene has a number of remarkable properties[59]. It is, of course, the thinnest material possible at only one atom thick. It has the highest electron mobility of any known material, with mobilities in excess of 200,000 $cm^2V^{-1}s^{-1}$at room

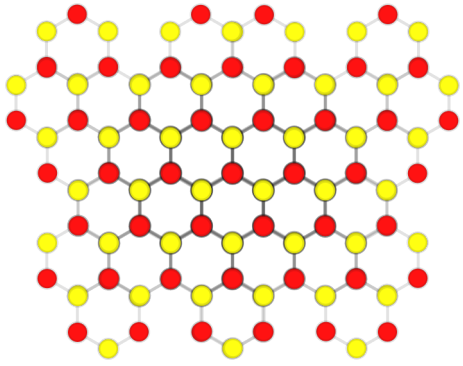

Figure 1.11 – Graphene crystal structure. The graphene hexagonal lattice can be analysed as two intersecting triangular sublattices, A and B (red and yellow).

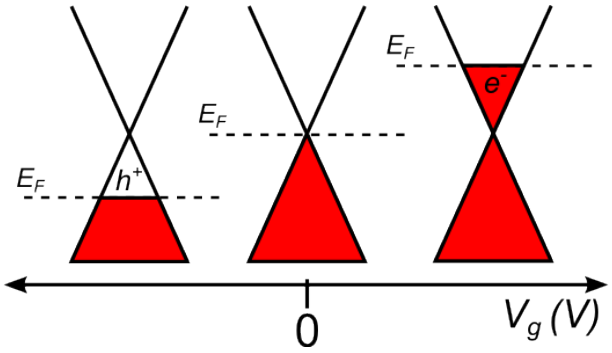

Figure 1.12 – Gating graphene - ambipolar field effect with linear dispersion near the Dirac point.

temperature[60, 61], along with highly unusual electronic properties, discussed below. It is also the strongest material known[62], yet is also flexible, and forms the most impermeable membrane known[63]. These are just a few of the material's remarkable properties, many of which could be appealing for plasmonic applications[64].

Electrons in monolayer graphene obey a linear dispersion relation near zero energy, where two cosine energy bands (one corresponding to each sublattice - figure 1.11) intersect. As the electrons interact with the lattice they behave as quasiparticles with zero rest-mass, which are better described by the relativistic (2+1)-dimensional Dirac equation than the Schrödinger equation, and are often referred to as massless Dirac fermions[59]. While these massless quasiparticles do not travel at the speed of light, they still have a remarkably high Fermi velocity, $v_F \approx 10^6\,\mathrm{ms}^{-1} \approx c/300$[59] and travel for micrometres without scattering even at ambient temperature[61, 65].

Graphene can support intrinsic surface plasmons at infrared and terahertz frequencies [64, 66]. Doping or gating a graphene layer can raise its Fermi level which increases the number of free charge carriers available to support plasmon resonances. Additionally, the electrons occupying states in the conduction band prevent inter-band transitions via Pauli blocking. A high-frequency limit of surface plasmons in graphene is therefore imposed by the level to which the material can be doped, because as soon as the plasmon energy approaches the minimum energy needed for an inter-band transition that is not prevented by Pauli blocking ($2E_F$ in figure 1.12), losses rapidly damp the resonance. This limit lies somewhere around 1 eV[64], which corresponds to 242 THz or 1.2 μm for a free-space photon. Because the charge carrier concentration can be varied linearly with gate voltage, the behaviour of graphene plasmons can be modified[66], allowing manipulation of optical properties.

While graphene's quantum efficiency for light-matter interaction is extremely high[64], its absorption is only 2.3% for a monolayer because the material is so thin (a value defined by $\pi\alpha$, where α is the fine structure constant[67]). This is remarkably high for an atomic monolayer, but is lower than might be desired for many applications, and does not compare favourably with metallic structures, which can absorb nearly 100% of light with large bandwidth range if fabricated with appropriate geometry[68].

This has led to the development of hybrid devices, combining graphene and metal plasmonics. Among the early studies of plasmon enhanced graphene-light interaction were measurements of surface enhanced Raman scattering from graphene layers transferred atop arrays of plasmonic nanostructures[69]. Raman enhancement factors of around 1000 have since been reported[70, 71]. Graphene could be an ideal test probe for quantifying Raman enhancement, as its Raman spectrum is reproducible and well known, and it does not suffer many of the disadvantages of dye based approaches (such as irreproducibility, inhomogeneous spatial distribution of dye molecules and photobleaching, section 1.10.1.3). Arrays of plasmonic nanostructures have also been used to enhance photovoltage generation in graphene[72, 73], with a twenty-fold improvement in efficiency reported. Graphene can also be used to modify the properties of resonances in metallic nanostructures[74, 75, 76, 77], in some cases allowing active control via gating[75], and can also be used for reasons not relating to its optical, electronic or plasmonic properties, for example as an easily functionalisable, or oxidation preventing coating[55, 78, 79].

1.10 Experimental techniques

1.10.1 Fluorescence and Raman scattering and spectroscopy

Fluorescence and Raman scattering are two similar but distinct phenomena by which a photon incident on a molecule or crystal can transfer energy to its vibrational modes. Typically, the incident photon loses energy to the vibrational modes, and the emitted/scattered photon will be red-shifted. The difference in frequency is called the "Stoke's shift". If the photon gains energy, we say it has been "anti-Stoke's" shifted. Anti-Stoke's Raman scattering can be used to study the thermal properties of a sample, but is not of much relevance to this work. Molecules and non-infinite crystals exist in discrete allowed energy states. Electronic energy levels are typically separated by several eV, whereas vibrational states are separated by meV. Thus we can view the vibrational states as creating substructure within the electronic states[8]. Figure 1.13 illustrates the difference between Raman scattering and fluorescence in this picture.

1.10.1.1 Fluorescence

Fluorescence is the absorption of one frequency of electromagnetic radiation by a substance, and subsequent emission of radiation of a second lower (for one photon processes) frequency. At a microscopic scale, if an electron is in an electronic state of energy E_0, it can be excited to a higher energy state E_1 by absorption of an incident photon of energy E_i, provided that the energy of the photon is equal to or larger than the difference in energy of the two states ($E_i \geq E_1 - E_0$). If the photon energy is greater than that required for the transition, the excess of energy can be coupled to the vibrational states of the molecule or crystal. Transitions between these vibra-

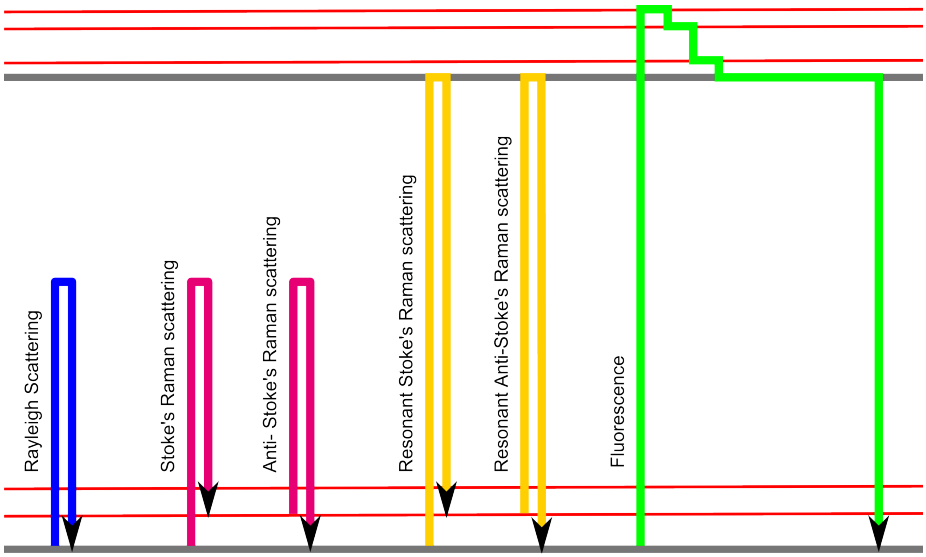

Figure 1.13 – Graphical depiction of the difference between Rayleigh and Raman scattering and Fluorescence. The y-axis represents energy, with electronic states in grey and vibrational states in red. The x-axis gives a rough indication of relative timescales. Adapted from[80].

tional states happen on picosecond timescales, whereas spontaneous emission rates between electronic states tend to occur on nanosecond timescales. Therefore by the time the electron decays back to its ground-state it will typically have reached the bottom of the sub-spectrum of vibrational states and have dissipated energy to phonons in the process. The radiative transition back to the ground-state is therefore of a smaller energy difference than that of excitation and so the emitted photon is of lower frequency. The difference in frequencies is known as the Stoke's-shift. Not all absorbed photons will result in fluorescence. Non radiative transitions such as multi-phonon processes can sometimes return an electron to its ground-state without any light emission. The quantum yield of a fluorophore is the ratio of photons absorbed to those emitted as fluorescence.

1.10.1.2 Raman scattering

Raman scattering is the inelastic scattering of light. Fluorescence is not classed as scattering, as it involves absorption and re-emission, while Raman scattering is instantaneous in the classical picture. In the quantum mechanical picture, the molecule can be considered to be excited momentarily to a virtual state, before instantly decaying. For Stoke's Raman scattering, the molecule will end up in a higher vibrational state (from which it will also rapidly decay) than it's initial state (usually the electronic ground-state), whereas for anti-Stoke's Raman the molecule transitions to a lower vibrational state than its initial state. Raman shifts are usually quoted as wavenumbers, in units of inverse centimetres relative to the excitation laser wavelength (rel. cm^{-1}).

The spectrum of the Stoke's shifted light from fluorescence and Raman scattering is directly linked to the vibrational modes, and thus the chemical structure of the sample under study. Typically, photons re-emitted by fluorescent processes will have undergone a multitude of transitions between vibrational states with each photon taking a different pathway. This results in a convoluted spectrum, making it hard to isolate the effect of individual vibrational modes. Each Raman scattered photon will typically have only interacted with a single mode, making it much easier to link them to the chemical structure of the sample, as the spectrum will consist of more discrete, sharper peaks. The energy lost or gained by each scattered photon is exactly equal to the energy of a vibrational mode in the sample, thus the wavenumbers of the Raman shifts in rel.cm^{-1} correspond directly to the energies of the vibrational modes.

1.10.1.3 Photobleaching

Photobleaching is a common experimental issue, as it causes molecules to temporarily or permanently lose their ability to fluoresce or Raman scatter. Electrons (spin 1/2) in atoms in their ground-state are paired, with opposing spins in a singlet state (total spin 0) due to Pauli-exclusion. Fluorescence and Raman involve transitions between these states and excited singlet electron states. However, there also exist three possible triplet (total spin 1) states where the spin of one electron flips to be parallel to the other. Transitions between singlet and triplet states are forbidden in simple formulations of quantum mechanics, but in practice spin-orbit and vibrational coupling do allow them to occur, but with very small amplitude. If such a transition occurs, the electron becomes inaccessible to the fluorescence and Raman processes, as transition back to the ground-state is now forbidden. Eventually, on much longer timescales than those of fluorescence and Raman, the electron may return to the ground-state via a similar transition. If light is emitted this is known as phosphorescence. The dye will then regain its fluorescence and Raman scattering. Another possibility is that the dye may undergo chemical reaction while in the higher-energy triplet state and permanently lose its fluorescence and Raman scattering. This is a particular risk with oxygen, which is unusual as it has a triplet state as its ground state. This actually reduces its reactivity with most everyday chemicals significantly, but makes it very reactive with other chemicals in triplet states.

1.10.2 Ellipsometry

Ellipsometry is an optical technique that uses polarised light to study the optical properties of a sample. Fundamentally, the ellipsometer measures the ratio between the complex Fresnel reflection coefficients R_p and R_s for $p-$ and $s-$polarised light respectively. These are more typically quoted as Ψ and Δ, where

$$\tan(\Psi)e^{i\Delta} = \frac{R_p}{R_s} \tag{1.29}$$

i.e. Ψ relates to the ratio of amplitudes, and Δ is the phase difference. Since ellipsometry measures the ratio of the two reflection coefficients, it is insensitive to random noise sources and is therefore a very sensitive technique.

In the right circumstances, and in some cases with the help of an appropriate theoretical model of the material, ellipsometry can be applied to determine properties including optical constants (n and k, ϵ' and ϵ''), film thickness (with sub-nanometre precision), doping concentration and surface roughness[81]. The ellipsometer employed in this work, (T.A. Woollam Co. Inc. M-2000F) allows collection of optical spectra in the ultraviolet, visible and near infra-red from 270-1700 nm, at variable angles of incidence from 45-90°. In the order that the components are encountered by the light beam, the ellipsometer apparatus consists of a Xenon lamp light source, a polariser, a rotating compensator, the sample under study, a polarisation analyser and a detector. In my work the ellipsometer was used to measure film thickness and complex refractive indices for calibration of deposition techniques, and most commonly to identify the spectral position and shape of plasmon resonances of my samples.

The ellipsometer was also used to measure transmission spectra. Transmission spectra of plasmonic arrays presented were all normalised to transmission through the plain glass substrate.

1.10.3 Electron beam lithography

Every stage of my work has made use of samples fabricated by electron beam lithography. The fundamentals of the technique are simple and the steps are illustrated in figure 1.14. Referring to the figure, I will describe the typical fabrication process I have used for making gold plasmonic nanostructures. It is possible to vary certain aspects of the process described below, such as using different formula resists, spin-speeds, baking times and developing solution. However my fabrication procedure was consistent throughout my work, and was as described below unless otherwise specified:

1. First a substrate is prepared. Since I have been making samples to study their optical properties, I have used glass slides. Silicon wafer (often with an oxide coating) is a common choice of substrate for electron beam lithography, but does not allow measurement of optical transmission.

2. Because glass is not conductive, a thin (typically 3 - 5 nm) layer of chromium is evaporated, to prevent static charge build-up on the surface when it is exposed to the electron beam. This is not necessary if silicon and silicon dioxide is used.

3. Poly(methyl methacrylate) (PMMA) resist is spin coated onto the sample. PMMA is a common polymer, generally known under the trademarks Perspex, Plexiglas or Lucite. For this application, PMMA of very specific molecular weight is dissolved in an anisole solvent, and spin coated with precise thickness. For almost all my samples, the PMMA was coated in two layers, the first using PMMA with

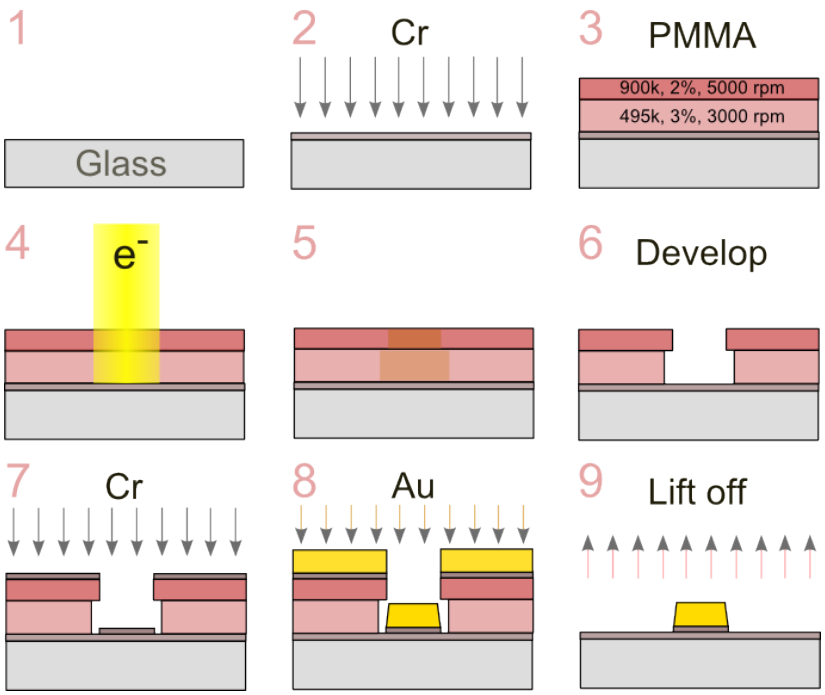

Figure 1.14 – An illustrated guide to electron beam lithography on glass.

molecular weight 495k, in a 3% solution (by mass) in anisole, coated at a spin-speed of 3000 rpm, and the second using molecular weight 950k, 2%, at 5000 rpm. Each layer is baked for 15 minutes after spin-coating.

4. A beam of electrons is then used to draw the desired pattern onto the PMMA layers on the surface of the sample.

5. Areas exposed to the electron beam undergo a change in their chemical composition, which increases their solubility in a developer solution. The lower molecular weight PMMA is more strongly affected than the layer of higher molecular weight.

6. The PMMA is exposed to a developing solution (1:3 MIBK:IPA) for 30s, which dissolves only the areas of resist which were exposed to the electron beam. The 495k layer dissolves more readily than the 950k layer, resulting in a slight overhang. We now have a mould with gaps in the areas that were exposed to the electron beam.

7. A chromium adhesion layer is deposited prior to gold deposition. Gold alone does not adhere well to glass or the now-oxidised chromium layer that was put down to prevent charging.

8. Gold is deposited by electron beam evaporation, coating the PMMA layer and filling the holes in the PMMA mould. The overhang created by the bilayer resist prevents the formation of 'bunny ears' - spikes at the edge of the deposited gold

structures caused by gold build up against the edges of the resist mould, instead of deposition onto only the substrate beneath.

9. The sample is then immersed in acetone, which rapidly dissolves all the PMMA, leaving the unwanted gold and chromium detached from the sample surface to lift off into the acetone. All that then remains on the sample surface is the gold and chromium deposited onto the surface, in the areas patterned with the electron beam.

Unless otherwise specified, this is the fabrication process that was used for all samples fabricated in the coming experimental sections. All electron beam lithography was carried out with the assistance of Gregory H. Auton (chapters 2 and 3) or Fred Schedin (chapters 4 and 5).

My Work

Chapter 2

Collective Plasmon Resonances at Normal Incidence

Benjamin D. Thackray, Vasyl G. Kravets, Fred Schedin, Gregory H. Auton, Philip A. Thomas and Alexander N. Grigorenko

We fabricated gold plasmonic nanoarrays on a glass substrate supporting narrow collective resonances that can be excited with light at normal incidence in an asymmetric air or water environment. Resonance quality factors up to 19 in air, 45 in water and 85 in glycerol were measured at normal incidence, and a very high figure of merit for bio-sensing applications in water was achieved. The coupled dipole approximation was used to predict the optimum combinations of nanostructure size and periodicity. These results could facilitate highly sensitive techniques for bio-sensing with with the spatial resolution, flexibility and miniaturisation potential of LSPR based approaches. (This work was published in *ACS Photonics* in 2014[82])

My Contribution

I designed, fabricated and measured the samples, with the help of Fred Schedin and Gregory H. Auton for electron beam lithography, and the assistance of Vasyl G. Kravets and Philip A. Thomas for measurements. Initial theoretical studies and simulation were performed by Alexander N. Grigorenko. I extended the theoretical study to produce the plots in figure 2.6.

2.1 Introduction

Surface plasmon resonance (SPR) based sensors typically use the Kretschmann configuration to excite propagating surface plasmon polaritons at the interface between a thin metal film and dielectric medium, such as air or water (section 1.3). The technique exploits the fact that the spectral (or angular) position of the surface plasmon

resonance minimum is strongly dependent upon the refractive index of the dielectric medium within the first few hundred nanometres from the surface of the gold layer. If the gold surface is functionalised with a molecule that binds to an analyte of interest, then the presence of the analyte and its real-time binding characteristics can be deduced by monitoring the shift of the surface plasmon resonance produced by local refractive index changes near the gold surface. The technique is fast, label-free and highly sensitive, capable of detecting refractive index shifts as small as $10^{-5}-10^{-6}$ RIU with intensity based measurements[83]. For example, both proteins[84], such as insulin[85], and DNA[86] can be detected at nanomolar (nM) concentrations.

The first application of this configuration for bio-sensing was by Liedberg *et al.* in 1983[87, 88], after which the technique rapidly developed to become a major application of plasmonics. Today commercial SPR devices are offered by several companies[89, 90], and significant advances have been made in approaches to surface functionalisation, utilising the sensing volume above the surface with functionalised dextran hydrogel[91], combining the technique with microfluidics, and schemes for multi-analyte detection[92]. However, devices based on the Kretschmann configuration have a number of disadvantages. A high quality gold film, steep angle of incidence (AOI) and a prism are required to enable light to couple to the higher-momentum SPR modes, and as a result, the apparatus is bulky and consumables for SPR based detection can be expensive[90, 93]. Significantly, the sensing area when using SPR is not well localised on the sample surface. Typically it is of the order of the SPR propagation length in-plane; i.e. few to hundreds of micrometers, but can even be much larger[94]. The sensing volume also extends hundreds of nanometres from the gold surface. If the purpose is to sense bulk refractive index then this is beneficial, providing at least an order of magnitude increase in sensitivity compared to LSPR, but for bio-sensing applications it is usually disadvantageous to have such a large sensing volume[94]. Most high-end SPR set-ups are bulky and unsuitable for imaging and point of care and 'lab on a chip' applications[94]. It would be helpful if light could be strongly coupled to plasmon resonances at normal incidence, so detection could be performed in a standard microscope without the need for specialist optics, making the technique much more accessible. Even if detection sensitivity is reduced, increased accessibility could open up the technology for applications where extreme sensitivity is unnecessary[93].

Localised surface plasmon resonances (LSPR) in sub-wavelength metallic nanostructures (section 1.4) provide a solution to some of SPR's limitations for bio-sensing applications[94, 95]. LSPR based detection can usually be performed at normal incidence, and can provide nanometre-scale localisation, allowing detection up to the single (protein) molecule limit[94]. Additionally, the LSPR wavelength can be tuned from the visible and into the infrared by variation of the nanostructure geometry. LSPR can also be combined with other complementary sensing techniques, such as

surface enhanced Raman and fluorescence spectroscopy. LSPR resonances in simple isolated structures tend to be spectrally broad and of low quality factor, but very high detection sensitivities have been achieved with novel structures. For example, neurotoxins linked to Alzheimer's disease have been detected at ~100 fM concentrations on a substrate made with nanosphere lithography[95, 96]. Overall, LSPR could be much more suitable for many bio-sensing applications due to its higher spatial localisation, miniaturisation potential and widely tunable resonance characteristics[94, 97]. Phase-based measurements present potential for a further 1-2 orders of magnitude improvement in refractive index sensitivity, in both SPR and LSPR configurations[83, 98, 99]. While SPR approaches can appear to out-perform LSPR approaches 'on paper', i.e. when judged in terms of sensitivities and figures of merit (section 2.5), the spatial specificity and resolution of LSPR approaches means that they often prove more sensitive in a real bio-sensing setup[100].

Collective resonances (section 1.6.1) in arrays of plasmonic nanostructures, where diffraction is used to reinforce the LSPR resonances in the individual nanostructures of the array, can be very narrow and of high quality factor and improve the refractive index sensitivity of LSPR resonances until almost comparable to SPR[83]. This makes them ideally suited for bio-sensing applications. Phase-based approaches exploiting this effect can achieve sensitivities up to the 10^{-10} RIU[83], or fg/mm^2 level[79]. These diffraction coupled resonances are typically only excited at a steep AOI around ~60°[51], although in arrays of tall nanostructures, narrow resonances in a symmetric environment have been attained at shallower angles, such as 15°[101]. These results were attributed to the out-of-plane coupling of the localised surface plasmon resonances of the individual nanostructures, facilitated by the tall nanostructures. Diffraction coupled resonances at normal incidence have been predicted and measured[52] in arrays of gold nanospheres, but strong resonances are typically only observed in an index-matched environment. Auguié *et al.* explain in a theoretical study of the dipolar model how an asymmetric environment can suppress the collective resonance modes in arrays, especially in the case of structures small compared to their period[102]. They go on to predict that this could be overcome with larger or asymmetric nanostructures (a prediction we confirm). Excitation of collective resonances in arrays at normal incidence has been presented from a water/ glass asymmetric environment, and even air/ glass[103, 104], however to our knowledge, the resonances presented here are of the highest quality factor attained in a similar configuration to date.

Presented in this chapter are gold nanostructure arrays which have high quality factor resonances at normal incidence in air, water and glycerol and novel resonance modes in asymmetric, out-of-plane L-shaped nanostructures that were also observed. We have measured near infra-red resonance quality factors as high as 19 in air (spectral position 843 nm), 45 in water (1025 nm) and 85 in glycerol (1228 nm). The

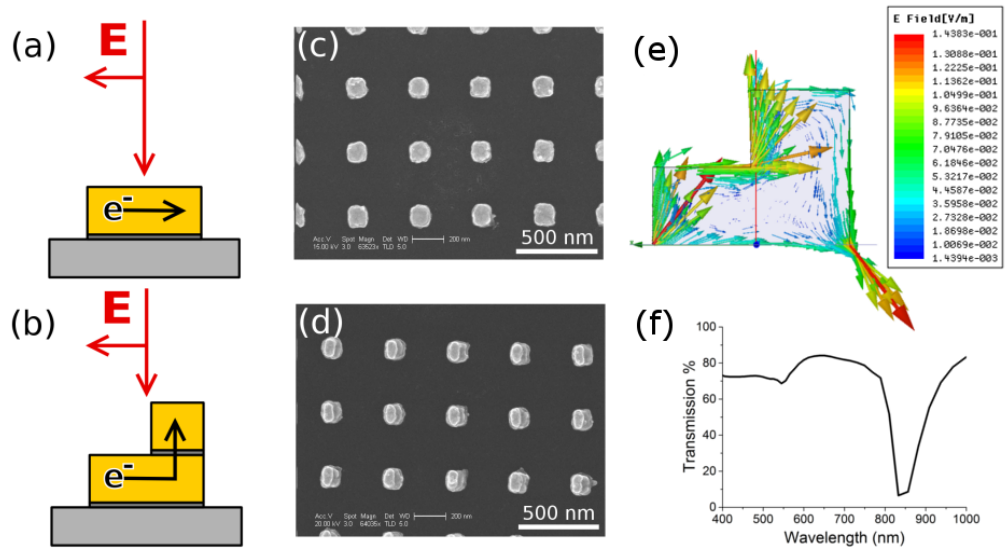

Figure 2.1 – Cross-sectional side view of nanostructures, SEM images and FDTD simulation (a) Cross-sectional diagram of a square nanostructure fabricated with one lithography step. (b) Cross-sectional diagram of an L-shaped nanostructure fabricated with two lithography steps (c) SEM image of an array of square structures with period 400 nm (d) SEM image of an array of L-shaped structures with period 400 nm (e) FDTD simulation of 150 nm L-shapes in an array of period 544 nm (f) Predicted transmission spectrum from the FDTD simulation.

LSPR of similar nanoparticles when the collective mode was not excited had quality $Q = 9$ in air in the red part of spectrum. The diffraction coupled resonances in our structures are spectrally narrower and of higher quality factor, and register a higher figure of merit (FOM*[105]) for bio-sensing applications than any previously presented in similar structures, to our knowledge.

2.2 Investigation and experimental results

To achieve collective resonances at normal incidence, one needs to use either composite or large nanostructures as an array elementary cell. Composite nanostructures show strong near-field coupling inside the nanostructure[106, 107] that alleviates restrictions imposed on the plasmon resonance of a simple sphere, while large nanostructures demonstrate the small absorption necessary for existence of the normal angle resonance.

We initially studied composite nanostructures for normal angle collective resonances, fabricating the 'L'-shaped structures shown in figure 2.1(b,d). Our reasoning was as follows: normal incident light will excite in-plane electron resonance in the base of the L-shaped structure, which is electrically connected to the out-of-plane stem of the L-shaped structure. The in-plane electron oscillation induced in the base by the incident light should then drive out-of-plane electron oscillation in the stem, coupling the normally incident light to the collective out-of-plane modes of the array.

Figure 2.1 illustrates the principle behind the design. FDTD simulation predictions supported our expectations, as shown in figure 2.1(e,f).

The structures were fabricated from gold on a glass substrate by electron-beam lithography (see section 1.10.3 and 2.3). The first arrays were 200 µm x 200 µm overall, with periods 400 nm and 500 nm. 130 nm x 130 nm, 80 nm tall square nanostructures were fabricated in the first lithographic step, then a second lithographic step added the second layer of 130 nm x 60 nm, 60 nm tall gold to the top of each structure to complete the out-of-plane L-shapes (e.g.. figure 2.1(d)).

Each array of squares was created with a duplicate control array in the first lithographic step, which was left untouched by the second lithography. A 3 nm chromium adhesion layer was first evaporated beneath each layer of gold deposited, as well as over the entire glass substrate to prevent charging during electron beam lithography. The chromium layer was later etched from the glass substrate, as at normal incidence the metallic sublayer can effectively suppress plasmonic resonance due to resistive coupling (section 1.7). The resulting structures can be seen in the SEM images in figure 2.1: 2.1(c) shows an array of simple squares, and 2.1(d) shows an array of out-of-plane L-shapes.

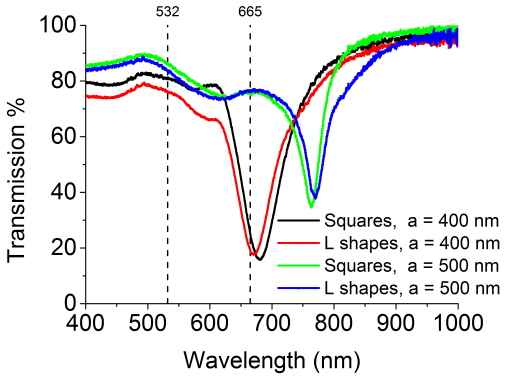

Figure 2.2 – Transmission at normal incidence for 400 and 500 nm period arrays of square and L-shaped nanostructures in water. Vertical lines indicate the position of the Rayleigh anomalies at normal light incidence.

At normal incidence, transmission spectra measured on the arrays of L-shaped structures failed to exhibit any significant improvement on the control samples in air or water (figure 2.2). However, ellipsometry (section 1.10.2) (figure 2.3) demonstrated some significant differences. Both squares and L-shapes demonstrate the familiar[51] diffraction coupled resonance at a high angle of incidence (60-65°). At the same time, the L-shaped structures demonstrate a significantly stronger resonance than the squares at shallower angles of incidence (45-55°). Transmission results at an angle (figure 2.4) also show a distinction between the L-shapes and squares. For small (5-25°) angles of incidence, the two structures behave similarly. However, at higher angles of incidence the resonance quality decreases significantly for the square structures, while the L-shapes retain the quality of their resonances up to 40°, above which they also decrease in strength, until 55-60° where the transmission minimum becomes deeper again. Both structures show a similar blue-shift of approximately 20-25 nm of the resonance position as the angle increases from 5-60°, with a stronger blue-shift at smaller angles of incidence.

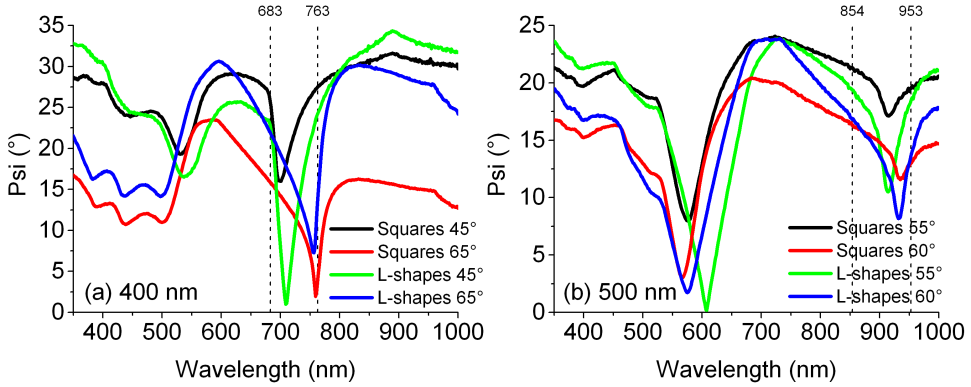

Figure 2.3 – Ellipsometry of square and L-shaped nanostructure arrays. (a) Array period 400 nm. (b) Array period 500 nm. While the behaviour of both structures is similar for the well documented diffraction coupled resonance excited at around 60°[51], the behaviour of squares and L-shapes differs significantly at shallower angles, with the L-shapes exhibiting a second resonance at 45° when a = 400 nm and at 55° when a = 500 nm (green lines). Vertical lines indicate the position of the air Rayleigh anomalies.

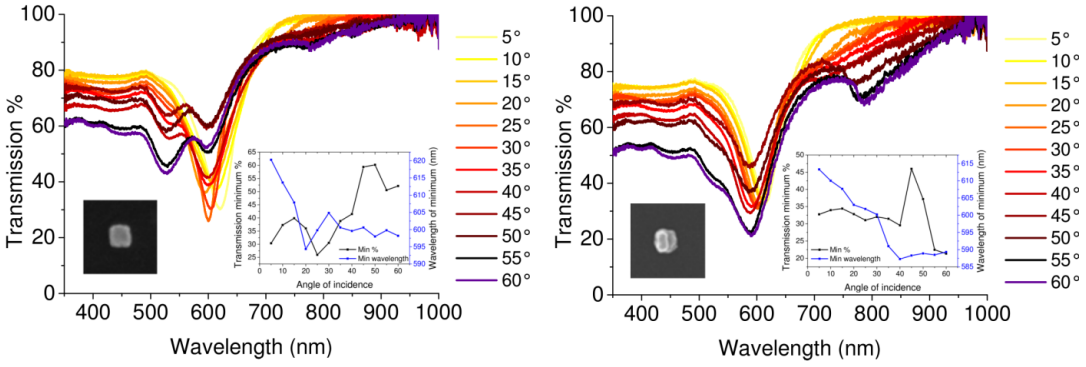

Figure 2.4 – Transmission for angles of incidence from 5° - 60° (a) for square nanostructures with period 400 nm (b) for L-shaped nanostructures with period 400 nm. Insets show an SEM image of a typical nanostructure, and plot the depth and spectral position of the local minimum at ~600 nm. While the squares have a sharper minimum, the transmission minimum remains deep at higher angles for the L-structures. Both structures exhibit a similar blue-shift of the resonance wavelength with increasing angle.

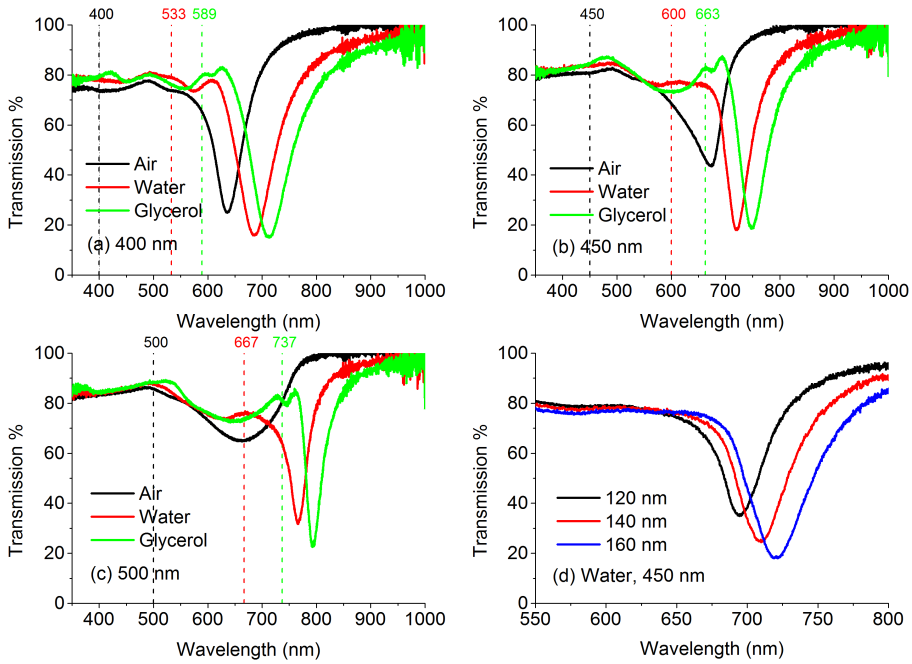

Figure 2.5 – Transmission from arrays of square nanostructures in air, water and glycerol. (a) Transmission of an array with period 400 nm (b) Transmission of an array with period 450 nm (c) Transmission of an array with period 500 nm. (d) Close-up of minimum transmission from arrays with nanostructures of different sizes with period 450 nm in water. Vertical lines indicate the calculated position of the Rayleigh anomaly at normal incidence.

Unfortunately, the novel resonances in the L-shaped structures were excited too far from normal incidence for our intended bio-sensing application. At normal incidence, the L-shapes provide no improvement on simple square structures which suggests that coupling to the out-of-plane mode is difficult to achieve under normal illumination. More positively, the resonances in the arrays of square structures were surprisingly good, especially considering the adverse effect that asymmetric environments can have on resonances at normal incidence[102]. The reason for the limited success of the L-shaped structures lies in strong absorption observed in a unit cell of the structure. We found that larger nanostructures (which show smaller absorption and larger scattering) were more suitable for excitation of normal angle collective resonances.

Building on these results, we decided to optimize the diffractive coupled resonance observed in regular arrays of simple square nanostructures. We fabricated a set of arrays with a larger variety of periods and square sizes using the same fabrication procedure as for the previous structures, but without a second lithography step. The square height was 80 nm, and again the chromium layer was etched from the substrate after fabrication and SEM imaging. From the variety of square sizes on this sample (120 nm, 140 nm, 160 nm) we have presented just the results from squares 160 nm in size, which showed the best resonances overall (figure 2.5(d) shows the effect of the square size on the resonances of an array with period 450 nm – confirming of the

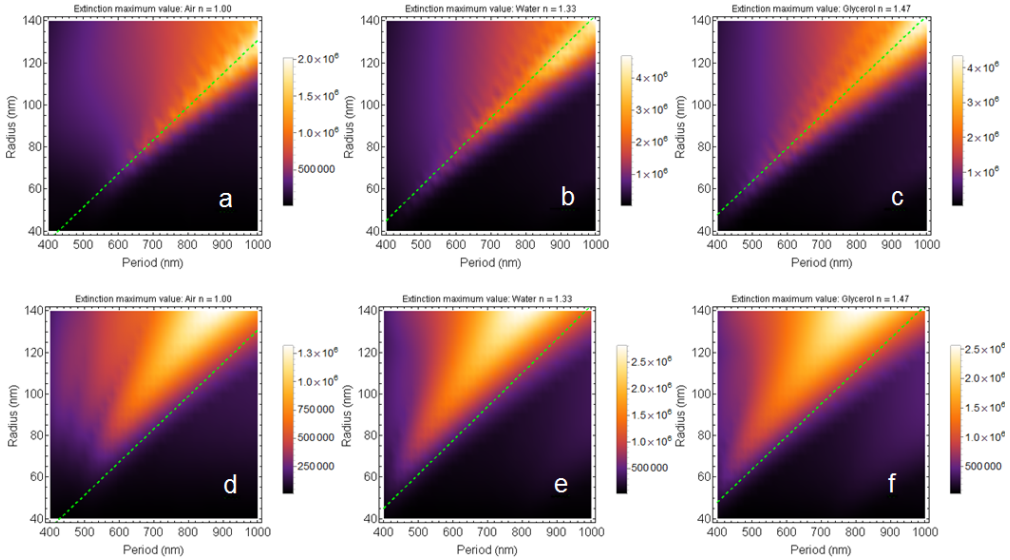

Figure 2.6 – Simulation of the extinction maximum values produced by various combinations of the array period and nanostructure size (spherical nanostructures assumed). (a)-(c) show the prediction of the model for 100 interacting nanoparticles, in air, water, and glycerol respectively. The green dotted line provides an indication of the optimal combination of structure size and array period. It is clear that a larger than optimal ratio of size to period is predicted to perform better than a smaller than optimal ratio. (d)-(f) are predictions for 10 particles in air, 13 particles in water and 15 particles in glycerol, respectively. Here the number of particles has been reduced to an effective value to account for the effects of spatial decoherence (section 1.6.1.2). The positions of the green lines are unchanged, indicating a shift of the optimum ratio towards larger particles, and a broadening of the distribution.

importance of the nanostructure size[102]). Figure 2.5 displays selected transmission results from the new samples in air, water, and glycerol. Good resonances exist in glycerol (expected, as the environment is symmetric), but more unusually also in water and air (especially for the sample with 400 nm period).

To further improve our normal incidence resonances we turned to the coupled dipole model (section 1.6.1.1) and attempted to use it as an approximate theoretical model to predict optimal combinations of array period and nanostructure size. Figure 2.6 (a)-(c) shows the predicted maximum extinction (per particle) in air water and glycerol environments, as a function of nanostructure (assumed spherical) radius and period (100 nanostructures simulated, we later considered the effect of spatial coherence when using focussing optics in (d)-(f)). It is clear that optimal combinations lie on or close to the dotted lines indicated. The lines could be approximately fitted to give equations for optimal radius of nanostructure $r = a/6.30 - 28$ in air, $r = a/6.15 - 20$ in water and $r = a/6.35 - 15$ in glycerol, where a is array period. These results also suggest that nanostructures that are slightly larger than optimal for a given period perform better when using focusing optics than those that are slightly smaller.

From this, we designed and made square nanoarrays (methods as before) with larger nanostructures, dimensions around 200 nm x 200 nm (in-plane) x 100 nm (out-

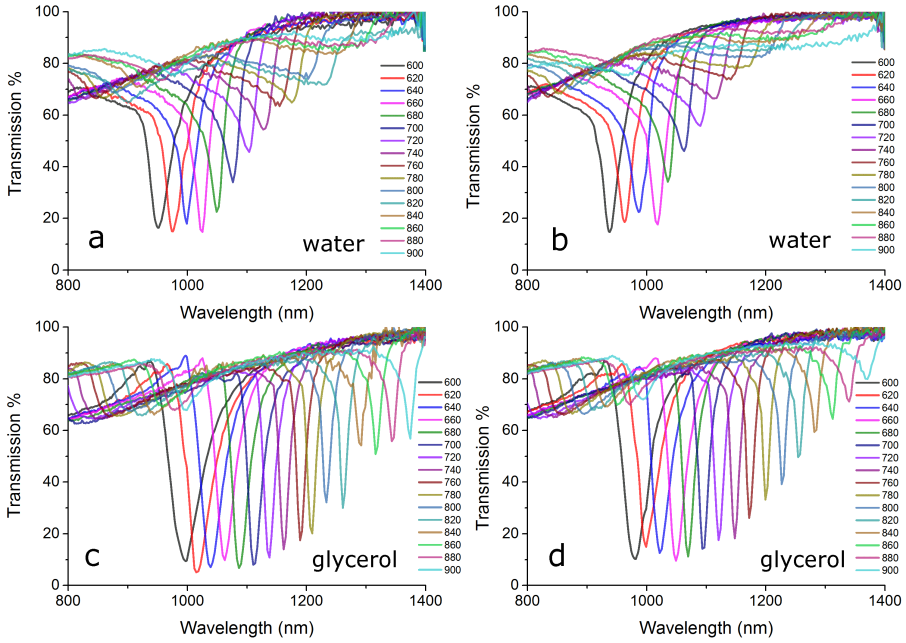

Figure 2.7 – Transmission of arrays of larger, 100 nm tall, square nanostructures with periods from 600 to 900 nm. (a) Structures 210 nm square in water (b) structures 195 nm square in water (c) structures 210 nm square in glycerol (d) structures 195 nm square in glycerol. Clearly there are many samples with high quality factor resonances.

of-plane), with periods from 600 to 900 nm, in steps of 20 nm. The results from these samples were disappointing in air, showing no good resonances (not presented), but well-behaved in water and glycerol (figure 2.7), demonstrating the expected high quality factor resonances at normal light incidence (Q up to approximately 45 in water, 85 in glycerol), which worsen as the period increases and the nanostructures become relatively too small.

At this point we had very good results for collective resonances at normal angle of incidence in water and glycerol, but we still wanted to improve the resonances in air. Theory and the experimental results of Zhou and Odom in an index matched environment[101] suggest that the height of the unit cell nanostructure, not just overall volume, may be especially important for supporting resonances at normal light incidence. While we had made the nanostructures larger, they were still only 100 nm tall and a poor approximation of the spheres for which we have calculated our theoretical predictions. To this end, we fabricated arrays of nano-cubes with sizes around 200 nm x 200 nm (in-plane) and height 200 nm (out-of-plane). The experimental results for these structures are shown in figure 2.8. The collective resonances observed at normal light incidence for these taller structures followed theoretical predictions and showed resonances with high quality factors up to 19 in air.

It is important to note that transmission spectra were measured with focussing optics; using lenses of numerical aperture 0.1. The presence of the focussing op-

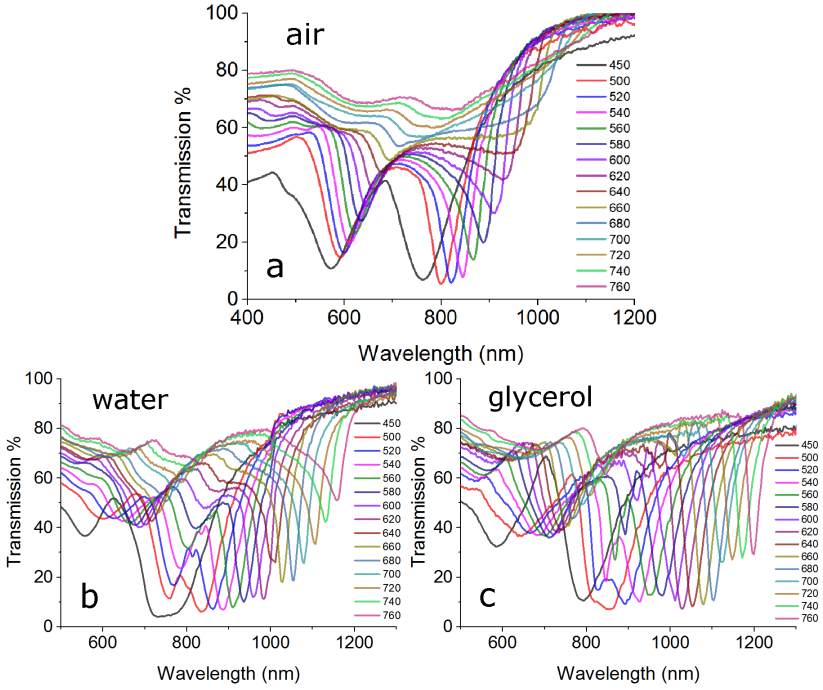

Figure 2.8 – Transmission of arrays of even larger, 200 nm tall, square nanostructures, with periods varying from 450 to 760 nm. Data presented is from structures 200 x 200 x 200 nm in size. (a) in air (b) in water and (c) in glycerol.

tics was a practical necessity, because of the restrictions on sample array size from the electron beam fabrication time involved. The higher numerical aperture implies lower degree of spatial coherence (section 1.6.1.2) which in turn reduces the resonance quality factor (due to reduction of a number of nanostructures which vibrate in phase and hence are effectively involved in the production of diffracted orders). Resonance quality factors would be expected to be even higher in the case of collimated illumination. The effect of the focussing optics on the optimum resonance conditions can be seen in figure 2.6 (d)-(f). Since we present these results with their practical application in mind, the presence of focussing optics is a realistic representation of the optical setup that would be used in a bio-sensing application, and thus appropriate.

2.3 Fabrication details

Samples were fabricated by electron beam lithography, as described in section 1.10.3. First, a 1.2 mm thick glass substrate was coated with 3 nm of chromium to prevent charging. All except the 200 nm tall structures were made as described in section 1.10.3; using bilayer PMMA resist (495k, 2%, 3000 rpm then 950k, 3%, 5000 rpm). For the 200 nm tall structures, the first layer was duplicated, to increase the resist thickness to accommodate the taller nanostructures.

In an additional step to the method described in section 1.10.3, the chromium layer was chemically etched from the surface of the sample after all other processing.

This removed the chromium in all the areas not protected by gold (it will remain as an adhesion layer underneath the gold structures, where it is protected from the etchant in which it was immersed for only the minimum amount of time required to remove it from the exposed areas of the sample surface).

2.4 Highest quality factors

In summary, our highest approximate quality factors (Q = λ / FWHM) measured in each environment are 19 in air (n = 1.00, λ = 843 nm, period a = 540 nm, structures 200 x 200 x 200 nm), 45 in water (n = 1.31, λ = 1025 nm, a = 660 nm, structures 195 x 195 x 100 nm), and 85 in glycerol (n = 1.44, λ = 1228 nm, a = 800 nm, structures 200 x 200 x 100 nm).

2.5 Figures of merit

It is common to calculate a figure of merit (FOM) to quantify the sensing potential of plasmon resonances[108, 109]. One is typically defined as the change in a measured quantity (such as the wavelength of the resonance minimum) per refractive index unit (this quantity is termed the 'sensitivity', S), and is usually normalised to give the FOM by dividing by the FWHM of the resonance dip (a sharper peak gives a more precise indication of the resonance minimum position). This FOM adequately quantifies the sensing potential of plasmonic modes in configurations similar to those used in commercial instruments, where the angular shift of a single resonance minimum at a steep angle of incidence is used to detect change in refractive index at the surface. However for our purposes this FOM is problematic for a number of reasons. Our structures exhibit complex resonances that don't fit a Lorentzian profile, making the assignment of a value of the FWHM to each peak a difficult and subjective exercise. Where quality factors have been quoted, peak height for the FWHM was measured approximately from the left-hand (low wavelength) 'shoulder' of the resonance dip to the resonance minimum, and thus the values must be considered estimates for this reason. Additionally, this FOM may also not be the most appropriate way of quantifying the sensing potential in a simplified bio-sensing set-up at normal incidence[100, 105].

Similar considerations prompted Becker *et al.*[105] to define an alternative figure of merit (FOM*) for LSPR resonances, where FOM* = $\left(\frac{dI/dn}{I}\right)_{max}$. This FOM* is more appropriate choice for our purposes. The simplified bio-sensing application which we propose for our structures would involve measuring changes in intensity in transmission, possibly with a laser at one wavelength, which could be chosen to achieve the maximum FOM*. This definition avoids the need to assign a subjective FWHM to each peak.

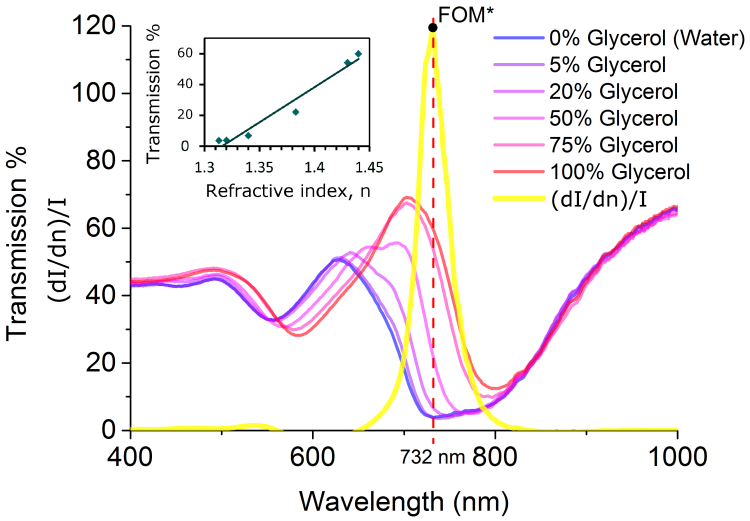

Figure 2.9 – Transmission variation with refractive index and $(dI/dn)/I$ variation with wavelength for the sample with the highest measured FOM* of 120. Nanostructures 210 x 210 x 200 nm, with period 450 nm. Inset: linear fit at the 732 nm peak of $(dI/dn)/I$ giving the FOM*.

All samples were measured in 6 different concentrations of glycerol solution in water[1], 0% (pure water), 5%, 20%, 50%, 75% and 100% (pure glycerol), which were measured to have refractive indices of 1.31, 1.32, 1.34, 1.38, 1.43, and 1.44 respectively in the wavelength range 800-1400 nm containing the resonance minima, varying by <1% over this range. The water/glycerol solutions and the sample were contained in a glass cuvette. The sensitivities were then calculated, the FOM was estimated and the FOM* was calculated using a linear fit for dλ/dn and dI/dn, and dividing by I for pure water. Calculated sensitivities were mostly around 300 nm/RIU, reaching 380 nm/RIU for structures 200 x 200 x 200 nm with period 600 nm. This corresponds to a FOM of approximately 13. These values compare favourably with typical sensitivities and FOMs for conventional (non collective) LSPR based approaches, which are typically around 200 nm/RIU and 2-10 respectively in similar conditions (700 nm excitation and $n = 1.33$)[100]. They do not compare well on paper to SPR based approaches though, which can exhibit sensitivity 3300 nm/RIU and FOM of 54 in the same conditions[100]. However, as the authors of the cited work explain[100], bulk sensitivities and FOMs are not always appropriate for many bio-sensing applications, where the sensing volume is typically very small and spatial resolution is very desirable. In these situations, LSPR based approaches often prove more sensitive in a practical sense (i.e. in terms of ng/cm^2 detection limits on the sample surface)[100].

Our highest measured FOM* was 120 at 732 nm, for the sample with structures 210 x 210 x 200 nm in size and array period 450 nm (figure 2.9). We measured FOM*s better than 40 up to detection wavelengths of 1000 nm. Interestingly, the highest FOM*s measured were not always for peaks with the highest estimated quality factor, rather

[1]Measurements in 5 - 75% water/ glycerol solutions were performed by Philip A. Thomas

they were often for wider, asymmetrical peaks where one side of a peak varied rapidly with changing refractive index, as in figure 2.9. This highlights the unsuitability of quality factor and the 'traditional' FOM for quantification of array bio-sensing potential in this configuration.

2.6 Explanation

The results presented here overcome the suppression of collective resonances by an asymmetric refractive index environment[102] by using carefully tuned combinations of periodicity and nanostructure size. Though multipole effects likely become relevant for larger nanostructures, an explanation of this effect exists within the coupled dipole model (section 1.6.1.1). Attaining the strongest collective resonances possible requires producing the ideal combination of parameters so that the real and imaginary components of the inverse polarisability α^{-1} and dipole sum S cancel as completely as possible (as described in section 1.6.1.1 and illustrated by example in figure 1.9). Large periodicities improve cancellation of the imaginary components $\mathrm{Im}(\alpha^{-1})$ and $\mathrm{Im}(S)$, which both approach zero in the long wavelength limit, while differing significantly at shorter wavelengths. A larger period then requires a correspondingly larger particle size to enable effective diffraction coupling as LSPR wavelength needs to be similar to the array period, and LSPR wavelength scales with nanostructure size. Additionally, having a tall nanostructure moves electron oscillation further from the substrate, mitigating the suppression effect of an asymmetric environment. Producing these optimal resonance conditions puts stringent requirements the nanostructure geometry. However, as shown in figure 2.6, using focusing optics relaxes the stringency of these requirements slightly by broadening the distribution and also shifts the ideal combination towards larger particle sizes.

2.7 Summary

We fabricated arrays supporting collective, diffraction coupled resonances which can be excited with light at normal incidence in asymmetric air and water environments. The nanostructure and array geometries were optimised for their bio and chemical sensing potential through several stages of experimental and theoretical investigation. We calculate a very high FOM* (up to 120 in water) for bio-sensing applications over a range of wavelengths from 700 to 1000 nm (FOM* from 40 - 120), as well as resonances of unusually high quality in air (Q~19) and water (Q~45). The high figure of merit coupled with the fact that the resonances were excited with focusing optics at normal incidence, make these structures well suited for sensing applications in asymmetric index environments, regaining some of the sensitivity of SPR while retaining the flexibility and spatial resolution of LSPR based approaches in a practical way.

Chapter 3

Extremely Narrow, High Quality Factor Collective Plasmon Resonances

Benjamin D. Thackray, Gregory H. Auton, Philip A. Thomas, Vasyl G. Kravets and Alexander N. Grigorenko

Presented in this chapter are extremely narrow collective plasmon resonances in nanostripe arrays on a gold substrate, with spectral line FWHM < 7 nm and quality factor Q of at least 210, at important fibre-optic telecommunications wavelengths around 1.5 μm.

(This work is prepared for publication, pending the inclusion of the latest results from our group, which extend and improve even further upon those presented here.)

My Contribution

I designed, fabricated and measured the initial samples with super-narrow resonances with the assistance of Gregory H. Auton for electron beam lithography. Philip A. Thomas has since picked up the idea and produced further samples of a similar geometry, including some identical except for small changes in the period and thus the position of the resonance minima. Two spectra from Philip's samples are included in figure 3.2. Vasyl G. Kravets and Alexander N. Grigorenko were a constant source of guidance and advice throughout.

3.1 Introduction

For many applications, especially sensing and modulation, it is advantageous to have the narrowest plasmon resonances possible. Propagating SPPs in continuous films generally have $Q < 20$ [55], and localised plasmon resonances in isolated nanoparticles

tend to be spectrally broad, limiting their usefulness for such applications. The spectral width of the resonance peak can be narrowed by coupling with resonance modes in nearby nanostructures, especially in the case of diffraction coupling in large arrays (section 1.6.1) , which can be employed to greatly improve resonance quality factors.

We added a continuous gold layer beneath an array of diffraction coupled gold lines, and observe a further, significant improvement in the quality factor of the collective resonances, due to an enhancement from the image dipole in the gold sublayer which can be understood by analogy with concepts from antenna theory. We are not the first to acknowledge this effect, as work published recently presented similar results at longer wavelengths, from 3 to 5 μm[110], with quality factors $Q > 200$ around 5 μm. To our knowledge, we have measured some of the highest recorded values of quality factor for collective resonances in diffraction coupled arrays of plasmonic nanostructures, measuring $Q > 210$ at around ~1.5 μm.

3.2 Fabrication details

Samples were fabricated on a glass substrate by electron beam lithography, as described previously (section 1.10.3). The substrate was in all cases coated in a 3 nm layer of chromium prior to lithography to prevent charging. For the samples from which the principal results are presented, a flat 100 μm x 300 μm, 65nm tall gold layer was then deposited by electron beam evaporation. In a second lithographic step, a 300 μm array of 100 μm long, 450nm wide gold stripes with a height of 70 nm were deposited atop this flat gold layer. These lines were fabricated with periods of 1463, 1485, 1550[1] and 1580[1] nm, measured in SEM after fabrication. An additional 3 nm of chromium was also deposited prior to each gold deposition step, for adhesion.

The additional results in figures 3 and 4 were fabricated in a similar way, except the gold contact area was instead 200 μm x 200 μm in size, and the stripe arrays covered a 100 μm x 100 μm area. Results are presented from samples with period 700 nm and stripe widths of 200 nm and 480 nm, and period 1000 nm with stripe width 245 nm. Samples with periods a = 700, 1000, 1500 and 2000 nm were made, each with 4 different nanostripes widths designed to be 1/5, 2/5, 3/5 and 4/5 of the sample period (though they came out a little larger - see the appendix). Almost all the samples produced very narrow resonances, especially for a = 700, 1000 and 1500 nm – only a selection of the best are presented (a more complete data set can be found in appendix A).

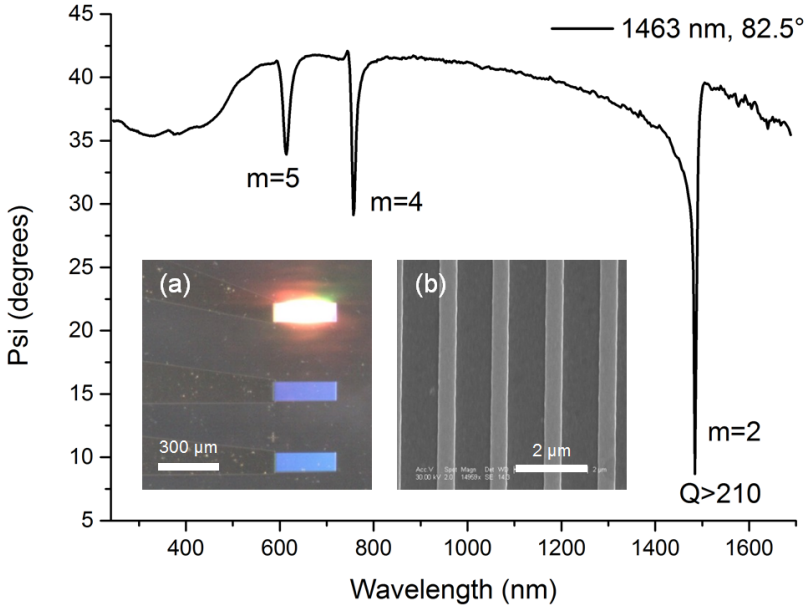

Figure 3.1 – A full 240 – 1700 nm ellipsometric spectrum of a sample producing a resonance of quality factor > 210 at 1484 nm (FWHM < 7 nm). The sample has lines 450 nm wide, with a period a = 1463 nm and was measured at an angle of incidence of $\theta = 82.5°$. Resonance minima are close to the expected position of the Rayleigh anomalies at $\lambda_R = \frac{a}{m}[1+\sin(\theta)]$with $m = 2,4,5$. Inset (a) is an optical image of a structure being measured under the ellipsometer beam, and inset (b) is an SEM image of the lines.

3.3 Results

One of the highest quality factor resonances is shown in figure 3.1, with quality factor $Q > 210$ at a wavelength of 1484 nm. The sample has lines 450 nm wide, with a period $a = 1463$ nm and was measured at an angle of incidence of $\theta = 82.5°$. This corresponds well with the expected position of the air Rayleigh cut-off wavelength at $\lambda_R = \frac{a}{m}[1 + \sin(\theta)]$, for $m = 2$, (which would be predicted to be at 1457 nm), as do the other peaks for the $m = 4$ and 5 modes.

Figures 3.2, 3.3 and 3.4 demonstrate that improvements to the collective resonances are not limited to one combination of array geometry, measurement angle and wavelength. Figure 3.2 demonstrates that super-narrow resonances can be achieved at a range of wavelengths around the 1.5 - 1.55 µm telecommunications standard, Figure 3.3 shows resonances achieved at shallower angles and different gold line thicknesses with an array period 700nm, and Figure 3.4 shows that high quality resonances with $Q > 70$ can be achieved over a wide range of angle of incidence. Additional results from different periods and line widths can be found in appendix A.

[1]Samples with periods 1550 and 1580 were fabricated by Philip A. Thomas, as part of a follow up to my work. Two spectra from Philip's samples are included in figure 3.2 only. It is worth noting that Philip was able to almost exactly reproduce the spectra measured on my samples.

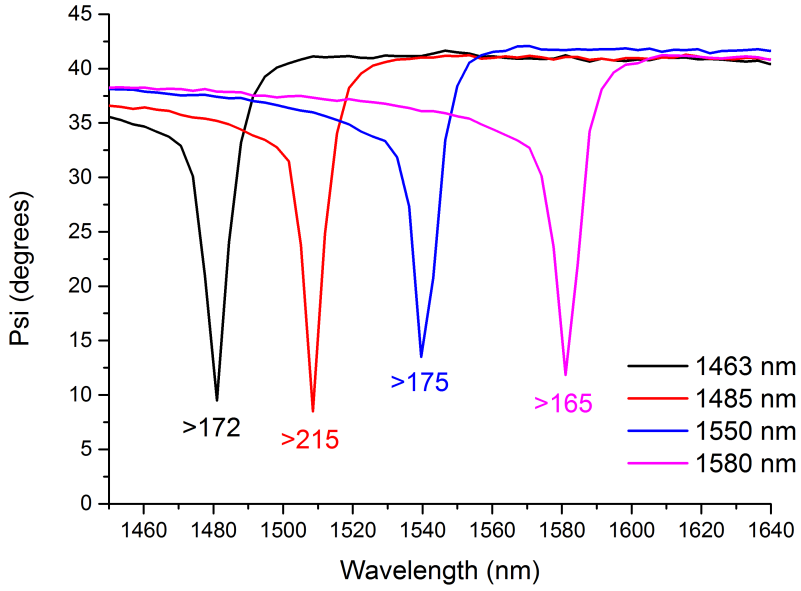

Figure 3.2 – Close up of the $m = 2$ resonance peaks of line arrays of various periods at angle of incidence of 80°. The lines were 450 nm wide in all cases, and lower-bound values of the quality factors are labelled beneath each peak.

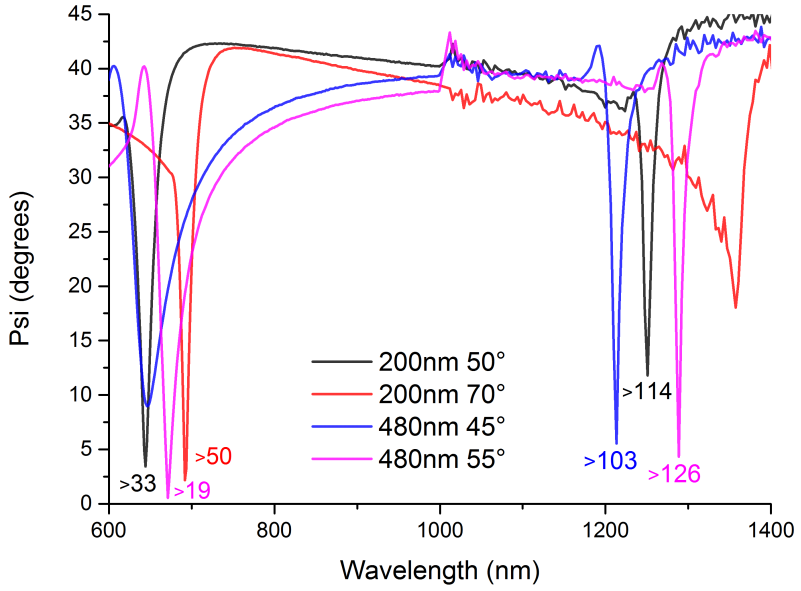

Figure 3.3 – Additional examples of high quality factor resonances measured on a sample with array period 700 nm. The widths of the gold lines and measurement angle of incidence are indicated on the graph, and each narrow peak is labelled with a lower-bound estimate of its quality factor.

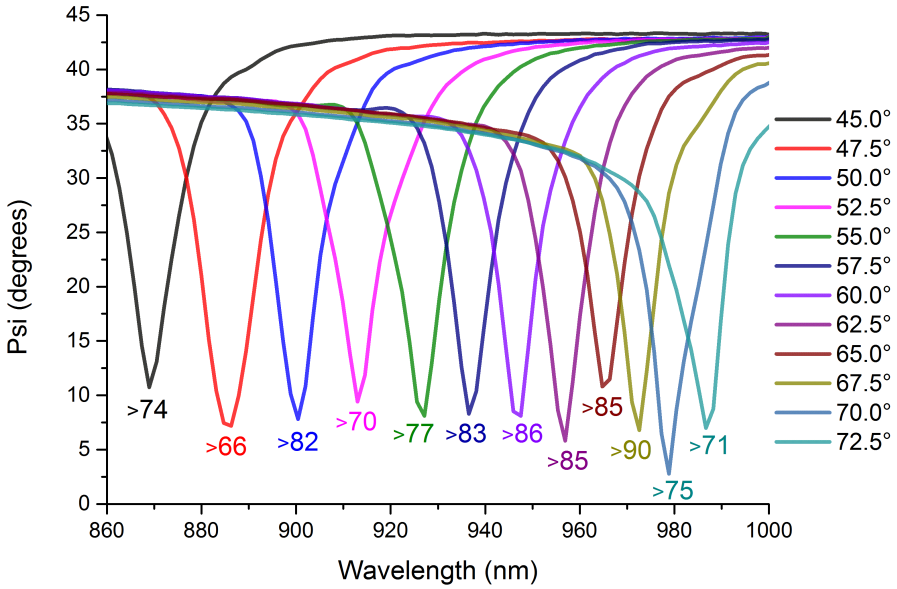

Figure 3.4 – Demonstration that narrow resonances can be attained at a range of angles-of-incidence. Spectra measured on a sample with period 1000 nm and stripe width 245 nm for angles of incidence from 45.0 to 72.5° in 2.5° steps. Minimum values of quality factor are indicated beneath each peak.

3.4 Discussion

All quality factors have been quoted as conservative lower-bound estimates. These were calculated by measuring peak depth from the highest value at the right hand shoulder of the line as plotted to the lowest value of Ψ of a measured data point. This would be expected to be a lower-bound estimate of the true value for two main reasons. Firstly, the peaks are asymmetric and do not perfectly fit a Lorentzian profile. By ignoring this asymmetry and measuring our baseline from the higher, right-hand shoulder of the peak we are effectively fitting them with a 'worst case' Lorentzian function and likely assigning them an unduly high FWHM. Secondly, the peaks are only a few nanometres wide, which is comparable to the wavelength sensitivity of our detector. It is likely that the true lowest value of Ψ for a peak does not align perfectly with a measurement wavelength, so we therefore expect to measure a higher minimum value of Ψ than the true value. This again acts to increase our estimate of the FWHM, leading us to underestimate our quality factor calculations. For these reasons we consider our presented values to be cautious lower-bound estimates of the true resonance quality factors, the highest of which likely exceed 250. Additionally, we have used focussing optics with numerical aperture 0.1 to measure the ellipsometric spectra, which we expect to reduce our measured resonance quality factors due to the effect of spatial decoherence (section 1.6.1.2). The significant effect of spatial decoherence is demonstrated in the supplementary information of reference [110].

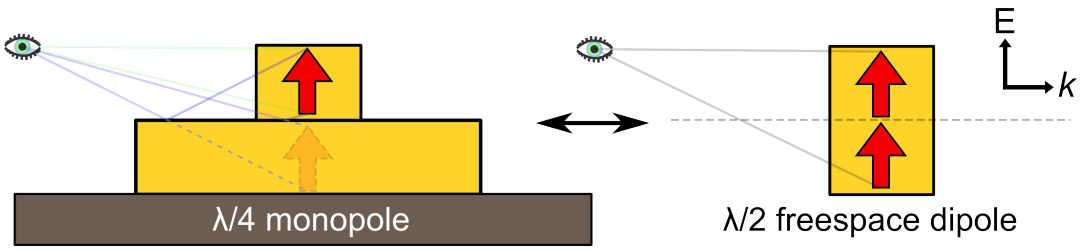

Figure 3.5 – Illustration of the equivalence of the radiation fields from a $\lambda/4$ monopole antenna over perfect ground (which should strictly be of infinite extent - in our case, this surface is a gold, near-perfect Drude metal mirror) and $\lambda/2$ dipole antennae with twice the voltage.

3.5 Explanation

It may not be immediately clear that this is the case, but the sample properties responsible for producing the exceptionally narrow and high quality factor resonances measured here are essentially the same as those shown to be important in the previous chapter. Namely, large structures facilitating strong out-of-plane electron resonances (and therefore coupling to the narrow sub-radiant lattice resonances[101]), combined with large array periods, and an index-matched environment. The first of these can be understood by analogy with concepts from the theory of antennae[110]. A monopole quarter-wave antenna over a perfect ground will radiate a field equivalent to that of a half-wave dipole antenna of twice the voltage. This is due to reflection from the ground, which is assumed to be an infinite perfect electron conductor. The situation on the surface of our samples is essentially identical, as illustrated in figure 3.5. Image charges in the gold sublayer screen and re-radiate the field scattered by the nanostripes, creating an overall scattered field similar to that that would be scattered by a nanostructure of twice the height (for out-of-plane electron oscillation). This is especially evident for excitation with light at grazing incidence, where the component of electric field normal to the plane is maximised (which is why the narrowest resonances were observed for the steepest angle of incidence around 80°). For light of $s-$polarisation, the dipole and its image would be antiparallel and cancel, thus this effect is highly polarisation selective. Production of this effect should only require that the gold sublayer is significantly thicker than the skin-depth, estimated as ~5 nm for gold at ~1.5 μm wavelengths. Since the image charges mirror the charge distribution in the nanostructure above, this has the added advantage of effectively removing the restrictions that asymmetric environments place on resonance quality factor[102] (as discussed in the previous chapter). The overall effect of the image in the gold sublayer to a far-field observer is to mimic a freespace dipole of twice the voltage, effectively eliminating the effect of the substrate.

In summary, the key factors that are responsible for the ultra-narrow resonances are essentially the same as those identified to be important in the previous chapter: Large nanostructures facilitating strong out-of-plane electron resonances (in this case,

enhanced by the image charges in the gold layer and with out-of-plane oscillation facilitated by the grazing angle of incidence) combined with a large periodicity, and the creation of a 'virtual' index-matched environment, removing the damping effect that the substrate refractive index mismatch can have on diffraction coupled resonances.

Modelling the sample geometry as a linear chain of 100 spheres may be a relatively crude approximation, but it is worth noting that the maximum values of extinction calculated with the couple dipole model in section 2.2 (figure 2.6), predicted a relationship $r = {}^{a}/_{6.30} - 28$ between for the optimal combinations of nanosphere radius r and array period a in air. For a = 1500 nm, this predicts an optimal radius of ~210 nm, or diameter of 420 nm (though not all data is shown in figure 2.6, calculations were performed up to a = 2000, r = 250, confirming the continuation of this trend [although the relevance of a simple dipolar model at large scales may become questionable]). When measuring with focussing optics the effects of spatial coherence must also be considered, which shifts the optimal combinations of array period and nanosphere radius towards higher radii (figure 2.6(d)) and this predicted radius should therefore be considered a lower bound.

3.6 Summary

Diffraction coupled plasmon resonances of exceptionally narrow spectral width and high quality factor were achieved by fabricating arrays of gold nanostripes on a gold sublayer. The effect is explained by analogy with well known results from the theory of antennae and attributed to image charges in the gold sublayer which create a radiation field equivalent to that of a resonant nanostructure of twice the height. This, coupled with excitation at a steep angle of incidence, creates strong out-of-plane electron oscillation. The gold sublayer also acts to mimic an index-matched environment and remove the damping effect of an asymmetric environment. The measured quality factors of up to $Q > 210$ are among the highest reported from arrays of diffraction coupled nanostructures at a wavelengths around 1.5 μm.

Chapter 4

Resistive Coupling of Localised Plasmon Resonances in Metallic Nanostripes through a Graphene Layer

Benjamin D. Thackray, Vasyl G. Kravets, Fred Schedin, Rashid Jalil and Alexander N. Grigorenko

We fabricated and studied hybrid graphene plasmonic devices consisting of a gold nanostripe array combined with graphene. Significant changes in the optical properties of the nanostripe array were measured after monolayer and bilayer graphene were transferred onto it. We suggest that this modification is partly due to resistive coupling of localised plasmon resonances through the highly mobile electrons of the graphene layer. These results suggest an approach towards designing active optical elements exploiting the high sensitivity of graphene carrier-density to bias voltage for ultra-fast light modulation. This is especially interesting as the plasmonic resonances of metal nanostructures can lie in the visible, near infra-red and ultra-violet; important areas for many applications.
(This work was published in *Journal of Optics* in 2013[54].)

My Contribution

I designed the samples with the assistance of Alexander N. Grigorenko and Vasyl G. Kravets. I fabricated the samples with the assistance of Vasyl G. Kravets at all stages, Fred Schedin for electron beam lithography, and Rashid Jalil for graphene flake transfer. I performed measurements on the samples with the assistance of Vasyl G. Kravets. Initial identification of the resistive coupling effect, and FDTD simulation studies were by Alexander N. Grigorenko.

4.1 Introduction

Graphene plasmonic devices have attracted recent attention with their potential applications for ultra-fast optical modulators, efficient photodetectors, photovoltaics, and ultra-sensitive chemical and bio-sensors[64, 65]. Plasmon resonances in noble metals such as silver and gold can be tuned over a wide range of frequencies, from ultraviolet to deep infra-red, generally by careful choice of design parameters that are defined at the point of fabrication, such as the materials and sample geometry. Changes in the dielectric constant of the environment induce resonance frequency shifts, which can be exploited for sensing[95], but these changes tend to be either slow or require high voltages. Fast modulation of plasmon resonances would be very desirable for optical applications, and could compete favourably with modulators based on cheap and small but slow liquid crystals, or fast but bulky and expensive nonlinear crystals[64]. Plain and structured graphene has long wavelength plasmon resonances in the infra-red to terahertz region (section 1.9) and, importantly, graphene resonance frequency and amplitude have been shown to be actively controlled by gate voltage[64, 66, 111]. However, graphene alone does not interact strongly with light, absorbing only ~2.3% of incident energy[67]. Metallic structures, on the other hand, can absorb nearly 100% of light in wide bandwidth range if fabricated with appropriate geometry[68]. Recently, there have been attempts to combine graphene and metal to create hybrid plasmonic devices exploiting the benefits offered by both materials[64]. These approaches may use metal plasmons to alter or enhance graphene-light interaction [69, 72, 73], use graphene to modify the resonances of metallic nanostructures [75, 76, 77], or exploit other properties of graphene, for example as an easily functionalisable coating, or as a reproducible probe for characterising sample properties such as Raman enhancement[55, 71, 78, 79, 112].

Few results relating to the effect of graphene on metal plasmon resonances in hybrid structures and the possibility for active control have yet been published. Kim *et al.* used bias voltage applied to a graphene layer to control the plasmon resonance of a single gold nanorod, shifting the LSPR resonance slightly and modulating the resonance quality factor by 28% by varying the bias over a range of 2 V [75]. These results were for resonance at telecommunications wavelengths around 1.5 μm. It has also been shown by Yang *et al.* that varying the separation between a graphene layer and randomly arranged gold nanoparticles on a surface with an Al_2O_3 spacer layer can create a shift in the resonance frequency of over 20 nm at optical frequencies[76, 77]. The spacer layers used in the two studies varied from 0.3 to 35nm, with saturation seen above 20 nm[76]. Xu *et al.* studied self-assembled silver nanoparticles on glass substrate coated with CVD graphene, as well as similar samples where the graphene layer was absent. They observed an increase in the transmittance near the silver plasmon resonance frequency of their samples when graphene layers were present, indicating that the graphene suppresses the localised plasmon resonances in the silver by

dissipating the electric field at the nanoparticle surfaces[112]. Simulation results and Raman measurements also support their conclusions.

We present evidence for a coupling mechanism that has so far received much less attention than near-field and radiative mechanisms - resistive coupling of plasmonic resonances through a conductive layer. It was shown previously that resistive coupling could strongly suppress plasmonic resonances and generate quantized transmission of light through an array of gold nanostructures on a conductive chromium or titanium sub-layer[53], where the effects of resistive coupling were seen as a modification to the optical response of an array of coupled plasmonic nanostructures even in the range far from the main plasmonic resonances (see section 1.7). The results presented here demonstrate that addition of graphene to an array of diffractive coupled gold nanostripes can significantly modify the optical response of the array. We partially attribute this effect to resistive coupling of the gold electron oscillations through the graphene conduction electrons.

4.2 Fabrication details

Gold nanostripes were fabricated on a glass substrate with 3 nm chromium adhesion layer by electron beam lithography, electron beam evaporation of gold and lift-off, as described in section 1.10.3. Two samples were made with gold stripes of differing average widths of 160 and 175 nm, and the same pitch of 320 nm, stripe height of 90 nm, and stripe length of 200 μm. The stripe arrays covered a $200 \times 200\ \mu m^2$ area. Stripe width length and pitch were confirmed by SEM and height was confirmed by quartz crystal microbalance during deposition. A schematic and SEM image of the structures can be seen in figure 4.1.

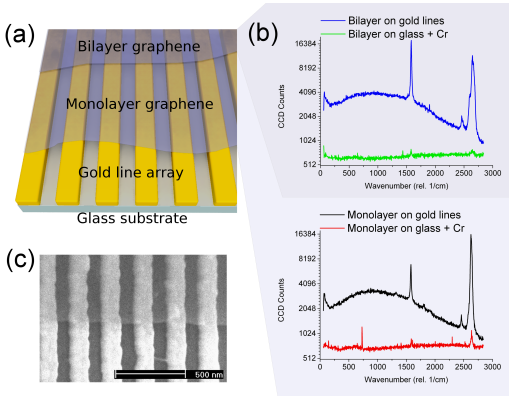

Figure 4.1 – Sample geometry. (a) Schematic diagram of sample. (b) Logarithmic plot of Raman spectra of bilayer and monolayer graphene on the gold structures and on the glass substrate with 3 nm Cr layer. The plasmonic Raman enhancement factor of the peaks (calculated using the maximum peak height above background) ranges from 30 to over 100. The high quality of the graphene is confirmed by the absence of a D-peak. (c) SEM image of the edge of the monolayer graphene on the gold lines.

Monolayer and bilayer graphene was then prepared by micro-mechanical cleavage of graphite[1], and transferred onto the metallic structures by the wet transfer method[113]. The presence, nature and high quality of the monolayer and bilayer graphene was confirmed by SEM and Raman spectroscopy (figure 4.1) Two samples were studied, one with 175 nm stripes

[1] Graphene transfer was performed by Rashid Jalil

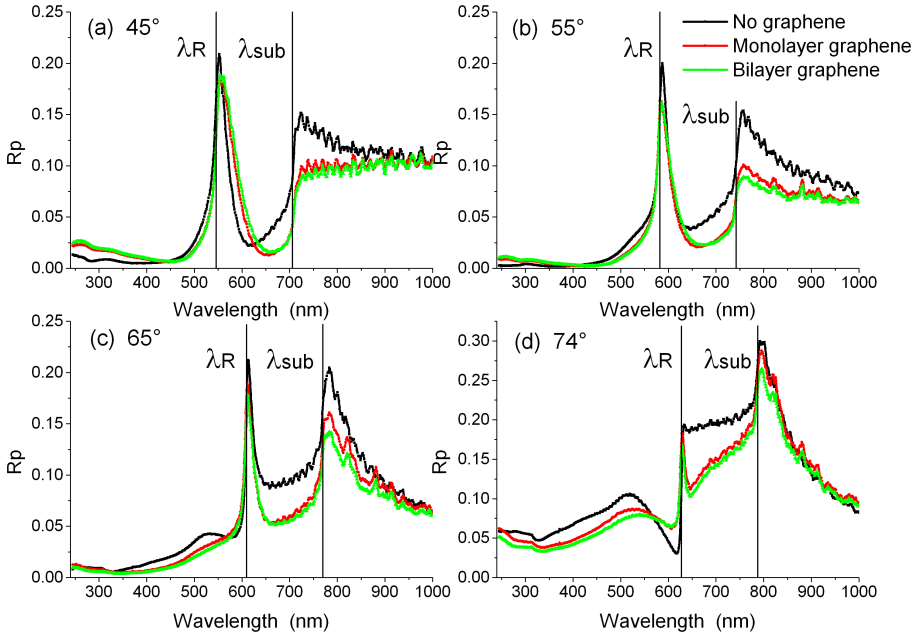

Figure 4.2 – Reflection spectra of the sample with 175 nm thick lines. The spectra were measured with $p-$polarised light before and after the addition of monolayer and bilayer graphene at four angles of incidence: (a) 45° (b) 55° (c) 65° (d) 74°. λ_R indicates the first air Rayleigh anomaly ($\lambda_R = a[1+\sin(\theta)]$, where a is the array period and θ is the angle of incidence) and λ_{sub} the resonance in the substrate ($\lambda_{sub} = a[n_s+\sin(\theta)]$, where n_s is the substrate refractive index).

and both monolayer and bilayer graphene, and a second with 160 nm stripes and only monolayer graphene. Both samples showed very similar effects upon addition of graphene, so only the results from the 175 nm sample are presented here, due to the additional presence of bilayer graphene.

4.3 Experimental results

Reflection spectra measured on the sample at various angles of incidence can be seen in figure 4.2. It is immediately clear that the presence of graphene results in a modification in the reflection coefficient R_P of up to ~10% over a wide range of wavelengths, increasing in bandwidth with increasing angle of incidence to span most of the visible spectrum at 74°. There is a much smaller, but still noteworthy difference between monolayer and bilayer, with bilayer having a similar but slightly more pronounced effect than monolayer graphene. A near-zero reflectivity plateau is seen at shorter wavelengths, most significantly at smaller angles of incidence. Figure 4.3 shows ellipsometric spectra measured at the same four angles of incidence. Again, there is a significant change upon addition of monolayer graphene, and a small increase in the magnitude of the effect when bilayer graphene is added. A significant difference from the reflection spectra however, is that the direction of the change reverses as the Brewster angle of the glass substrate is crossed. Shallower angles demonstrate a change in

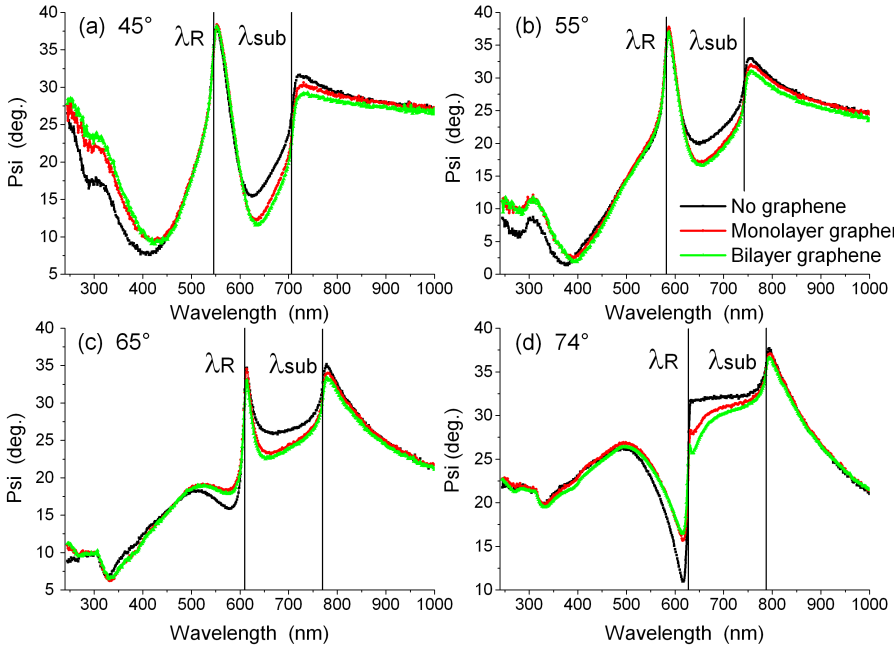

Figure 4.3 – Ellipsometry spectra of the sample with 175 nm thick lines. The spectra were measured before and after the addition of monolayer and bilayer graphene at four angles of incidence: (a) 45° (b) 55° (c) 65° (d) 74°. A significant modification can be seen after addition of the conducting layer. λ_R indicates the Rayleigh anomaly in the air and λ_{sub} the resonance in the substrate. Note that the graphene presence has the opposite effect on the optical reflection at either side of the Brewster angle.

the UV (perhaps due to the graphene Van Hove singularity[114]) which is absent for larger angles, and for all angles the magnitude of the effect decreases to zero in the infrared. This can be more clearly seen in figure 4.4, which shows the isolated effect of addition of monolayer graphene, calculated by subtraction of the reflection and ellipsometric spectra in absence of graphene from those when monolayer is added. The reflection spectra of figure 4.4(a) show modification of a similar nature (with some discrepancy at resonance) over the whole spectrum, which increases in magnitude with increasing angle of incidence. Figure 4.4(b) shows the abrupt flip in the sign of the modification as the substrate Brewster angle is crossed, and clearly shows that the difference tends to zero in the long wavelength limit.

A shift in the position of the plasmon resonance spectral minimum was also observed, as in previous studies[76, 77]. The direction of the shift tended to be towards longer wavelengths, and varied between 3 nm and 50 nm in magnitude. Larger shifts were seen in reflection than in ellipsometry, at smaller angles of incidence, and for bilayer when compared to monolayer. It should be noted that the error in the reflection coefficient R_P is larger than in the ellipsometric parameter Ψ. In the previous studies where the thickness of an Al_2O_3 spacer layer was varied, a blue shift of up to 29 nm was observed with spacer layer thickness from 0.3 - 15 nm[76, 77]. This previously observed blue-shift with increasing gold/ graphene separation can be better interpreted as a reduction in the red-shift that is induced by the addition of

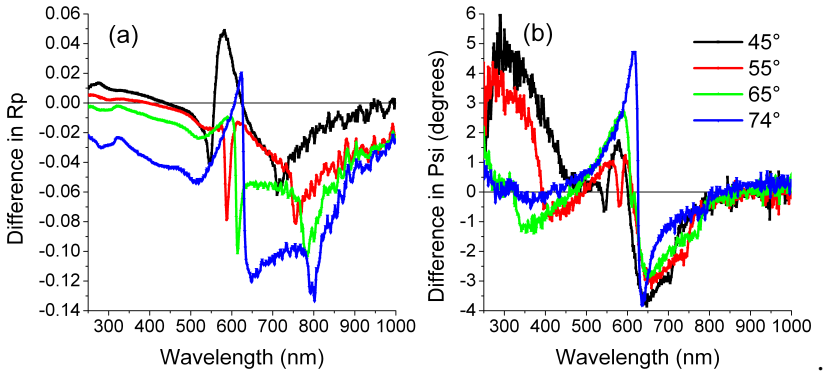

Figure 4.4 – Difference spectra due to the presence of monolayer graphene. (a) The difference in $p-$polarised reflection coefficient for four angles of incidence. (b) The difference in ellipsometric parameter Ψ for four angles of incidence. Care is advised before drawing any conclusions from the apparent monotone variation with angle of the difference in reflection above 800 nm, as the full data set displays a more complicated behaviour than is evident in the data shown. A point to note is that only at 45° does the reflection coefficient R_p tend to zero in the infrared, whereas the data from all 15 measured angles tended to zero in ellipsometry.

graphene, which can be seen by comparing their results from samples with graphene, gold and Al_2O_3 with their control samples where the graphene is absent. Though generally a red-shift was seen, we did observe a slight blue-shift to some of the resonances at higher angles of incidence upon graphene addition. This hints at a complex nature of the resonance position shift, and is echoed in Niu *et al.*'s results with thick spacer layers; where for spacer layer thicknesses of 15-20 nm a red-shift was instead observed[76]. The larger shifts in reflection than in ellipsometry and the fact that the difference in R_p in the long wavelength limit does not tend to zero, but the difference in ellipsometry does, both indicate variation in R_s. Variation in R_s could also explain the fact that both red- and blue-shifts of peak positions were observed.

4.4 Discussion

The first evidence for an additional resistive coupling between nanostructures induced by the presence of graphene comes from the large amplitude modification that is observed upon addition of monolayer, and the comparatively smaller difference between monolayer and bilayer. This indicates that the presence of a conducting layer is partly responsible for the effect and not just the change in local refractive index (the sample was also covered with non-conductive PMMA to confirm that no similar change was observed). The similar nature and only slightly increased magnitude of the effect in the areas with bilayer graphene also supports this hypothesis, as it shows that the increased conductivity of bilayer[115, 116] enhances the effect, but that it is the presence of a conducting layer that is principally responsible. The fact that the effect spans a large part of the visible spectrum also supports our hypothesis, indicating that the effect is not a resonant phenomenon, which is as we would

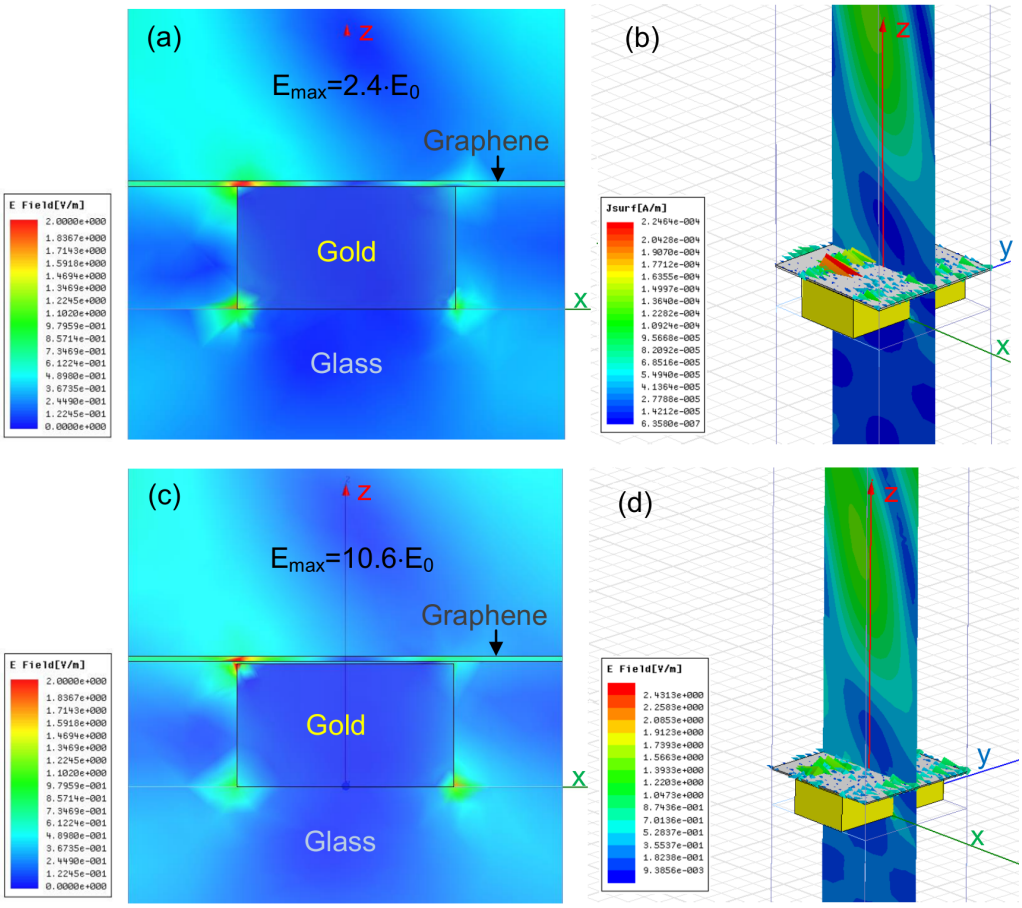

Figure 4.5 – FDTD modelling. The calculated distribution of field (z−cross-sections) and currents (graphene plane) for the elementary cell of the structure (320 nm x 320 nm) illuminated by p−polarized light under the angle of incidence of 65°. (a) and (b) correspond to the case of graphene being in direct (resistive) contact with metallic stripes; (c) and (d) corresponds to the case of graphene displaced by 2 nm from the top surface of gold nanostripes.

expect since graphene optical conductivity remains almost constant over the visible spectrum[67]. It is worth noting that it is likely that other factors such as doping[69] and image dipoles in the graphene layer[76, 77] could play a part in producing the effect.

In summary, our experiments show that the graphene affects the spectra well outside the region of localised plasmonic resonances, which is a signature of the resistive coupling. Additionally, the large effect of addition of monolayer is only slightly increased by the bilayer graphene of increased conductivity, suggesting that the presence of a conductive layer is key.

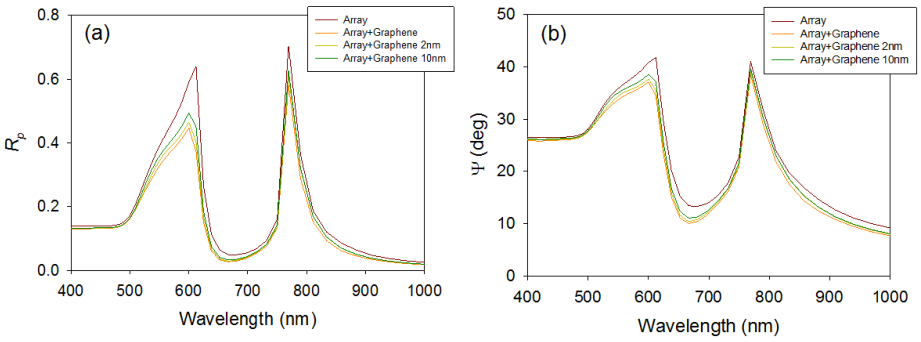

Figure 4.6 – FDTD modelling. (a) The calculated $p-$polarized reflection R_p and (b) ellipsometric parameter Ψ for the case of bare the plasmonic structure, the plasmonic structure with graphene on the top, and the plasmonic structure with a graphene sheet placed 2nm and 10nm above.

4.5 FDTD modelling[2]

To elucidate the nature of the coupling of the localised plasmons in the presence of graphene, we performed finite element analysis of our structures with the help of High Frequency Structure Simulator (HFSS11). The actual geometry of the samples was used in modelling and optical constants of gold films were extracted from spectroscopic ellipsometry measurements[68, 72] while graphene was modelled as a thin layer with conductivity given by the sheet graphene conductivity[64] divided by the thickness of the layer. Simulations clearly demonstrate that the presence of conductive graphene suppresses localised plasmonic resonances through the currents induced in the graphene sheet. For example, figure 4.5 shows the maps of the induced electric field, figure 4.5(a), (c), and currents in the graphene sheet, figure 4.5(b), (d), for the $p-$polarised light illuminating the arrays of nanostripes at the incidence angle of 65° (an elementary cell of 320 nm x 320 nm is shown; the structure is supposed to be periodic in both $x-$ and $y-$directions). For comparison, the solutions are provided for the cases where graphene is in direct contact with the gold nanostripes, figure 4.5(a), (b), and is displaced by 2 nm from the surface of the gold in a such a way that the resistive contact is absent, figure 4.5(c), (d). It is easy to see that the localised plasmonic resonances are suppressed in the presence of the resistive contact between gold and graphene (the maximal electric field enhancement developed in this case is only 2.4, figure 4.5(a) which is much smaller than the enhancement ratio of 10.6 observed for the case of the graphene displaced by 2 nm from the surface of the gold, figure 4.5(c)). FDTD modelling also confirms the presence of a net current flowing between nanostripes in case of resistive contact between graphene and gold, which is responsible for suppressing the localised plasmonic resonances; compare figure 4.5(b) and (d).

The influence of graphene on the collective resonances of the nanostripes can be

[2]FDTD modelling was performed by Alexander N. Grigorenko, and is presented for the justification it provides to the conclusions drawn.

seen in figure 4.6. We show the calculated R_P and Ψ for an angle of incidence of 65° without graphene and at several different positions of the graphene layer with respect to the surface of the sample (one in the direct contact with gold nanostripes, shifted by 2 nm and 10 nm above the stripes). One can see that there are spectral regions where the resistive coupling dominates (in the near infrared where the reflections for graphene displaced by 2 and 10 nm are the same) and also there are spectral regions where Ohmic losses in graphene provide the strongest contribution to the graphene influence on plasmonic resonances (visible and UV region where the reflections for graphene displaced by 2 and 10 nm are different).

To summarise, FDTD modelling supports the idea of currents in the graphene layer which suppress localised plasmonic resonances. This can be seen from the drop of the maximal field enhancement ratio for the graphene in contact with the gold stripes.

4.6 Summary

We have observed that a conductive graphene layer placed on top of an array of diffraction coupled nanostripes can modify their reflectance and ellipsometry over the visible spectrum by up to ~10%. We suggest that resistive coupling of the resonances through the graphene layer is partly responsible for this effect, though it remains for the relative contributions of various effects to be quantified. Active control of the resistive coupling effect by graphene gating would provide conclusive proof of our hypothesis. This is a more subtle experiment on which we are currently working. These results are promising due to their potential to enable the fabrication of ultrafast optical modulators, using bias voltage to rapidly modulate the carrier density of the graphene layer and thus the resistive coupling and optical properties.

Chapter 5

Cascaded Plasmon Resonances

Benjamin D. Thackray, Vasyl G. Kravets, Fred Schedin and Alexander N. Grigorenko

In this section I present results from an early area of investigation during my PhD, where I aimed to optimise structures for the cascaded enhancement of plasmon resonances. Some progress was made towards the optimisation of fabrication procedures, however practical considerations concerning the fabrication time and complicated measurement procedures ultimately led to this direction being abandoned in favour of the more productive projects presented above. Here I present an incremental improvement to the reliability of the fabrication process for the structures initially devised and fabricated by Kravets *et al.*[106, 107].

These structures could be used to reliably produce localised strong electromagnetic field enhancement for applications such as SERS and SEFS studies.

My Contribution

Here I built upon earlier work by the other three named contributors. My contribution was to devise and test an incremental improvement to the fabrication procedure. In practice this mostly involved a lot of calibration of deposition rates and testing of dyes for enhancement quantification. I modified a sample design previously devised, then fabricated samples with the assistance of Fred Schedin for electron beam lithography. Vasyl G. Kravets and Alexander N. Grigorenko again assisted and guided at all stages.

5.1 Cascaded enhancement

A novel approach for maximising local field intensities is to create plasmonic nanostructures that create a cascaded enhancement of the electromagnetic field. Application of self-similar nanostructures for cascaded field enhancement was suggested by Li, Stockman, and Bergman[117]. They suggested planar chains of metal spheres, decreasing in size and separation along the chain. They hypothesised that the perturbing effect of each subsequent smaller sphere on the field of the larger can be neg-

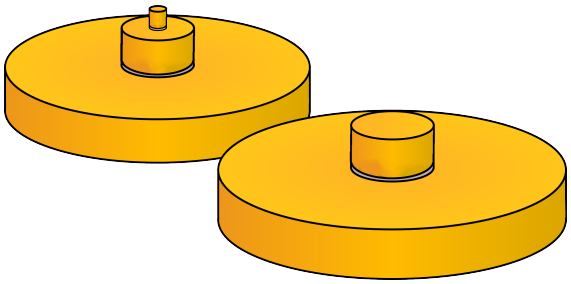

Figure 5.1 – Cartoon depiction of double (foreground) and triple (background) structures for cascaded electromagnetic field enhancement fabricated by Kravets *et al.* [106, 107].

lected, so that the smaller structure could be considered to be lying in the field generated by the larger one. Each larger structure will resonate in its exciting field and enhance the local electromagnetic field by a factor $Q \sim \frac{\mathrm{Re}(\epsilon(\omega))}{\mathrm{Im}(\epsilon(\omega))}$, which will in turn excite resonance with additional enhancement from the smaller sphere, and so on, resulting in a total enhancement factor $\sim Q^n$ for n spheres[117]. The idea was justified with simulation results, however when first tested experimentally, did not produce the predicted strong enhancement effects[107, 118].

Kravets *et al.* took this idea, but modified the geometry of the structure, exchanging the planar chain of spheres for an out-of-plane stack of discs. This proved successful, first for studies of surface enhanced fluorescence with double-structures made of two stacked discs with one cascaded enhancement step[106], and then for Raman studies on triple structures with an additional enhancement step, created by adding a third disc to the stack[107]. In this work we pursue the 'pagoda' type structures in [106], which were then developed to create the three-disc triple structures. These structures are depicted in figure 5.1 .

Few other papers have been published on cascaded field enhancement[119, 120]. A notable example is the work of Höppener *et al.*[121], who fabricated an antennae made of three gold nanospheres of sizes 80, 40 and 20 nm on a quartz tip, which are bonded by dithiol linker molecules, which also separate the particles by 2 nm to prevent electrical contact.

5.2 Fabrication optimisation

It was found in previous work, and confirmed in mine, that the optimal disc diameters for the structures fabricated by Kravets *et al.* were ~590-600 nm for the largest, annular disc, 100-110 nm for the second disc, and 30 nm for the smallest (where present)[107]. The two larger discs are deposited in the same deposition step, and so have a common thickness of ~90 nm, while a 100 nm diameter, 100 nm tall dielectric spacer concentric to both discs separates the two from electrical contact. The smallest discs are only ~30 nm tall, and separated by 10 nm of dielectric deposited by electron beam evaporation. A range of structure sizes and combinations close to

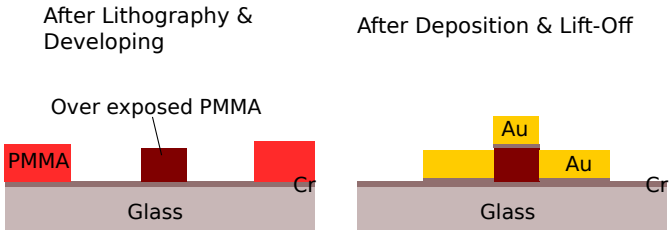

Figure 5.2 – Original fabrication procedure for double structures used by Kravets *et al.* [106, 107]

these optimised values were fabricated.

Kravets *et al.*[106, 107] reduced the number of lithography steps needed to fabricate the samples by employing a clever technique which allowed the PMMA resist to be used as both a positive and negative electron beam resist. Under normal exposure to an electron beam, PMMA will become more soluble in the developing solution (see section 1.10.3), however if the PMMA is strongly over-exposed, it can cross-link, and instead become insoluble. This allows both the pattern for the mould for the gold deposition step to be drawn, while also allowing the patterning of insoluble, dielectric structures on the surface. This technique was employed as illustrated in figure 5.2 to create two stacked gold discs (the largest actually an annular, doughnut shape surrounding the over-exposed PMMA) separated by a dielectric spacer of over-exposed PMMA in a single lithographic step. While this is a clever way to reduce the number of sample fabrication steps, I found that it came at the expense of sample reproducibility. In a survey of 188 structures, conducted by taking a number of SEM images at random locations on the arrays produced by the original method, I found that only 94 structures - exactly 50% of those measured - were well formed. Of the other 50%, 38, or approximately 20% had no smaller disc at all, and the remaining 56, or ~30%, had a smaller disc that was present but displaced due to poor adhesion to the over-exposed PMMA column. Examples of these three situations can be seen in the example SEM images shown in figure 5.4. Additionally it was found during sample use that the structures fabricated by this method degraded with repeated spin-coating of PMMA (containing low concentrations of suspended dye molecules, for fluorescence and Raman enhancement measurements), and subsequent removal of the PMMA/dye coating in acetone.

For these reasons, an improved fabrication method was developed, as depicted in figure 5.3. This approach replaces the over-exposed PMMA column with a similar structure fabricated from silicon dioxide deposited by electron beam evaporation in an additional lithographic step. This approach produced structures with a much higher level of reproducibility (estimated at over 90%), but at the cost of more complicated sample fabrication. 239 structures were assessed, as for the previous sample, and 217, or ~91% were found to be well formed. Of the remaining 22 structures, 21 had no smaller disc (~9%) and only one (~0%) had a disc where it was clear that gold

Figure 5.3 – Modified fabrication procedure for improved reproducibility.

adhesion had failed, but the small disk still remained. It is worth noting that for the samples fabricated with the original method, in almost all cases where there was no smaller gold disc the larger disc was still annular, with a hole in the centre. On the other hand, in all cases where the smaller disc was absent on the samples fabricated with the second method, the larger disc was solid, indicating that no dielectric column was present. This suggests that poor adhesion of chromium/ gold to the over-exposed PMMA column is the principal flaw of the original approach.

The successful samples fabricated with a silicon dioxide dielectric spacer were preceded by failed samples, where the layer thickness was inaccurate by more than 30%, and the dielectric constant of the film, measured by ellipsometry, was poor. It was discovered through many stages of testing and optimisation that for reliable deposition of a film of silicon dioxide of a given thickness it is important to scan the electron beam over a fresh target, using a deposition rate no higher than ~0.6 ångströms per second (typical deposition rate was around 0.2 - 0.4 Å/s with good results). It is also important that the material parameters for thickness calculation are well calibrated, and that a quartz crystal with more than 50% of its lifetime remaining to monitor the deposition process. Using these optimised deposition conditions, film thicknesses (measured with both the ellipsometer and profilometer, with good agreement) were reliable to within ~5%, with dielectric constant close to the desired 3.9.

5.3 Fluorescence and Raman enhancement

Calculation of cascaded enhancement factors, and the contributions from different components of the composite nanostructures (discussed at length in the supplementary information of reference [106]) is a complicated business. Fortunately, since the work in this chapter builds on previous results that have already demonstrated the validity of the cascaded enhancement effect, it is sufficient to show that the normalised integrated fluorescence enhancement measured from the full two-tier nano-

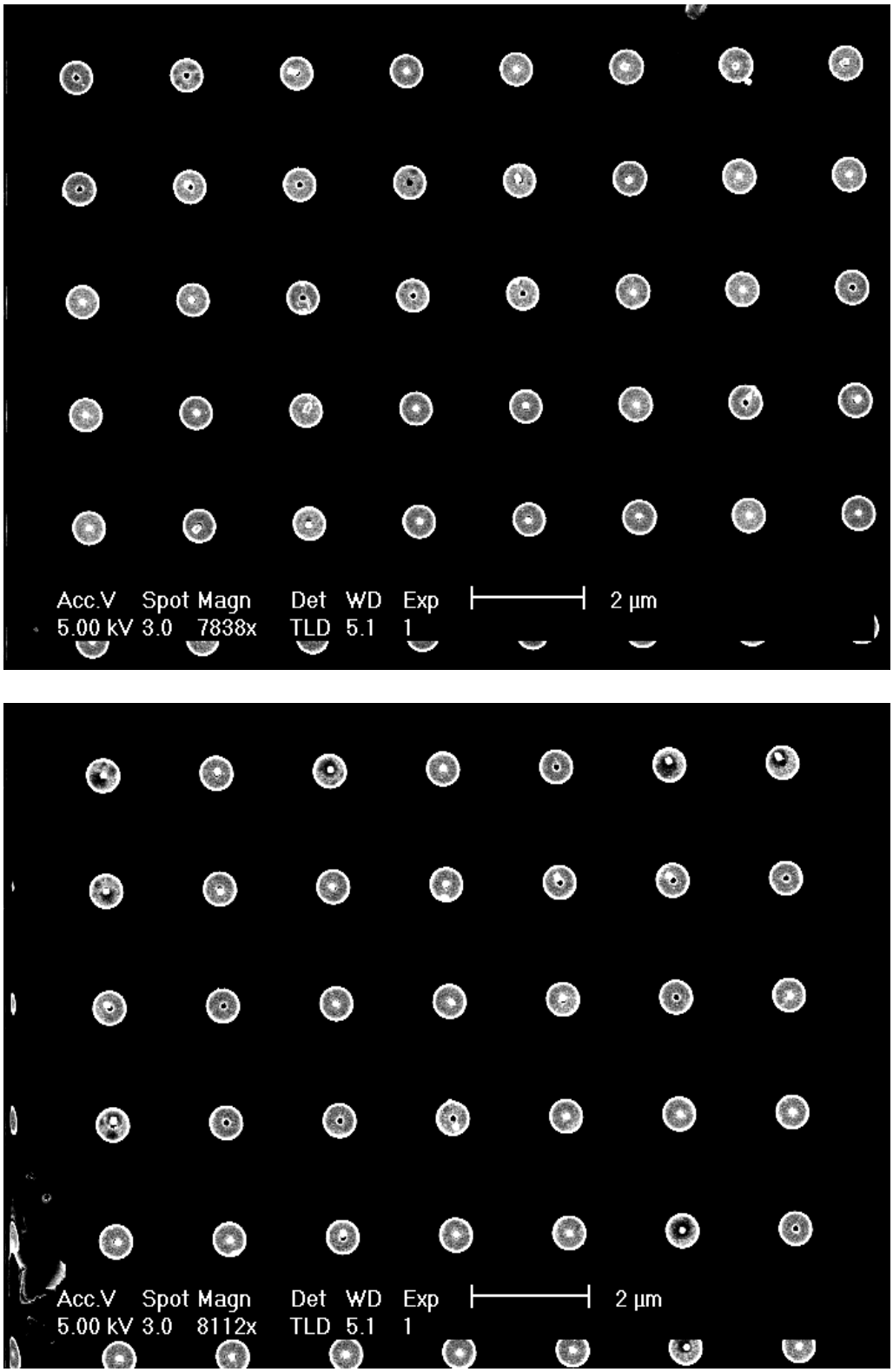

Figure 5.4 – Typical SEM images of double structures from samples made with the original method (figure 5.2).

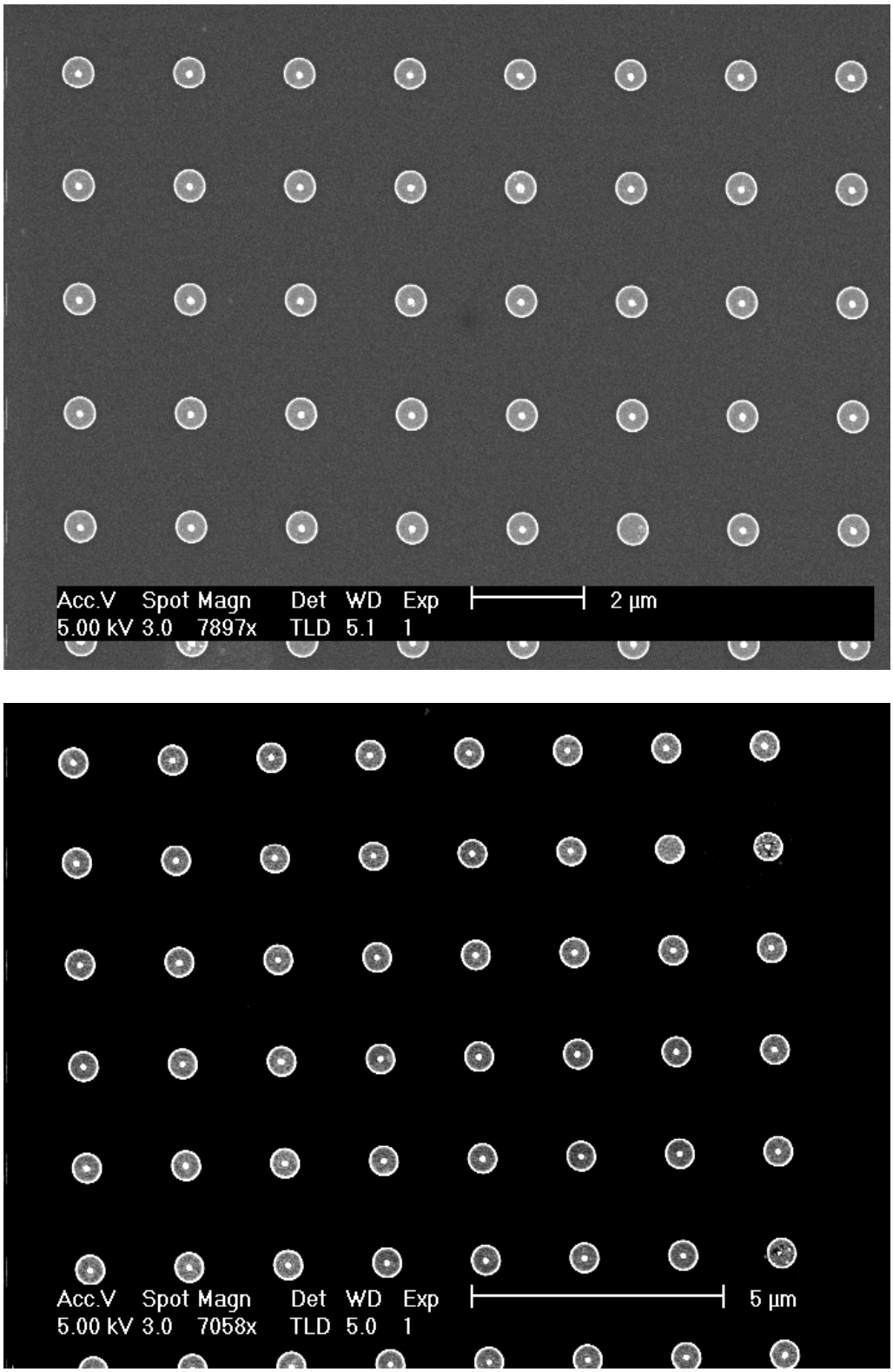

Figure 5.5 – Typical SEM images of double structures made with the modified fabrication method (figure 5.3).

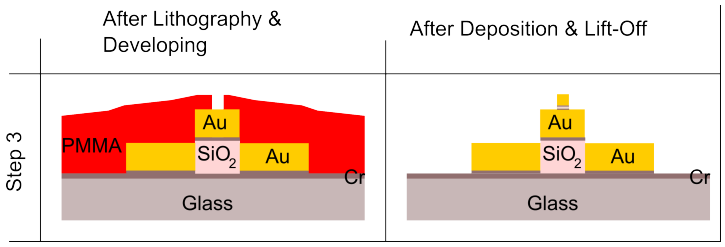

Figure 5.6 – The additional lithography step required to fabricate triple structures

structure when using the new fabrication method is comparable to that measured when using the previous fabrication method. Kravets *et al.* measured a normalised fluorescence of ~8-9 from the full nanostructure fabricated with the original method[106] (supplementary information). Measuring the normalised integrated fluorescence in the same way gives a value of ~7-10 on the nanostructure arrays fabricated with the improved method. Fluorescence spectra were integrated from 200 - 2000 rel. cm^{-1}, and the enhancement effect was found to be reproducible over the surface of the samples. It should be noted that I used a different dye, cresyl violet perchlorate, to that used in the previous work; oxazine 1 perchlorate. This was due to difficulty acquiring oxazine 1 perchlorate, and encouraging results from cresyl violet perchlorate while testing several dyes for their suitability for SEFS and SERS measurements. Cresyl violet perchlorate (CVP) was found to have more stable Raman peaks than those measured from rhodamine 6g and oxazine 750 perchlorate. The dye was dissolved in ethanol, and then mixed with PMMA (950k, 2%) in anisole, before being spin-coated over the sample and baked. Ethanol was used to disperse the dye and prevent agglomeration. The final molar concentration of the dye was 10^{-5} M (0.01 mol/m^3). It is assumed here that the SERS and SEFS enhancement factors measured are largely independent of choice of dye. The CVP Raman peak near 600 rel. cm^{-1} was integrated from 580-607 rel. cm^{-1} with the fluorescent background subtracted and an enhancement factor of 190 was calculated for double structures in comparison to just the larger discs alone. The background Raman signal in absence of any nanostructures was too weak to measure, even with very long integration times. Spectra from 45 structures were used to estimate the normalised integrated fluorescence and Raman enhancement factors.

Triple structures were also fabricated with the new method, however addition of the third disc showed no significant improvement in Raman or fluorescence enhancement over that measured on double structures. This is suspected to be a consequence of our decision (out of practical necessity) to use silicon dioxide as a spacer layer between the second gold disk and the smallest top disc, instead of the hafnium dioxide that was used for the triple structures of Kravets *et al.* Silicon dioxide is of significantly lower dielectric constant, and at film thickness of 10 nm is unlikely to form a continuous film, hence it is likely that the top discs were in electrical contact with the middle discs, preventing any cascaded enhancement effect.

5.4 Summary

An incremental but potentially significant improvement to the fabrication procedure for structures supporting cascaded enhancement of plasmon resonances for sensing, SEFS and SERS studies is presented. The method improved the fraction of well formed double structures from ~50% to over 90%, and SEFS measurements suggest that the cascaded enhancement effect in two-tier structures was not impaired.

Conclusion and Future Work

We have studied a variety of near and far-field coupling mechanisms of localised plasmon resonances which can create resonances with unique properties that would not be supported by individual nanostructures; as well as identifying evidence of a new resistive coupling mechanism which so far remains largely uninvestigated. This has included optimisation of arrays of diffraction coupled nanostructures for bio-sensing applications in asymmetric index environments at normal incidence in chapter 2. Quality factors as high as 19 and 45 were measured in air and water respectively. These samples produced a FOM* of 120 for bio-sensing applications, which is the highest value recorded to date, to the best of our knowledge. These results potentially make diffraction coupled LSPR a more viable alternative to SPR for many biosensing applications, particularly miniaturised point of care and 'lab on a chip' devices and in detection approaches combining surface plasmon based refractive index sensing with other sensing techniques such as surface enhanced Raman and fluorescence spectroscopy. Continuing to investigate diffraction coupled resonances in chapter 3, resonances of quality factor of at least 210 were measured at grazing incidence on arrays of nanostripes on a gold substrate. The gold layer can be used to increase the effective size of the nanostructures and mimic an index-matched environment, producing narrow, high quality factor resonances at wavelengths of around 1.5 μm. Narrow resonances in this wavelength range are of particular interest due to the importance of these wavelengths as a telecommunications standard. Evidence of an, at present, largely unrecognised resistive coupling mechanism was presented in chapter 4, which manifested as a significant (~10%) change in sample reflectance and ellipsometry upon addition of a graphene layer to an array of diffraction coupled gold nanostripes. Resistive coupling through graphene is particularly promising, as the fact that graphene charge carrier density can be modulated with a bias voltage implies that the resistive coupling effect, and thus sample optical properties, may also be modulated. Finally, in chapter 5, an improvement to the fabrication reproducibility of two-tier nanostructures for cascaded electromagnetic field enhancement was presented. These structures are interesting because of their potential for application for highly localised surface enhanced spectroscopy and sensing.

All these sections suggest further work. While refractive index sensitivity was measured using different concentrations of water/ glycerol solutions with different refract-

ive indices, it would be interesting to test the structures developed in chapter 2 in a real bio-sensing environment, where it is expected that their advantages would become even more apparent. Refractive index sensing could also be combined with surface enhanced Raman and fluorescence spectroscopy techniques, for which the substrates should be very well suited. Additionally, the potential for phase based measurements, which are already known to be capable of improving refractive index sensitivity by 1-2 orders of magnitude, has not yet been explored, and has the potential to push detection limits well beyond conventional SPR. Further work has already commenced, attempting to combine measurements on these structures with a transmission ellipsometry based technique for even higher detection sensitivity. Though results from the L-shaped nanostructures investigated in this chapter failed to produce strong resonances at normal incidence, there was evidence of strengthened resonance at shallow angles of incidence, which suggests that optimisation of the L-shaped geometry could yield interesting results.

Further work based on the results in chapters 3 and 4 is already under way. My attempt to combine the results of these two chapters, by transferring a layer of boron nitride and graphene onto an array exhibiting ultra-narrow diffraction coupled resonances on a gold substrate and applying bias voltage to modulate the resistive coupling effect, sadly failed. The work has since been picked up by Philip A. Thomas who has had much more luck, and has succeeded in producing the first evidence of a reproducible modulation effect with applied bias voltage. Philip has also recently further optimised the geometry of the samples with ultra-narrow resonances to increase their quality factors to exceed 300. There is significant work to be done in developing quantitative understanding of the resistive coupling effect, and optimisation of the samples to maximise modulation depth. Another approach under investigation involves fabricating a wave-guide atop the ultra-narrow diffraction coupled arrays, again with a graphene later for modulation.

Cascaded enhancement is a promising avenue of investigation that also remains relatively poorly investigated so far. Future work could include more rigorous verification of the fluorescence and Raman enhancement from the structures using a variety of dyes, or even graphene as a reproducible probe for Raman enhancement. Another approach that was initiated (but not completed in time for this thesis) was to use a monolayer of benzenethiol, deposited after the last lithography and gold deposition step but before lift-off, to precisely quantify the cascaded enhancement effect. Benzenethiol forms a monolayer on a gold surface, and has a strong Raman signature[122]. If deposited from the gas phase before lift-off in this way, a monolayer should form on top of the smallest structure only (as at this stage everything else is covered by a layer of PMMA and gold that is later removed), precisely probing the local electromagnetic field in this small (~30 nm diameter circular) area where enhancement should be very strong. This would hugely simplify the calculation of

enhancement factors, which as noted can be very complex and relies on statistical analysis. Additional further work on the cascaded enhancement effect could include investigating a wider variety of new nanostructure geometries, as well as methods to simplify the fabrication process without sacrificing reproducibility.

Bibliography

[1] R.W. Wood, "On a remarkable case of uneven distribution of light in a diffraction grating spectrum," *Philosophical Magazine*, vol. 4, 1902.

[2] Lord Rayleigh, "Note on the remarkable case of Diffraction Spectra described by Prof. Wood," *Philosophical Magazine*, vol. 14, p. 60, 1907.

[3] U. Fano, "The Theory of Anomalous Diffraction Gratings and of Quasi-Stationary Waves on Metallic Surfaces (Sommerfeld's Waves)," *Journal of the Optical Society of America*, vol. 31, pp. 213–222, 1941.

[4] A. Sommerfeld, "Über die Ausbreitung der Wellen in der drahtlosen Telegraphie," *Annalen der Physik*, vol. 333, pp. 665–736, 1909.

[5] J. Zenneck, "Über die Fortpflanzung ebener elektromagnetischer Wellen längs einer ebenen Leiterfläche und ihre Beziehung zur drahtlosen Telegraphie," *Annalen der Physik*, vol. 328, pp. 846–866, 1907.

[6] D. Pines and D. Bohm, "A Collective Description of Electron Interactions: II. Collective vs Individual Particle Aspects of the Interactions," *Physical Review*, vol. 85, pp. 338–353, 1952.

[7] R.H. Ritchie, "Plasma Losses by Fast Electrons in Thin Films," *Physical Review*, vol. 106, no. 5, pp. 874–881, 1957.

[8] E.C. Le Ru and P.G. Etchegoin, *Principles of Surface-Enhanced Raman Spectroscopy and related plasmonic effects*. Elsevier, 2008.

[9] H. Raether, *Surface plasmons on smooth and rough surfaces and on gratings*. Springer, 1988.

[10] P.R. West, S. Ishii , G.V. Naik, N.K. Emani, V.M. Shalaev, and A. Boltasseva, "Searching for better plasmonic materials," *Laser and Photonics Reviews*, vol. 4, 2010.

[11] A. Otto, "Excitation of Nonradiative Surface Plasma Waves in Silver by the Method of Frustrated Total Reflection," *Zeitschrift für Physik*, vol. 216, pp. 398–410, 1968.

[12] E. Kretschmann and H. Raether, "Radiative decay of non radiative surface plasmons excited by light," *Zeitschrift Für Naturforschung*, vol. 23a, pp. 2135–2136, 1968.

[13] M. Faraday, "Experimental relations of gold (and other metals) to light," *Philos. Trans. R. Soc. London*, vol. 147, pp. 145–181, 1857.

[14] S. K. Ghosh and T. Pal, "Interparticle coupling effect on the surface plasmon resonance of gold nanoparticles: From theory to applications," *Chemical Reviews*, vol. 107, no. 11, pp. 4797–4862, 2007.

[15] G. Mie, "Beiträge zur Optik trüber Medien, speziell kolloidaler Metallösungen," *Annalen der Physik*, vol. 330, pp. 377–452, 1908.

[16] G.C. Schatz and R.P. Van Duyne, *Electromagnetic Mechanism of Surface-enhanced Spectroscopy from Handbook of Vibrational Spectroscopy*. John Wiley & Sons, 2002.

[17] S.A. Maiera and H.A. Atwater, "Plasmonics: Localization and guiding of electromagnetic energy in metal/dielectric structures," *Journal of Applied Physics*, vol. 98, p. 011101, 2005.

[18] N. J. Halas, S. Lal, W.-S. Chang, S. Link, and P. Nordlander, "Plasmons in strongly coupled metallic nanostructures," *Chemical Reviews*, vol. 111, no. 6, pp. 3913–3961, 2011.

[19] A. N. Grigorenko, A. K. Geim, H. F. Gleeson, Y. Zhang, A. A. Firsov, I. Y. Khrushchev, and J. Petrovic, "Nanofabricated media with negative permeability at visible frequencies," *Nature*, vol. 438, no. 7066, pp. 335–338, 2005.

[20] M. Fleischmann, P.J. Hendra, A.J. McQuillan, "Raman spectra of pyridine adsorbed at a silver electrode," *Chemical Physics Letters*, vol. 26, pp. 163–166, 1974.

[21] M.G. Albrecht and J.A. Creighton, "Anomalously intense Raman spectra of pyridine at a silver electrode," *Journal of the American Chemical Society*, vol. 99, pp. 5215–5217, 1977.

[22] D.L. Jeanmaire, R.P. Van Duyne, "Surface raman spectroelectrochemistry: Part I. Heterocyclic, aromatic, and aliphatic amines adsorbed on the anodized silver electrode," *Journal of Electroanalytical Chemistry and Interfacial Electrochemistry*, vol. 84, pp. 1–20, 1977.

[23] M. Moskovits , "Surface-enhanced spectroscopy," *Reviews of Modern Physics*, vol. 57, pp. 783–826, 1985.

[24] A Otto, I Mrozek, H Grabhorn and W Akemann, "Surface-enhanced Raman scattering," *Journal of Physics: Condensed Matter*, vol. 4, pp. 1143–1212, 1992.

[25] B. Sharma, R. R. Frontiera, A-I. Henry, E. Ringe, and R. P. Van Duyne, "SERS: Materials, Applications, and the Future," *Materials Today*, vol. 15, pp. 16–25, 2012.

[26] K. Kneipp, M. Moskovits and H. Kneipp, "Surface-Enhanced Raman Scattering - Physics and Applications," *Topics in Applied Physics*, vol. 103, pp. 261–278, 2006.

[27] S.M. Nie and S.R. Emery, "Probing single molecules and single nanoparticles by surface-enhanced Raman scattering," *Science*, vol. 275, pp. 1102–1106, 1997.

[28] K. Kneipp, Y. Wang, H. Kneipp, L.T. Perelman, Irving Itzkan, Ramachandra R. Dasari, and Michael S. Feld , "Single molecule detection using surface enhanced Raman scattering (SERS)," *Physical Review Letters*, vol. 78, pp. 1667–1670, 1997.

[29] X.-M. Qian and S.M. Nie, "Single-molecule and single-nanoparticle SERS: from fundamental mechanisms to biomedical applications," *Chemical Society Reviews*, vol. 37, pp. 912–920, 2008.

[30] R.M. Jarvis, H.E. Johnson, E. Olembe, A. Panneerselvam, M.A. Malik, M. Afzaal, P. O'Brien and R. Goodacre, "Towards quantitatively reproducible substrates for SERS," *Analyst*, vol. 133, pp. 1449–14452, 2008.

[31] R.G. Freeman, K.C. Grabar, K.J. Allison, R.M. Bright, J.A. Davis, A.P. Guthrie, M.B. Hommer, M.A. Jackson, P.C. Smith, D.G. Walter and M.J. Natan, "Self-Assembled Metal Colloid Monolayers: An Approach to SERS Substrates," *Science*, vol. 267, pp. 1629–1632, 1995.

[32] C.J. Kiely, J. Fink, M. Brust, D. Bethell and D.J. Schiffrin, "Spontaneous ordering of bimodal ensembles of nanoscopic gold clusters," *Nature*, vol. 396, pp. 444–446, 1998.

[33] M.J. Banholzer, J.E. Millstone, L. Qin and C.A. Mirkin, "Rationally designed nanostructures for surface-enhanced Raman spectroscopy," *Chemical Society Reviews*, vol. 37, pp. 885–897, 2008.

[34] Wenfang Hu and Shengli Zou, "Proposed Substrates for Reproducible Surface-Enhanced Raman Scattering Detection," *The Journal of Physical Chemistry C*, vol. 115, pp. 4523–4532, 2011.

[35] M.S. Schmidt, J.K. Olsen, A. Boisen and J. Hübner, "Nanostructured surface enhanced Raman scattering substrates for explosives detection," *Sensors 2010 IEEE*, pp. 2634–2637, 2010.

[36] P.L. Stiles, J.A. Dieringer, N.C. Shah, and R.P. Van Duyne, "Surface-Enhanced Raman Spectroscopy," *Annual Reviews of Analytical Chemistry*, vol. 1, pp. 601–626, 2008.

[37] W.H. Yang, G.C. Schatz, and R.P. Van Duyne, "Discrete dipole approximation for calculating extinction and Raman intensities for small particles with arbitrary shapes," *Journal of Chemical Physics*, vol. 103, pp. 869–875, 1995.

[38] E. Fort and S. Grésillon, "Surface enhanced fluorescence," *Journal of Physics D: Applied Physics*, vol. 41, p. 013001, 2008.

[39] J.N. Anker, W.P. Hall, O. Lyandres, N.C. Shah, J. Zhao and R.P. Van Duyne, "Biosensing with plasmonic nanosensors," *Nature Materials*, vol. 7, pp. 442–453, 2008.

[40] E.C. Le Ru, P.G. Etchegoin, "Rigorous justification of the $|E|^4$ enhancement factor in Surface Enhanced Raman Spectroscopy," *Chemical Physics Letters*, vol. 423, pp. 63–66, 2006.

[41] K. T. Carron, W. Fluhr, M. Meier, A. Wokaun, and H. W. Lehmann, "Resonances of two-dimensional particle gratings in surface-enhanced Raman scattering," *J. Opt. Soc. Am. B*, vol. 3, no. 3, pp. 430–440, 1986.

[42] V. Markel, "Coupled-dipole approach to scattering of light from a one-dimensional periodic dipole structure," *Journal of Modern Optics*, vol. 40, no. 11, pp. 2281–2291, 1993.

[43] S. Zou, N. Janel, and G. C. Schatz, "Silver nanoparticle array structures that produce remarkably narrow plasmon lineshapes," *The Journal of Chemical Physics*, vol. 120, no. 23, pp. 10871–10875, 2004.

[44] V. A. Markel, "Divergence of dipole sums and the nature of non-lorentzian exponentially narrow resonances in one-dimensional periodic arrays of nanospheres," *Journal of Physics B: Atomic, Molecular and Optical Physics*, vol. 38, no. 7, p. L115, 2005.

[45] S. Zou and G. C. Schatz, "Theoretical studies of plasmon resonances in one-dimensional nanoparticle chains: narrow lineshapes with tunable widths," *Nanotechnology*, vol. 17, no. 11, p. 2813, 2006.

[46] V. A. Markel and A. K. Sarychev, "Propagation of surface plasmons in ordered and disordered chains of metal nanospheres," *Phys. Rev. B*, vol. 75, no. 8, p. 085426, 2007.

[47] C. L. Haynes, A. D. McFarland, L. Zhao, R. P. Van Duyne, G. C. Schatz, L. Gunnarsson, J. Prikulis, B. Kasemo, and M. Käll, "Nanoparticle optics: The importance of radiative dipole coupling in two-dimensional nanoparticle arrays," *The Journal of Physical Chemistry B*, vol. 107, no. 30, pp. 7337–7342, 2003.

[48] E. M. Hicks, S. Zou, G. C. Schatz, K. G. Spears, R. P. Van Duyne, L. Gunnarsson, T. Rindzevicius, B. Kasemo, and M. Käll, "Controlling plasmon line shapes through diffractive coupling in linear arrays of cylindrical nanoparticles fabricated by electron beam lithography," *Nano Letters*, vol. 5, no. 6, pp. 1065–1070, 2005.

[49] J. Sung, E. M. Hicks, R. P. Van Duyne, and K. G. Spears, "Nanoparticle spectroscopy: Plasmon coupling in finite-sized two-dimensional arrays of cylindrical silver nanoparticles," *The Journal of Physical Chemistry C*, vol. 112, no. 11, pp. 4091–4096, 2008.

[50] B. Lamprecht, G. Schider, R. T. Lechner, H. Ditlbacher, J. R. Krenn, A. Leitner, and F. R. Aussenegg, "Metal nanoparticle gratings: Influence of dipolar particle interaction on the plasmon resonance," *Phys. Rev. Lett.*, vol. 84, no. 20, pp. 4721–4724, 2000.

[51] V. G. Kravets, F. Schedin, and A. N. Grigorenko, "Extremely narrow plasmon resonances based on diffraction coupling of localized plasmons in arrays of metallic nanoparticles," *Phys. Rev. Lett.*, vol. 101, no. 8, p. 087403, 2008.

[52] B. Auguié and W. L. Barnes, "Collective resonances in gold nanoparticle arrays," *Phys. Rev. Lett.*, vol. 101, no. 14, p. 143902, 2008.

[53] V. Kravets, F. Schedin, and A. Grigorenko, "Fine structure constant and quantized optical transparency of plasmonic nanoarrays," *Nat Commun*, vol. 3, 640, 2012.

[54] B. Thackray, V. G. Kravets, F. Schedin, R. Jalil, and A. N. Grigorenko, "Resistive coupling of localized plasmon resonances in metallic nanostripes through a graphene layer," *Journal of Optics*, vol. 15, no. 11, p. 114002, 2013.

[55] V. G. Kravets, R. Jalil, Y.-J. Kim, D. Ansell, D. E. Aznakayeva, B. Thackray, L. Britnell, B. D. Belle, F. Withers, I. P. Radko, Z. Han, S. I. Bozhevolnyi, K. S. Novoselov, A. K. Geim, and A. N. Grigorenko, "Graphene-protected copper and silver plasmonics," *Sci. Rep.*, vol. 4, article 5517, 2014.

[56] H.-M Bok, K. L. Shuford, S. Kim, S.K. Kim, and S. Park, "Multiple Surface Plasmon Modes for Gold/Silver Alloy Nanorods," *Langmuir*, vol. 25, pp. 5266–5270, 2009.

[57] S. Link, Z.L. Wang, and M.A. El-Sayed, "Alloy Formation of Gold-Silver Nanoparticles and the Dependence of the Plasmon Absorption on Their Composition," *Journal of Physical Chemistry B*, vol. 103, pp. 3529–3533, 1999.

[58] K. S. Novoselov, A. K. Geim, S. V. Morozov, D. Jiang, Y. Zhang, S. V. Dubonos, I. V. Grigorieva, and A. A. Firsov, "Electric field effect in atomically thin carbon films," *Science*, vol. 306, no. 5696, pp. 666–669, 2004.

[59] A. K. Geim and K. S. Novoselov, "The rise of graphene," *Nat Mater*, vol. 6, no. 3, pp. 183–191, 2007.

[60] S. V. Morozov, K. S. Novoselov, M. I. Katsnelson, F. Schedin, D. C. Elias, J. A. Jaszczak, and A. K. Geim, "Giant intrinsic carrier mobilities in graphene and its bilayer," *Phys. Rev. Lett.*, vol. 100, no. 1, p. 016602, 2008.

[61] K. Bolotin, K. Sikes, Z. Jiang, M. Klima, G. Fudenberg, J. Hone, P. Kim, and H. Stormer, "Ultrahigh electron mobility in suspended graphene," *Solid State Communications*, vol. 146, pp. 351–355, 2008.

[62] G.-H. Lee, R. C. Cooper, S. J. An, S. Lee, A. van der Zande, N. Petrone, A. G. Hammerberg, C. Lee, B. Crawford, W. Oliver, J. W. Kysar, and J. Hone, "High-strength chemical-vapor deposited graphene and grain boundaries," *Science*, vol. 340, no. 6136, pp. 1073–1076, 2013.

[63] V. Berry, "Impermeability of graphene and its applications," *Carbon*, vol. 62, no. 0, pp. 1–10, 2013.

[64] A. N. Grigorenko, M. Polini, and K. S. Novoselov, "Graphene plasmonics," *Nat Photon*, vol. 6, no. 11, pp. 749–758, 2012.

[65] F. H. L. Koppens, D. E. Chang, and F. J. García de Abajo, "Graphene plasmonics: A platform for strong light-matter interactions," *Nano Lett.*, vol. 11, no. 8, pp. 3370–3377, 2011.

[66] Z. Fei, A. S. Rodin, G. O. Andreev, W. Bao, A. S. McLeod, M. Wagner, L. M. Zhang, Z. Zhao, M. Thiemens, G. Dominguez, M. M. Fogler, A. H. C. Neto, C. N. Lau, F. Keilmann, and D. N. Basov, "Gate-tuning of graphene plasmons revealed by infrared nano-imaging," *Nature*, vol. 487, no. 7405, pp. 82–85, 2012.

[67] R. R. Nair, P. Blake, A. N. Grigorenko, K. S. Novoselov, T. J. Booth, T. Stauber, N. M. R. Peres, and A. K. Geim, "Fine structure constant defines visual transparency of graphene," *Science*, vol. 320, no. 5881, p. 1308, 2008.

[68] V. G. Kravets, F. Schedin, and A. N. Grigorenko, "Plasmonic blackbody: Almost complete absorption of light in nanostructured metallic coatings," *Phys. Rev. B*, vol. 78, no. 20, p. 205405, 2008.

[69] F. Schedin, E. Lidorikis, A. Lombardo, V. G. Kravets, A. K. Geim, A. N. Grigorenko, K. S. Novoselov, and A. C. Ferrari, "Surface-Enhanced Raman Spectroscopy of Graphene," *ACS Nano*, vol. 4, no. 10, pp. 5617–5626, 2010.

[70] M. Khorasaninejad, S. M. Raeis-Zadeh, S. Jafarlou, M. J. Wesolowski, C. R. Daley, J. B. Flannery, J. Forrest, S. Safavi-Naeini, and S. S. Saini, "Highly enhanced Raman scattering of graphene using plasmonic nano-structure," *Sci. Rep.*, vol. 3, 2936, 2013.

[71] V. G. Kravets, F. Schedin, R. Jalil, L. Britnell, K. S. Novoselov, and A. N. Grigorenko, "Surface hydrogenation and optics of a graphene sheet transferred onto a plasmonic nanoarray," *J. Phys. Chem. C*, vol. 116, no. 6, pp. 3882–3887, 2012.

[72] T. Echtermeyer, L. Britnell, P. Jasnos, A. Lombardo, R. Gorbachev, A. Grigorenko, A. Geim, A. Ferrari, and K. Novoselov, "Strong plasmonic enhancement of photovoltage in graphene," *Nat Commun*, vol. 2, 458, 2011.

[73] Y. Liu, R. Cheng, L. Liao, H. Zhou, J. Bai, G. Liu, L. Liu, Y. Huang, and X. Duan, "Plasmon resonance enhanced multicolour photodetection by graphene," *Nat Commun*, vol. 2, 579, 2011.

[74] X. Zhu, L. Shi, M. S. Schmidt, A. Boisen, O. Hansen, J. Zi, S. Xiao, and N. A. Mortensen, "Enhanced light-matter interactions in graphene-covered gold nanovoid arrays," *Nano Lett.*, vol. 13, no. 10, pp. 4690–4696, 2013.

[75] J. Kim, H. Son, D. J. Cho, B. Geng, W. Regan, S. Shi, K. Kim, A. Zettl, Y.-R. Shen, and F. Wang, "Electrical control of optical plasmon resonance with graphene," *Nano Lett.*, vol. 12, no. 11, pp. 5598–5602, 2012.

[76] J. Niu, Y. J. Shin, J. Son, Y. Lee, J.-H. Ahn, and H. Yang, "Shifting of surface plasmon resonance due to electromagnetic coupling between graphene and Au nanoparticles," *Opt. Express*, vol. 20, no. 18, pp. 19690–19696, 2012.

[77] J. Niu, Y. Jun Shin, Y. Lee, J.-H. Ahn, and H. Yang, "Graphene induced tunability of the surface plasmon resonance," *Applied Physics Letters*, vol. 100, no. 6, 061116, 2012.

[78] L. Wu, H. S. Chu, W. S. Koh, and E. P. Li, "Highly sensitive graphene biosensors based on surface plasmon resonance," *Opt. Express*, vol. 18, no. 14, pp. 14395–14400, 2010.

[79] V. G. Kravets, F. Schedin, R. Jalil, L. Britnell, R. V. Gorbachev, D. Ansell, B. Thackray, K. S. Novoselov, A. K. Geim, A. V. Kabashin, and A. N. Grigorenko, "Singular phase nano-optics in plasmonic metamaterials for label-free single-molecule detection," *Nat Mater*, vol. 12, no. 4, pp. 304–309, 2013.

[80] *http://www.azom.com/article.aspx?ArticleID=2950*, accessed 20/08/2014.

[81] *http://www.jawoollam.com/faq.html*, accessed 29/08/2014.

[82] B. D. Thackray, V. G. Kravets, F. Schedin, G. Auton, P. A. Thomas, and A. N. Grigorenko, "Narrow collective plasmon resonances in nanostructure arrays observed at normal light incidence for simplified sensing in asymmetric air and water environments," *ACS Photonics*, vol. 1, no. 11, pp. 1116–1126, 2014.

[83] V. G. Kravets, F. Schedin, A. V. Kabashin, and A. N. Grigorenko, "Sensitivity of collective plasmon modes of gold nanoresonators to local environment," *Optics Letters*, vol. 35, no. 7, pp. 956–958, 2010.

[84] H. J. Lee, D. Nedelkov, and R. M. Corn, "Surface plasmon resonance imaging measurements of antibody arrays for the multiplexed detection of low molecular weight protein biomarkers," *Analytical Chemistry*, vol. 78, no. 18, pp. 6504–6510, 2006.

[85] K. V. Gobi, H. Iwasaka, and N. Miura, "Self-assembled PEG monolayer based SPR immunosensor for label-free detection of insulin," *Biosensors and Bioelectronics*, vol. 22, no. 7, pp. 1382–1389, 2007.

[86] I. Mannelli, M. Minunni, S. Tombelli, R. Wang, M. Michela Spiriti, and M. Mascini, "Direct immobilisation of DNA probes for the development of affinity biosensors," *Bioelectrochemistry*, vol. 66, pp. 129–138, 2005.

[87] B. Liedberg, C. Nylander and I. Lunström, "Surface plasmon resonance for gas detection and biosensing," *Sensors and Actuators*, vol. 4, pp. 299–304, 1983.

[88] B. Liedberg, C. Nylander and I. Lundström, "Biosensing with surface plasmon resonance–how it all started.," *Biosens Bioelectron.*, vol. 10, no. 8, pp. i–ix, 1995.

[89] R. L. Rich and D. G. Myszka, "Grading the commercial optical biosensor literature - class of 2008: "the mighty binders"," *Journal of Molecular Recognition*, vol. 23, no. 1, pp. 1–64, 2010.

[90] J. H. T. Luong, K. B. Male, and J. D. Glennon, "Biosensor technology: Technology push versus market pull," *Biotechnology Advances*, vol. 26, no. 5, pp. 492–500, 2008.

[91] S. Lofas and B. Johnsson, "A novel hydrogel matrix on gold surfaces in surface plasmon resonance sonsors for fast en efficient covalent immobilization of ligands," *Journal of the Chemical Society, Chemical Communications*, vol. 21, pp. 1526–1528, 1990.

[92] X. Guo, "Surface plasmon resonance based biosensor technique: A review," *Journal of Biophotonics*, vol. 5, no. 7, pp. 483–501, 2012.

[93] Y. Tang, X. Zeng, and J. Liang, "Surface plasmon resonance: An introduction to a surface spectroscopy technique," *Journal of Chemical Education*, vol. 87, no. 7, pp. 742–746, 2010.

[94] A. G. Brolo, "Plasmonics for future biosensors," *Nat Photon*, vol. 6, pp. 709–713, Nov. 2012.

[95] J. N. Anker, W. P. Hall, O. Lyandres, N. C. Shah, J. Zhao, and R. P. Van Duyne, "Biosensing with plasmonic nanosensors," *Nat Mater*, vol. 7, no. 6, pp. 442–453, 2008.

[96] A. J. Haes, L. Chang, W. L. Klein, and R. P. Van Duyne, "Detection of a biomarker for Alzheimer's disease from synthetic and clinical samples using a nanoscale optical biosensor," *Journal of the American Chemical Society*, vol. 127, no. 7, pp. 2264–2271, 2005.

[97] K. A. Willets and R. P. Van Duyne, "Localized surface plasmon resonance spectroscopy and sensing," *Annual Review of Physical Chemistry*, vol. 58, no. 1, pp. 267–297, 2007.

[98] A. V. Kabashin, S. Patskovsky, and A. N. Grigorenko, "Phase and amplitude sensitivities in surface plasmon resonance bio and chemical sensing," *Opt. Express*, vol. 17, pp. 21191–21204, 2009.

[99] K. Lodewijks, W. Van Roy, G. Borghs, L. Lagae, and P. Van Dorpe, "Boosting the Figure-Of-Merit of LSPR-Based Refractive Index Sensing by Phase-Sensitive Measurements," *Nano Letters*, vol. 12, no. 3, pp. 1655–1659, 2012.

[100] M. Svedendahl, S. Chen, A. Dmitriev, and M. Käll, "Refractometric sensing using propagating versus localized surface plasmons: A direct comparison," *Nano Letters*, vol. 9, no. 12, pp. 4428–4433, 2009.

[101] W. Zhou and T. W. Odom, "Tunable subradiant lattice plasmons by out-of-plane dipolar interactions," *Nat Nano*, vol. 6, no. 7, pp. 423–427, 2011.

[102] B. Auguié, B. M., W. L. Barnes, and F. J. García de Abajo, "Diffractive arrays of gold nanoparticles near an interface: Critical role of the substrate," *Physical Review B*, vol. 82, no. 15, p. 155447, 2010.

[103] C. Yizhuo, S. Ethan, Y. Tian, and B. C. Kenneth, "Experimental observation of narrow surface plasmon resonances in gold nanoparticle arrays," *Applied Physics Letters*, vol. 93, no. 18, p. 181108, 2008.

[104] A. G. Nikitin, T. Nguyen, and H. Dallaporta, "Narrow plasmon resonances in diffractive arrays of gold nanoparticles in asymmetric environment: Experimental studies," *Applied Physics Letters*, vol. 102, no. 22, p. 221116, 2013.

[105] J. Becker, A. Trügler, A. Jakab, U. Hohenester, and C. Sönnichsen, "The optimal aspect ratio of gold nanorods for plasmonic bio-sensing," *Plasmonics*, vol. 5, no. 2, pp. 161–167, 2010.

[106] V. G. Kravets, G. Zoriniants, C. P. Burrows, F. Schedin, A. K. Geim, W. L. Barnes, and A. N. Grigorenko, "Composite Au Nanostructures for Fluorescence Studies in Visible Light," *Nano Letters*, vol. 10, pp. 874–879, 2010.

[107] V. G. Kravets, G. Zoriniants, C. P. Burrows, F. Schedin, C. Casiraghi, P. Klar, A. K. Geim, W. L. Barnes, and A. N. Grigorenko, "Cascaded Optical Field Enhancement in Composite Plasmonic Nanostructures," *Physical Review Letters*, vol. 105, p. 246806, 2010.

[108] P. Offermans, M. C. Schaafsma, S. R. K. Rodriguez, Y. Zhang, M. Crego-Calama, S. H. Brongersma, and J. Gómez Rivas, "Universal scaling of the figure of merit of plasmonic sensors," *ACS Nano*, vol. 5, no. 6, pp. 5151–5157, 2011.

[109] J. Ye and P. Van Dorpe, "Improvement of figure of merit for gold nanobar array plasmonic sensors," *Plasmonics*, vol. 6, no. 4, pp. 665–671, 2011.

[110] S.-Q. Li, W. Zhou, D. Bruce Buchholz, J. B. Ketterson, L. E. Ocola, K. Sakoda, and R. P. H. Chang, "Ultra-sharp plasmonic resonances from monopole optical nanoantenna phased arrays," *Applied Physics Letters*, vol. 104, no. 23, 231101, 2014.

[111] J. Chen, M. Badioli, P. Alonso-Gonzalez, S. Thongrattanasiri, F. Huth, J. Osmond, M. Spasenovic, A. Centeno, A. Pesquera, P. Godignon, A. Zurutuza Elorza, N. Camara, F. J. G. de Abajo, R. Hillenbrand, and F. H. L. Koppens, "Optical nano-imaging of gate-tunable graphene plasmons," *Nature*, vol. 487, no. 77, pp. 77–81, 2012.

[112] G. Xu, J. Liu, Q. Wang, R. Hui, Z. Chen, V. A. Maroni, and J. Wu, "Plasmonic graphene transparent conductors," *Advanced Materials*, vol. 24, no. 10, pp. 71–76, 2012.

[113] R. R. Nair, P. Blake, J. R. Blake, R. Zan, S. Anissimova, U. Bangert, A. P. Golovanov, S. V. Morozov, A. K. Geim, K. S. Novoselov, and T. Latychevskaia, "Graphene as a transparent conductive support for studying biological molecules by transmission electron microscopy," *Applied Physics Letters*, vol. 97, no. 15, p. 153102, 2010.

[114] V. G. Kravets, A. N. Grigorenko, R. R. Nair, P. Blake, S. Anissimova, K. S. Novoselov, and A. K. Geim, "Spectroscopic ellipsometry of graphene and an exciton-shifted van Hove peak in absorption," *Phys. Rev. B*, vol. 81, no. 15, p. 155413, 2010.

[115] A. B. Kuzmenko, E. van Heumen, F. Carbone, and D. van der Marel, "Universal optical conductance of graphite," *Physical Review Letters*, vol. 100, no. 11, p. 117401, 2008.

[116] E. J. Nicol and J. P. Carbotte, "Optical conductivity of bilayer graphene with and without an asymmetry gap," *Physical Review B*, vol. 77, no. 15, p. 155409, 2008.

[117] Kuiru L., M.I. Stockman and D.J. Bergman, "Self-Similar Chain of Metal Nanospheres as an Efficient Nanolens," *Physical Review Letters*, vol. 91, p. 227402, 2003.

[118] S. Bidault, F. J. García de Abajo, and A. Polman, "Plasmon-based nanolenses assembled on a well-defined DNA template," *Journal of the American Chemical Society*, vol. 130, no. 9, pp. 2750–2751, 2008.

[119] S. Toroghi and P. G. Kik, "Cascaded field enhancement in plasmon resonant dimer nanoantennas compatible with two-dimensional nanofabrication methods," *Applied Physics Letters*, vol. 101, 013116, no. 1, 2012.

[120] B. Ding, Z. Deng, H. Yan, S. Cabrini, R. N. Zuckermann, and J. Bokor, "Gold nanoparticle self-similar chain structure organized by DNA origami," *J. Am. Chem. Soc.*, vol. 132, no. 10, pp. 3248–3249, 2010.

[121] C. Höppener, Z. J. Lapin, P. Bharadwaj, and L. Novotny, "Self-similar gold-nanoparticle antennas for a cascaded enhancement of the optical field," *Phys. Rev. Lett.*, vol. 109, no. 1, p. 017402, 2012.

[122] J. D. Caldwell, O. Glembocki, F. J. Bezares, N. D. Bassim, R. W. Rendell, M. Feygelson, M. Ukaegbu, R. Kasica, L. Shirey, and C. Hosten, "Plasmonic nanopillar arrays for large-area, high-enhancement surface-enhanced Raman scattering sensors," *ACS Nano*, vol. 5, no. 5, pp. 4046–4055, 2011.

Appendix A

Additional super-narrow resonances

The samples with 300 μm x 100 μm stripe arrays that were fabricated in chapter 3 to create ultra-narrow diffraction coupled resonances that could be excited at grazing incidence (figures 3.1 and 3.2) were the second step of optimisation of resonances measured on samples that were fabricated with a much wider range of periodicities and stripe widths. Here, results from these initial samples are presented, demonstrating the effectiveness of this sample configuration for producing narrow resonances with a wide range of stripe widths and periodicities.

Presented is ellipsometry measured at angles 45, 55, 65 and 74° (the steepest angle measurable with focussing optics in the standard configuration) on samples with periods 700, 1000, 1500 and 2000 nm. Each 200 μm x 200 μm sample of each periodicity was split into four 100 μm x 100 μm nanostripe arrays, designed to have nanostripe widths of 1/5, 2/5, 3/5 and 4/5 the sample periodicity (figure A.1). However, the nanostripe widths came out larger than intended, as our dose calibrations were for electron beam lithography on a plain glass/ chromium substrate. Lithography on a gold surface will back-scatter more electrons and thus create a higher electron dose in the resist. The actual values of the stripe widths, as measured in SEM, are labelled on the graphs. Nanostripes were 70 nm tall, on a 65 nm gold sublayer. The samples were measured every 2.5° between 45 and 74°, increasing to every 0.5° around the resonance minima (to ensure the minimum was precisely identified). Only data measured every ~10° is presented here to demonstrate the overall trend and avoid overcomplicating the plots.

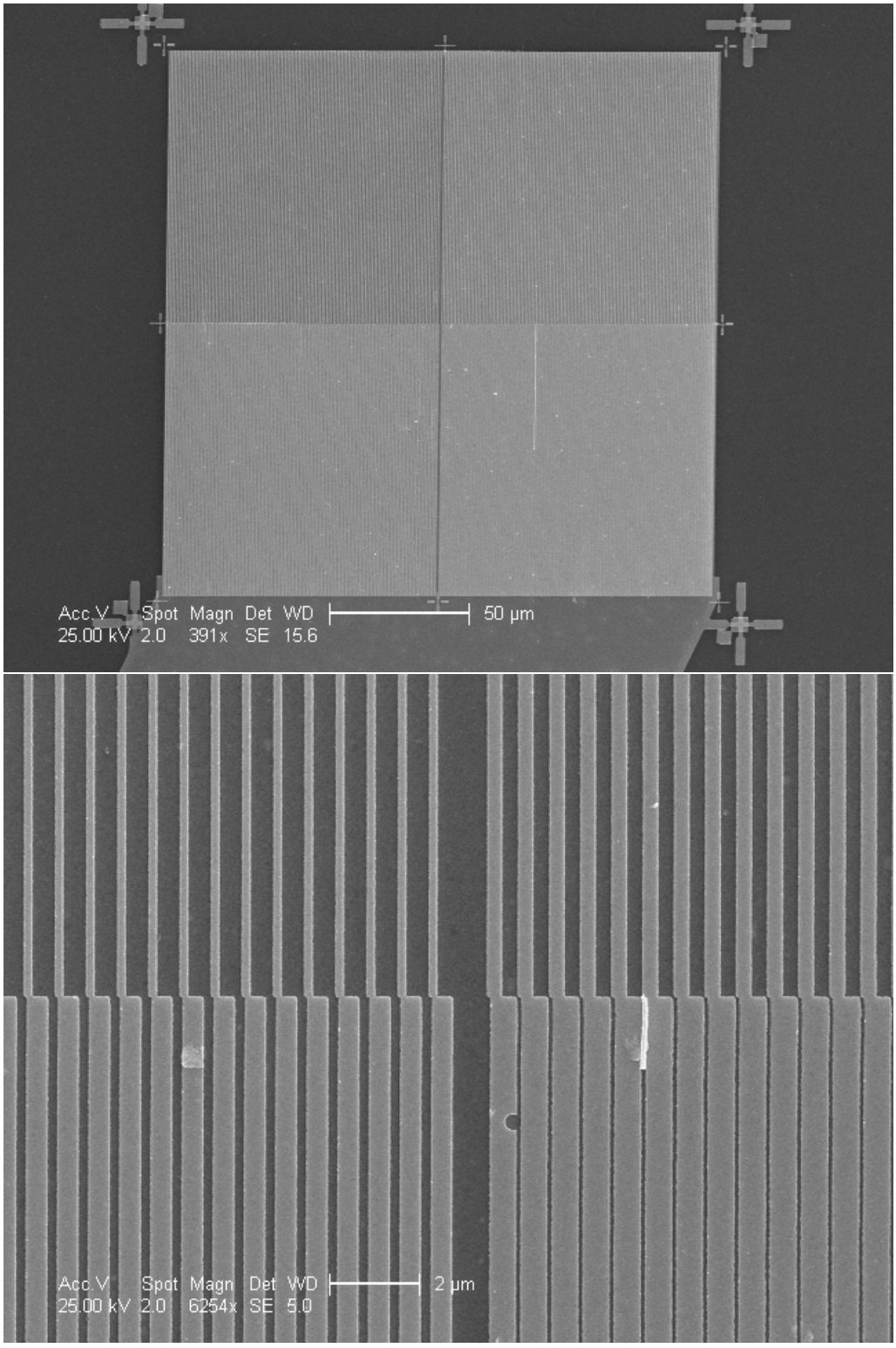

Figure A.1 – SEM images of the samples with period a = 700 nm. Top is an overview of the entire 200 µm x 200 µm array of four 100 µm x 100 µm nanostripe arrays, and bottom is a close up of the central region, showing nanostripes of all four thicknesses.

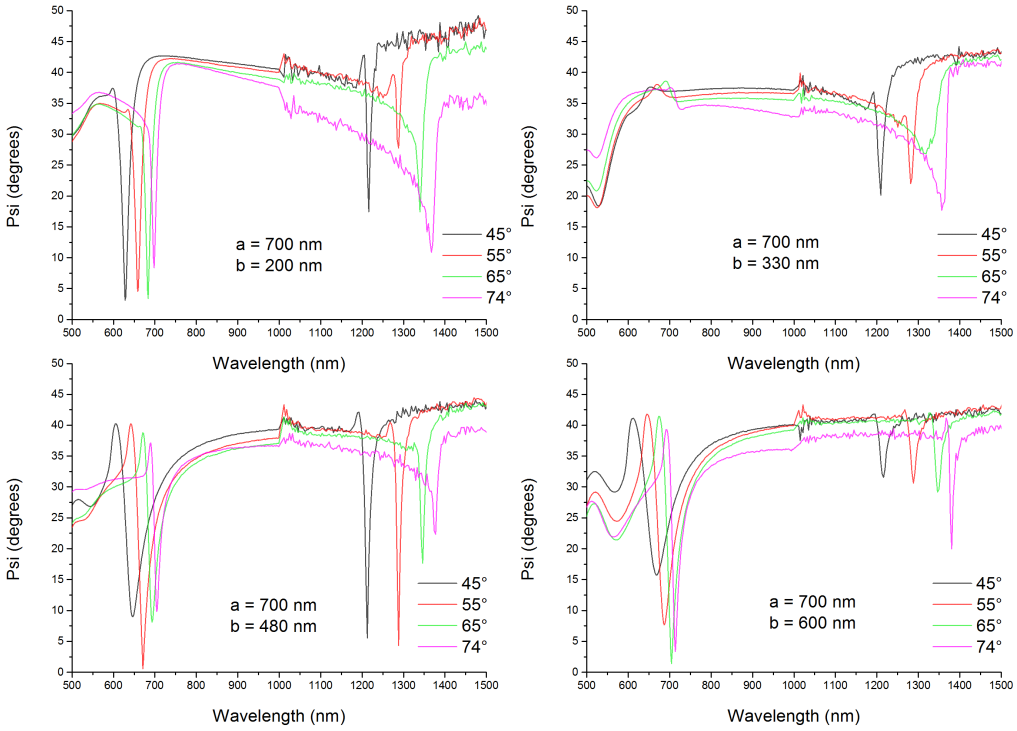

Figure A.2 – Resonances from arrays with period $a = 700$ nm and various stripe widths b (labelled on graphs)

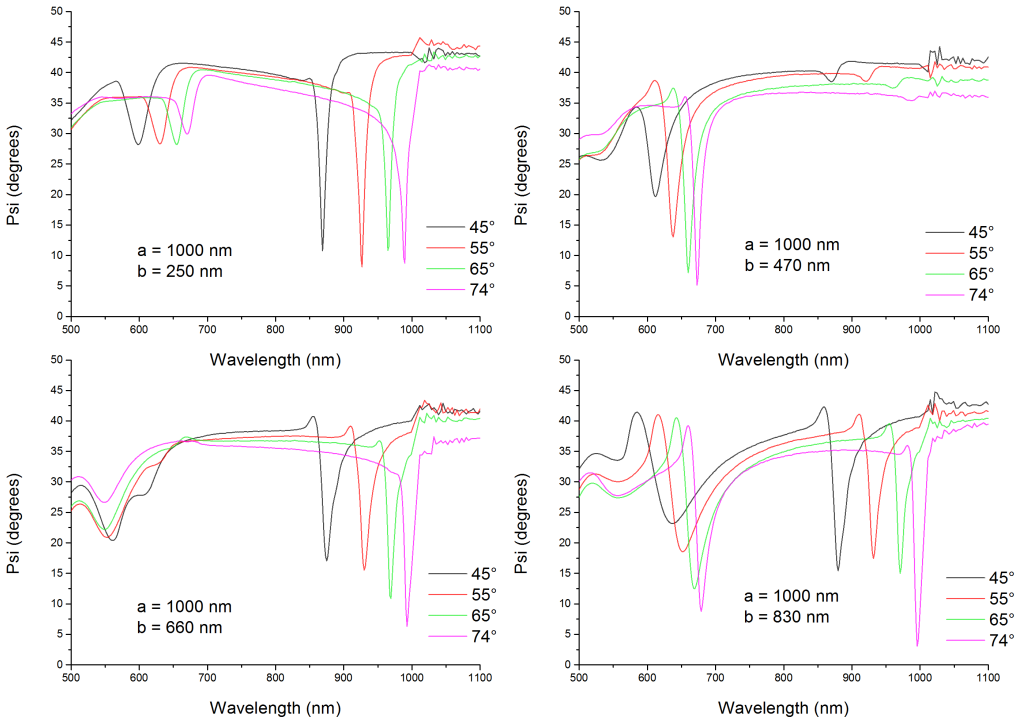

Figure A.3 – Resonances from arrays with period $a = 1000$ nm and various stripe widths b (labelled on graphs)

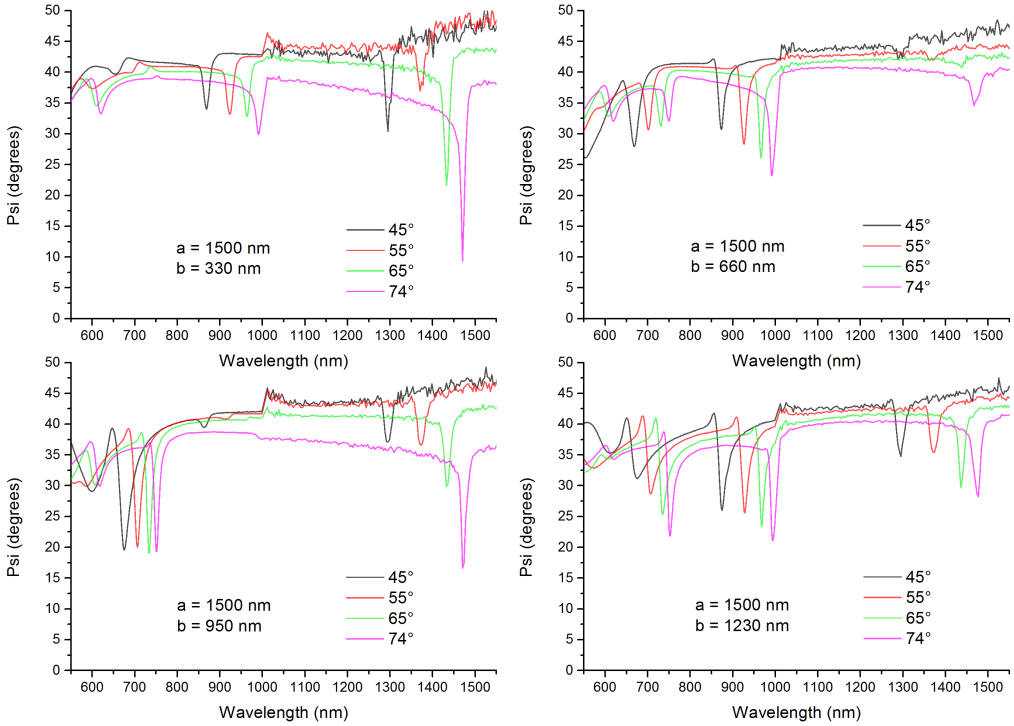

Figure A.4 – Resonances from arrays with period a = 1500 nm and various stripe widths b (labelled on graphs)

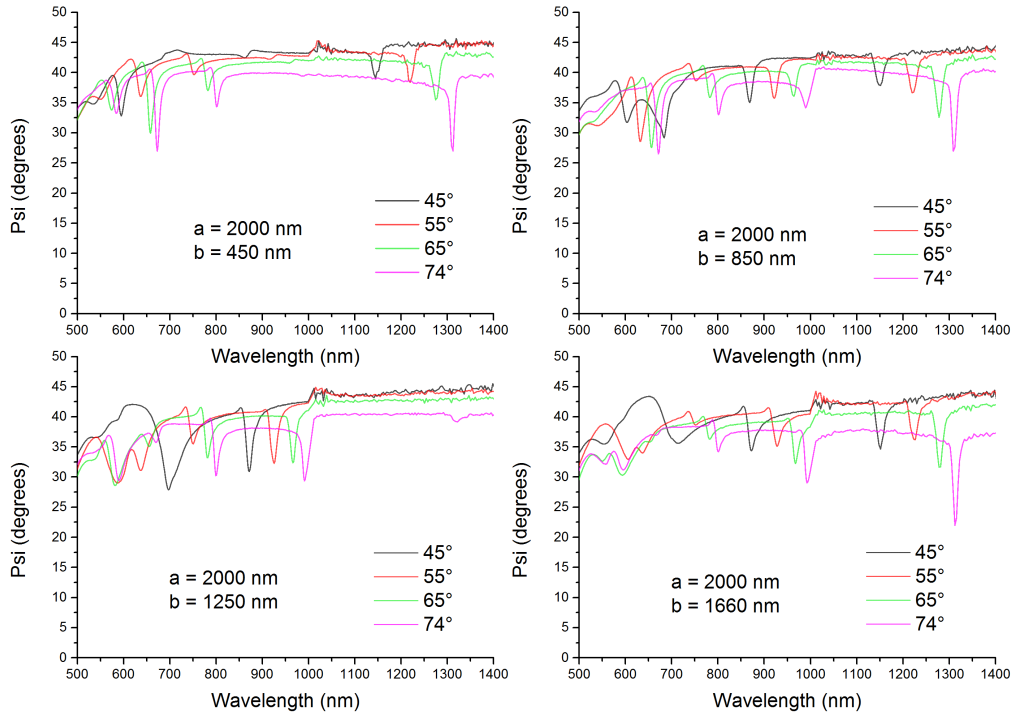

Figure A.5 – Resonances from arrays with period a = 2000 nm and various stripe widths b (labelled on graphs)